Vol. 40 (2009) *ACTA PHYSICA POLONICA B* No 8

UNDERSTANDING THE STRUCTURE OF THE PROTON: FROM HERA AND TEVATRON TO LHC

M. Boonekamp, F. Chevallier, C. Royon, L. Schoeffel

CEA Saclay/IRFU-SPP, 91191 Gif-sur-Yvette, France

(Received February 11, 2009; revised version received June 5, 2009)

In this review, we first discuss the perspectives concerning a better determination of the proton structure in terms of quarks and gluons at LHC after describing the results coming from HERA and Tevatron. In a second part of the review, we describe the diffractive phenomena at HERA and Tevatron and the consequences for LHC.

PACS numbers: 12.38.–t

Understanding the fundamental structure of matter requires an understanding of how quarks and gluons are assembled to form hadrons and of the structure of the protons which are the colliding particles at LHC. The arrangement of quarks and gluons inside nucleons can be probed by accelerating electrons, hadrons or nuclei to precisely controlled energies, smashing them into a target nucleus and examining in detail the final products.

In this review, we first discuss the structure of the proton in terms of quarks and gluons. We first present briefly the results from HERA and the Tevatron and then discuss two aspects at LHC: how we can improve our knowledge on parton distribution functions (PDFs) of the proton, and if it is possible to find some observables less sensitive to PDF uncertainties to probe new physics beyond the standard model. In a second part of the review, we will discuss diffraction at HERA, Tevatron and the prospects for LHC.

1. The parton distribution functions at the LHC

1.1. The challenges of LHC physics

The LHC physics program is rich and has been widely described [1–3]. It encompasses the searches for new particles up to masses of several TeV, including the elucidation of electroweak symmetry breaking and the possible observation of new symmetries at higher scales, and precision measurements of fundamental parameters in the electroweak and strong gauge sectors.

A common requirement for this program to succeed is a good control of the proton parton densities. To be more specific, the discovery of the Higgs boson, and subsequent measurements of its couplings relies on precise predictions of the gluon density in the range $x \sim 10^{-2}$–10^{-1}, and at corresponding scales $Q^2 = m_H^2 \sim 10^4$–$10^6\,\mathrm{GeV}^2$. The high-x, high-Q^2 gluon density also determines the production rate of high-E_T jets, and affects *e.g.* the measurement of the running of α_S and the search for extra dimensions through this final state.

The LHC also allows to reach very low values of x as it is indicated in Fig. 1. Dedicated processes at LHC will allow to study the low x region in detail as we will see in the following, for instance using Mueller–Navelet jets. In addition, the saturation region where the gluon density is large and gluons overlap in the proton might be accessible at LHC as we will discuss it further.

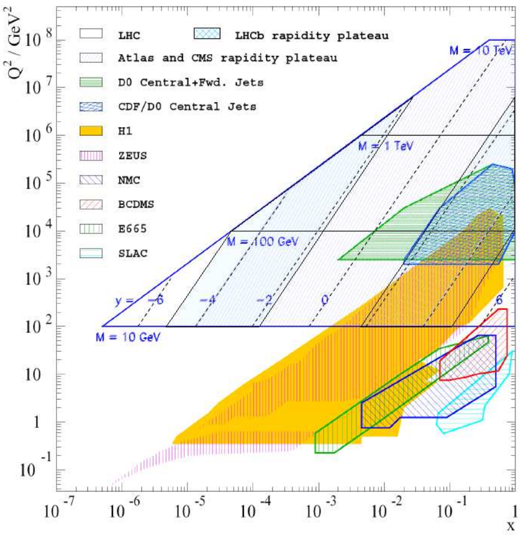

Fig. 1. (x, Q^2) domain probed by the fixed target, HERA, Tevatron and LHC experiments.

The on-shell production of electroweak gauge bosons is mainly controlled by the sea quarks. In this case Q^2 is essentially fixed, but the vector boson rapidity distribution probes the range $x \sim 10^{-5}$–10^{-1}. Precise measurements of the electroweak parameters, notably the W boson mass m_W and the weak mixing angle, $\sin^2\theta_W$, require tightly constrained parton densities in this range. The interpretation of high-mass Drell–Yan events or gauge boson pairs in terms of electroweak interactions again requires a good control of these densities at scales up to $10^6\,\mathrm{GeV}^2$.

In the process of quantifying the PDF-induced uncertainties on the above observables, and improving them where needed, one has to remember the hypotheses under which the PDFs have been determined in the first place. In particular, the dependence of the results on the choice of functional form of the parton densities at $Q_0 \sim m_p$ often cannot be ignored. However, in the neural network PDF approach, such source of uncertainty is perfectly taken into account since input PDFs are parametrised with neural networks which are flexible functional forms [9]. Hypotheses concerning the initial flavor composition (u, d, s and possibly c quarks) need to be accounted for, as well. In addition, the QCD evolution of these densities is performed assuming different schemes (Dokshitzer–Gribov–Lipatov–Altarelli–Parisi, DGLAP [4], Balitski–Fadin–Kuraev–Lipatov, BFKL [5]), perturbative orders (leading order (LO), next-to-leading order (NLO), next-to-next-to-leading order (NNLO)), including saturation effects or not. When quoting a PDF-induced uncertainty, one needs to ascertain whether these underlying hypotheses affect the result or can be ignored.

In the following, we review the most prominent examples of the influence of parton densities on the LHC physics program. After an introduction about the status of PDF determination and their uncertainties, coming mainly from fixed target experiments and from HERA, we discuss briefly the input from the Tevatron. The third section describes how LHC measurements are sensitive to gluon PDF and how to reduce its uncertainty. The fourth section is devoted to quark PDF. The last section deals with observables less sensitive to PDF uncertainties to look for beyond standard model effects; we can quote for instance ratios of cross-sections with the goal to measure separately a subset of parton densities or to reduce the impact of the PDF uncertainties.

1.2. Status of PDF uncertainties

The understanding of the proton structure has made great progress since the observation of the broken scale invariance in the early 70's. The measurement of the proton structure function at HERA in the H1 and ZEUS experiment allowed to make considerable progress on the knowledge of the proton structure [6]. The HERA data allowed to constrain strongly the PDF uncertainties at medium $x \sim 10^{-2}$, and to access a completely new kinematical region in x down to 10^{-5}. These data are fundamental to get precise cross-sections at LHC for beyond standard model effects and the background. In this section, we will only summarize the status on the PDF uncertainties since many reviews described already the impact of HERA on PDF determination [6].

According to the last version of global QCD fits, the uncertainties on the quark and gluon densities in the proton reach few per-cent in most of the kinematic plane in $(x,\, Q^2)$ [7, 8]. However, at LHC, the uncertainty on parton distributions leads to one of the most important uncertainties for many measurements, greater than the expected statistical errors, and thus reduce the sensitivity of these measurements to new physics effects. Several reasons explain why PDF-induced uncertainties on observables can be so large and why they must be quoted with critical thinking.

First, the uncertainties on PDFs come from the uncertainties on parameters of the functional form at $Q_0^2 \sim m_p^2$. These parameters are the output of global QCD fits on data (fixed-target, HERA, and Tevatron experiments). Valence quark PDFs can be essentially measured in the high-x region, so the largest uncertainties ($> 20\%$) on valence quark distributions are found at low x ($x < 10^{-3}$) and very high x ($x > 0.8$). On the contrary, the uncertainty on sea quark and gluon distributions reaches 20% at high x ($x > 0.2$). This is due to the lack of data on processes using sea quarks and gluon in this region and to the rapid fall off of the parton distributions at high x. At hadron colliders, many measurements are sensitive to a large x or Q^2 range, and not only to the intermediate region $10^{-3} < x < 10^{-1}$ in which PDFs are best known. Large uncertainties on PDFs are found at high x ($x > 0.2$) or low-x ($x < 10^{-4}$), and the error can be greater than 20%. Thus, precise measurements at LHC could help to reduce the errors on PDF and improve our knowledge of the proton substructure.

Second, one has to remember the hypotheses under which the PDFs have been determined in the first place. In particular, the dependence of the results on the choice of the functional form of the parton densities at $Q_0^2 \sim m_p^2$ often cannot be ignored. These hypotheses are needed to decrease the numbers of degrees of freedom in QCD fits, but the systematic uncertainty induced by such approximations cannot be evaluated any longer with one single PDF set. Among these assumptions, the ratio of the $\bar{d}, \bar{u}$ sea quark PDFs in the asymptotic low x region are often set to one, the sea quark and antiquark densities at Q_0^2 often have the same parametrisation, *etc.* Hypotheses concerning the initial flavor composition need to be accounted for, as well. The description of the strange quark and antiquark distributions at Q_0^2 may require additional degrees of freedom [7]. The proton could have an intrinsic charm quark component at $Q_0^2 \sim m_p^2$, thus enhancing the rate of charm quark-induced processes [47]. More generally, the extraction of heavy flavour PDFs and the comparison to data is still difficult and suffers from large statistical and systematic uncertainties.

The impact at higher scale of some approximations can be tested using different sets of PDFs, because the underlying hypotheses on the functional form are different. As an example, the effects of the underlying hypotheses can be seen in Fig. 2, where some differences are visible at $x \approx 10^{-2}$ for valence quark distributions. The hypotheses on the shape of PDF at Q_0^2 have to be tested when measurements become more and more precise. The LHC will play a major role in testing the PDF functional form.

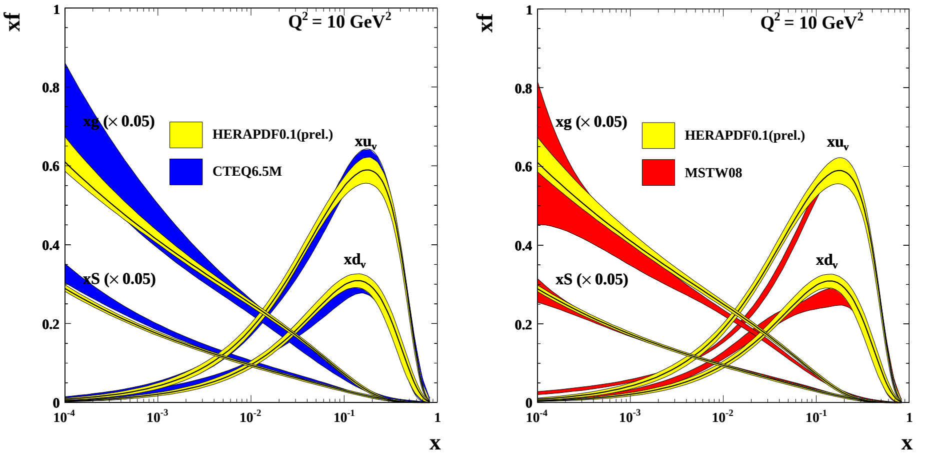

Fig. 2. $(x,\, Q^2)$ PDFs at $Q^2 = 10\,\mathrm{GeV}^2$ obtained from CTEQ6.5, MSTW08 and HERAPDF01(prel.) [10].

Third, the QCD evolution of these densities is performed using different evolution equations: DGLAP for Q^2 evolution, BFKL for $\ln 1/x$ evolution. The evolution equation can also be computed at different perturbative orders (LO, NLO, NNLO in α_{S} for DGLAP and leading log (LL), next-to-leading log (NLL) in $\log 1/x$ for BFKL), including the appropriate treatment of the mass of heavy quarks and the evolution of the strong coupling constant at low $Q^2 \approx m_q^2$. In addition, saturation effects could be strong at low Q^2 and very low x. Due to the large $(x,\, Q^2)$ domain accessible at LHC, many measurements are sensitive to these effects, and thus can bring constraints on evolution equations.

In the following, we describe which measurements at LHC can bring information on the proton structure, and thus help not only to reduce the PDF uncertainties, but also to test the hypotheses on the initial shape of PDFs at Q_0^2 and to test the evolution equations. Prospects for improvements and their difficulties will be presented in this context.

Before describing the expected results from LHC, we will give the QCD results obtained at Tevatron. The HERA results are described in detail in Ref. [6]. It is worth noticing that the results on PDFs coming from HERA are presently being improved by reducing the systematics on the different structure function measurements and combining the H1 and ZEUS data.

2. State of the art at the Tevatron

2.1. Inclusive jet cross-section measurements at the Tevatron

The first measurement sensitive to PDFs which can be performed at Tevatron is the inclusive jet cross-section which relies on the precise determination of the jet energy calibration. We will describe briefly how the jet energy is obtained at Tevatron since similar methods can be used at LHC. The jet energy scale is determined mainly using γ+jet events. In the DØ Collaboration as an example, the corrected jet energy is obtained using the following method

$$E_{\rm jet}^{\rm corr} = \frac{E_{\rm jet}^{\rm juncorr} - {\rm Off}}{{\rm Show} \times {\rm Resp}}\,, \qquad (1)$$

where $E_{\rm jet}^{\rm corr}$ and $E_{\rm jet}^{\rm uncorr}$ are respectively the corrected and uncorrected jet energies. The offset corrections (Off) are related to uranium noise and pile-up and are determined using minimum-bias and zero-bias data. The showering corrections (Show) take into account the energy emitted outside the jet cone because of the detector and dead material and, of course, not the physics showering outside the jet cone which corresponds to QCD radiation outside the cone. The jet response (Resp) is the largest correction, and can be subdivided in few corrections. The first step is to equalize the calorimeter response as a function of rapidity, and the jet response is then measured for the central part of the calorimeter using only the $p_{\rm T}$ balance in γ+jet events. Some additional small corrections related to the method biases are introduced. One important additional correction deals with the difference in response between quark and gluon jets. The difference was studied both in data and in Monte Carlo (using for instance the γ+jet and the dijet samples which are, respectively, quark and gluon dominated) and leads to a difference of 4 to 6% as a function of jet $p_{\rm T}$, which is not negligible if one wants a precision on jet energy scale of the order of 1%. This has an important consequence. The jet energy scale is not universal but sample dependent. QCD jets (gluon dominated) will have a different correction with respect to the $t\bar{t}$ events for instance which are quark dominated. The CDF Collaboration follows a method which is more Monte Carlo oriented using beam tests and single pion response to tune their Monte Carlo. At LHC, it will be possible to use Z+jets which do not suffer from the ambiguity of photon identification in the detector.

The uncertainties reached by the DØ Collaboration concerning the determination of jet energy scale are of the order of 1.2% for jet $p_{\rm T}$ between 70–400 GeV in a wide range of rapidity around zero (the uncertainty is of the order of 2% for a rapidity of 2.5). This allows to make a very precise measurement of the jet inclusive cross-section as a function of their transverse momentum.

The measurement of the inclusive jet cross-section [11] was performed by the DØ and CDF collaborations at Tevatron using a jet cone algorithm with a cone size of 0.7 (DØ and CDF) and the $k_{\rm T}$ algorithm (CDF). Data are corrected to hadron level (DØ) or parton level (CDF). The motivation of this measurement is double: it is sensitive to beyond standard model effects such as quark substructure and to PDFs, especially the gluon density at high x. Historically, the excess observed by the CDF Collaboration in 1995 concerning the inclusive jet $p_{\rm T}$ spectrum compared to the parametrisations was suspected to be a signal of quark substructure but it was found that increasing the gluon density at high x could accommodate these data. This raises the question of PDFs *versus* beyond standard model effects, and the interpretation of data in general. Data are compared with NLO QCD calculations using either CTEQ6.5M [12] for DØ or CTEQ6.1 for CDF (the uncertainties of the CTEQ6.5M parametrisation are two times smaller). A good agreement is found over six orders of magnitude. The ratio data over theory for the DØ and CDF measurements are given in Figs 3 and 4. A good agreement is found between NLO QCD and the DØ or CDF measurements with a tendency of the CTEQ parametrisation to be slightly lower than the data at high jet $p_{\rm T}$. The MRST2004 [12] parametrisation follows the shape of the measurements. Given the precision obtained on jet energy scale, the uncertainties obtained by the DØ Collaboration are lower than the PDF ones and will allow to constrain further the PDFs and specially the gluon density at high x (the uncertainties of the measurement performed by the CDF Collaboration are about two times larger). An update of the CTEQ and MRST PDFs using these latest data are expected soon. The DØ Collaboration took also special care of the uncertainty correlation studies, by giving the effects of the 24 sources of systematics in data.

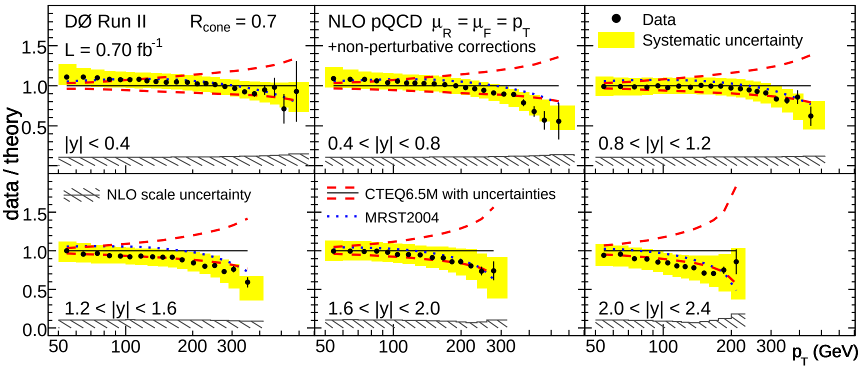

Fig. 3. Data over theory for the inclusive $p_{\rm T}$ cross-section measurement from the DØ Collaboration using the 0.7 jet cone. Data are compared to NLO QCD calculations using the CTEQ6.5M parametrisation.

In addition, the CDF Collaboration measured the dijet mass cross-section [13] above 180 GeV, and up to 1.2 TeV. No excess was found with respect to NLO QCD calculations and this measurement allows to exclude excited quarks below 870 GeV, Z' (resp. W') below 740 (resp. 840) GeV[1], and technirho below 1.1 TeV.

The question rises if PDFs can be further constrained at LHC using inclusive measurements. The PDF uncertainties are typically of the order of 15% for a jet $p_{\rm T}$ of 1 TeV, and 25% of 2 TeV for $1 < |\eta_{\rm jet}| < 2$ (without taking into account the new Tevatron measurements which we just discussed). A typical uncertainty of 5% (resp. 1%) on jet energy scale leads to a systematic uncertainty on 30 to 50% (resp. 6 to 10%) on the jet cross-section. A precise determination of the jet energy scale at LHC will thus be needed to get competitive measurements at LHC. In the following, we will discuss more clever ways to find observables less sensitive to PDF uncertainties but still sensitive to beyond standard model effects.

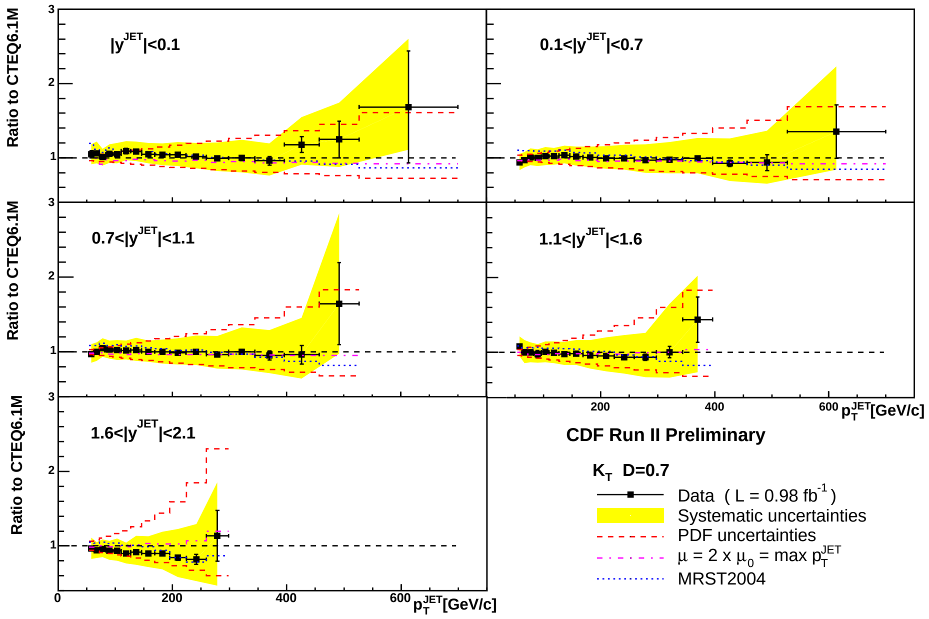

Fig. 4. Data over theory for the inclusive $p_{\rm T}$ cross-section measurement from the CDF Collaboration using the $k_{\rm T}$ algorithm. Data are compared to NLO QCD calculations using the CTEQ6.1 parametrisation.

---

[1] Stronger limits on W' and Z' mass limits come from lepton based searches.

2.2. Multijet cross-section measurements at the Tevatron and at HERA

The measurement of multijet cross-sections at the Tevatron and at HERA (and later on at LHC) is fundamental to constrain the PDFs and to tune the Monte Carlo, since it is a direct background entering in many searches for Higgs bosons or new particles at the LHC. We can quote for instance the search for Higgs bosons in association with $t\bar{t}$, the measurement of the $t\bar{t}$ production cross-section, the search for R-parity violated SUSY (which can lead up to 8–10 jets per event ...).

2.2.1. Measurement of $\Delta\Phi$ between jets in DØ

The advantage of the measurement of the difference in azimuthal angle between two leading jets in an inclusive QCD sample as was performed by the DØ Collaboration is that there is no need of precise knowledge of jet energy scale (the measurement is dominated by the knowledge of jet angles) and this can be performed at the beginning of data taking at the LHC for instance when the detectors are not yet fully calibrated. The $\Delta\Phi$ spectrum was measured in four different regions in maximum jet transverse momentum, and a good agreement was found with NLO calculations using either the CTEQ and MRST parametrisations except at very high $\Delta\Phi$ where soft radiation is missing [14]. PYTHIA [15] shows a disagreement at small $\Delta\Phi$, showing a lack of initial state gluon radiation, while HERWIG [16] shows a good agreement with data. It will be important to redo this kind of measurements at the beginning of LHC.

2.2.2. Measurement of γ+jet cross-sections

The DØ Collaboration measured the inclusive production of isolated $\gamma+$ jets in different detector regions requiring a central photon and a central or a forward jet. It distinguished the cases when the photon and the jet are on the same or opposite side. The cross-section has been found in disagreement with NLO QCD expectations both in shape and normalisation and the reason is still unclear [17]. It is worth noticing that the transverse momentum of the photon is not very high for that measurement, and maybe the problem is related to the fact that it is not performed where perturbative QCD can be trusted. We will come back on that kind of measurement when we discuss the possibilities at LHC.

2.2.3. Jet shape measurements in CDF

The jet shape is dictated by multi-gluon emission from primary partons, and is sensitive to quark/gluon contents, PDFs and running α_{S}, as well as underlying events. We define Ψ which is sensitive to the way the energy is spread around the jet center

$$\Psi(r) = \frac{1}{N_{\mathrm{jets}}}\Sigma_{\mathrm{jets}}\frac{P_{\mathrm{T}}(0,r)}{P_{\mathrm{T}}^{\mathrm{jet}}(0,R)}\,, \tag{2}$$

where R is the jet size. The energy is more concentrated towards the jet center for quark than for gluon jets since there is more QCD radiation for gluon jets (which means that Ψ is closer to one for quark jets when $r \sim 0.3R$ for instance). The CDF Collaboration measured $\Psi(0.3/R)$ for jets with $0.1 < |y| < 0.7$ as a function of jet p_{T} and found higher values of Ψ at high p_{T} as expected since jets are more quark like [18] and this is well described by QCD expectations. This measurement also helps tuning the PYTHIA and HERWIG generators since it is sensitive to underlying events in particular.

The CDF Collaboration studied also the jet shapes for b-jets in four different p_{T} bins [19] since it is sensitive to the b-quark content of the proton, and the result is given in Fig. 5. The default PYTHIA and HERWIG Monte Carlo in black full and dashed lines respectively are unable to describe the measurement. Compared to the inclusive jet shape depicted in Fig. 5 upper solid line (red) for PYTHIA, the tendency of the b-jet shape is definitely the right one, leading to smaller values of Ψ as expected, but the measurement leads to a larger difference. The effect of reducing the single b-quark fraction by 20% leads to a better description of data as it is shown in Fig. 5, lower

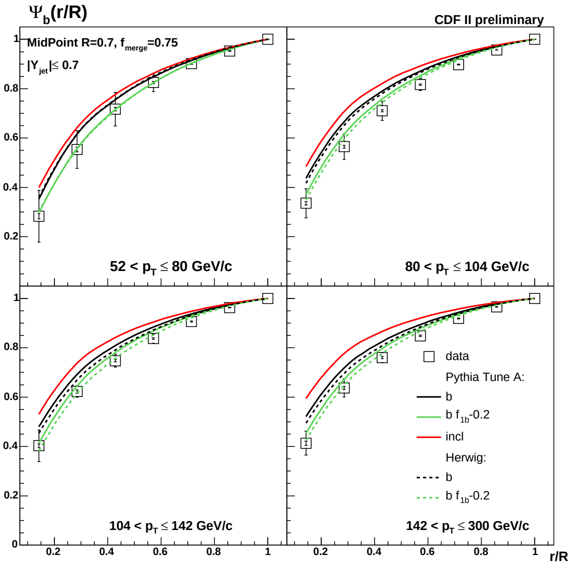

Fig. 5. Measurement of the b-jet shapes and comparison with the predictions of the PYTHIA and HERWIG Monte Carlo (see text).

solid and dashed lines (green). The fraction of b-jets that originate from flavour creation (where a single b-quark is expected in the same jet cone) over those that originate from gluon splitting (where two b-quarks are expected in the same jet cone) is different in Monte Carlo and data. This will be an important measurement to perform again at LHC since it is a direct background to searches for the Higgs boson and for new phenomena.

The CDF Collaboration also measured the $b\bar{b}$ dijet cross-section as a function of the leading jet p_{T} and the difference in azimuthal angle between the two jets and it leads to the same conclusion, namely that PYTHIA and HERWIG underestimates the gluon splitting mechanism [13].

2.3. A parenthesis: underlying events at Tevatron and LHC

This section is not directly related to the proton structure but understanding underlying events is a necessary step prior constraining further the proton structure. We will not mention further this aspect in the following but wanted to stress it while discussing the main results from Tevatron. The CDF Collaboration measured underlying events at Tevatron and used these measurements to tune in particular the PYTHIA generator. pp or $p\bar{p}$ interactions are namely not as simple as interactions in ep colliders. In addition to the hard scattering producing dijets, high p_{T} leptons ..., spectator partons produce additional soft interactions called underlying events. The main consequence is that it introduces additional energy in the detector not related to the main interaction which needs to be corrected.

To study this kind of events, the idea is quite simple. It is for instance possible to use dijet events and we can distinguish in azimuthal angle three different regions: the "toward" region around the leading jet direction defined by a cone of 60 degrees around the jet axis, the "away" region in the opposite direction to the jet, and the "transverse" region — the remaining regions far away from the jet and the "away" region, as shown in Fig. 6. In dijet events,

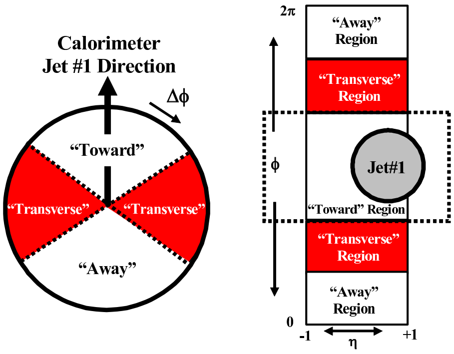

Fig. 6. Definition of the "toward", "away" and "transverse" regions in the case of dijet events as an example.

the "transverse" region will be dominated by underlying events. The CDF Collaboration measured the charged multiplicity and the charged transverse energy as a function of jet transverse energy and used these quantities to tune the PYTHIA Monte Carlo leading to the so called Tune A and Tune AW [13].

Clean Drell–Yan events can also be used to tune underlying events [13]. The lepton pair defines the "toward" region while the "away" and "transverse" regions are defined in the same way as for dijets. As an example, we give in Fig. 7 the charged particle density as a function of the transverse momentum of the lepton pair in the three regions compared with the Tune AW of PYTHIA.

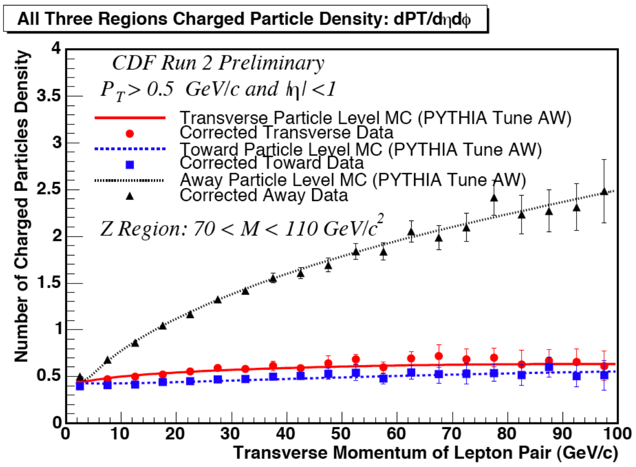

Fig. 7. Measurement of the charged particle density for Drell–Yan events in the "toward", "away" and "transverse" regions compared to PYTHIA Tune AW.

At LHC, one of the first measurements to be performed will be related to the tuning of underlying events in the generators. Present tunings between the different Monte Carlo (PYTHIA, PHOJET, HERWIG) show differences up to a factor six concerning the average multiplicity of charged particles as a function of the p_{T} of the leading jet as an example, and it is crucial to tune the Monte Carlo to accomplish fully the LHC program.

2.4. Measurements of the W+jet and Z+jet cross-sections at the Tevatron

The measurements of the W+jet and Z+jet cross-sections are specially important since they are a background for many searches and especially the search for the Higgs boson. We will also study further the W and Z production cross-sections to show their sensitivities on PDFs and as a method to constrain them further in the following.

2.4.1. Measurements of the $W + X$ cross-sections

The DØ Collaboration measured the ratio of the $W + c$ to the inclusive cross-section 0.074 ± 0.019 (stat.) $\pm^{0.012}_{0.014}$ (syst.) in agreement with NLO calculation [20]. It will be important to redo this measurement with higher statistics since it is directly sensitive to the s-quark PDF.

2.4.2. Measurement of the $Z + b$ and $W + b$ cross-sections

The motivation to measure the $Z + b$-jet cross-section is quite clear: this is a direct background for Higgs boson searches and it is also sensitive to the b quark content of the proton. The measurements of the $Z + b$-jet and $W + b$-jet cross-sections were performed by the CDF Collaboration at the Tevatron $\sigma(Z + b\,\mathrm{jets}) = 0.86 \pm 0.14 \pm 0.12\,\mathrm{pb}$ and $\sigma(W + b - \mathrm{jets}) \times \mathrm{BR}(W \to l\nu) = 2.74 \pm 0.27(\mathrm{stat.}) \pm 0.42(\mathrm{sys.})$ pb in agreement with NLO calculations and PYTHIA predictions [21]. The CDF Collaboration also compared the differential distributions in jet p_{T} and rapidity as an example and the distributions are found in good agreement with PYTHIA.

After reviewing briefly the present status on the proton knowledge from HERA and Tevatron, we will now discuss what can be expected at LHC, concerning the gluon and quark densities in the proton.

3. The gluon density in the proton

We review below the main physics items relying on the gluon density by studying two aspects: how does the physics at LHC (mainly searches) depend on the gluon uncertainty and how can we constrain it further using LHC data?

3.1. Impact on searches for new physics

The discovery of the Higgs boson, main objective and motivation for the construction of the LHC, is dominantly produced *via* gluon fusion for the mass range $100\,\mathrm{eV} < m_H < 1\,\mathrm{TeV}$. The hard cross-section and the decay modes can be accurately computed; for example, the NNLO QCD computation of FEHIP [22] claims a residual uncertainty of 1% on the production cross-section, assuming standard model couplings. The decay modes as computed with HDECAY [23] carry an even smaller uncertainty.

The dominant residual uncertainty on σ_H at the LHC comes from the uncertainty on the gluon density, as illustrated in Fig. 8 [24]. Depending on the value of m_H, the uncertainty varies between 5% and 10%. It is worthwhile to note, as can be seen on the figure, that the different PDF sets used (MRST, CTEQ, Alekhin) are sometimes marginally compatible; this examplifies the need to consider, in addition to the fit uncertainty claimed by each set, the framework (theory, underlying hypotheses) in which each fit has been performed.

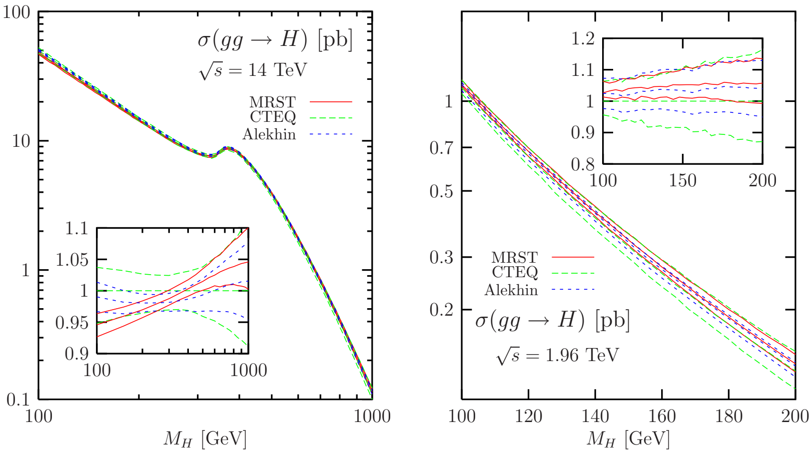

Fig. 8. Higgs boson production cross-section and its uncertainty, as a function of m_H.

This level of uncertainty does not affect the discovery potential (most often, signal and backgrounds are affected by the same uncertainty, which cancels in the ratio; besides, other systematic uncertainties dominate, depending on m_H and the final state considered). However, once the particle has been established and high statistics measurements of its couplings are underway, the gluon density will be the most significant source of theoretical uncertainty to the measurements.

High-E_{T} jets will be copiously produced at LHC: the expected cross-section for $E_{\mathrm{T}} > 1, \mathrm{TeV}$ is still about 20 pb. While this process has a high cross-section and is dominantly coupled to initial gluons, and as such is a natural probe of the proton PDFs, it is also sensitive to new particles. Scalar or vector s-channel resonances can appear in technicolor theories [25]; graviton production is another possibility [26]; as these processes display a peak in the invariant mass, these searches are relatively safe against PDF uncertainties.

On the other hand, certain theories with large compactification radius extra dimensions, or large number of extra dimensions, produce a continuum of Kaluza–Klein excitations, which appears as a modification of the slope of the differential cross-section, $d\sigma/dM$. Fig. 9 shows what can be expected in this case; it is easy to find unexcluded model parameters that predict deviations of 50% w.r.t. the standard model prediction, for $E_{\mathrm{T}} > 2$ TeV.

The uncertainty induced by the proton PDFs is displayed in Fig. 10. According to CTEQ6.1 (used in [27]), the cross-section uncertainty grows rapidly with m_{JJ}, being 30% at 2 TeV and up to factors of 10 at higher E_{T}. As we see, a good part of this process naïve sensitivity to new physics vanishes once PDF uncertainties are accounted for.

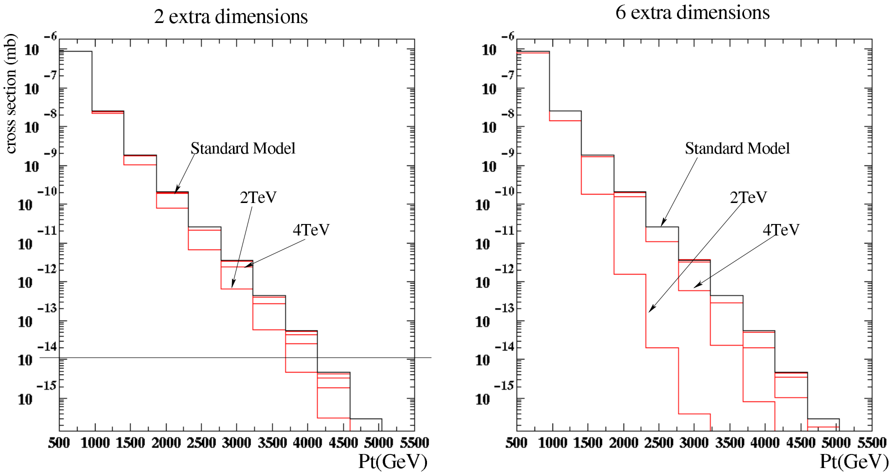

Fig. 9. Standard Model dijet cross-section as function of E_{T}, and expected modifications in the presence of extra dimensions. The successive curves represent, from top to bottom, the SM prediction and expected modifications of the spectrum in the presence of extra dimensions of size 8, 4 and 2 TeV.

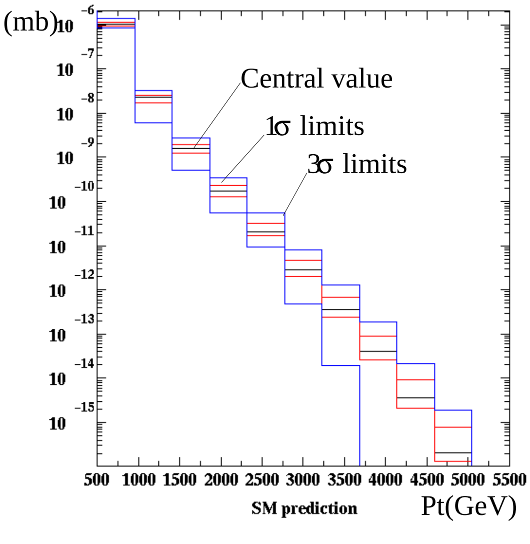

Fig. 10. Standard Model dijet cross-section and its uncertainty, as a function of m_{JJ} [27]. The central curve represents the SM prediction, and the envelopes represent the $1\,\sigma$ and $3\,\sigma$ confidence interval.

Another approach of the same problem was studied by ATLAS [28]. This note presented the LHC potential to measure the running of $\alpha_{\rm S}$ through an analysis of the dijet mass spectrum or jet $E_{\rm T}$ spectrum. The note concluded that although an absolute measurement of $\alpha_{\rm S}$ is out of reach, its running could be observed, and the standard evolution verified. At that time, PDF sets with uncertainties were not available and the related systematic uncertainties could not be studied; however, from the above discussion we can again anticipate that without significant improvements, PDF uncertainties compromise this prospect.

3.2. Discussion and expected improvements at the LHC

As we already mentioned, the above examples are direct results of the gluon density uncertainty. A convenient way to show this is displayed in Fig. 11. Writing

$$\sigma(M,y) = \int g(x,M) g(s/(Mx),M)\hat{\sigma}(M) \equiv \mathcal{L}(M,y)\hat{\sigma}(M)\,, \tag{3}$$

one can compute the "luminosity" $\mathcal{L}$ directly from the PDFs, and estimate the cross-section from the product of $\mathcal{L}$ with the hard process cross-section.

Fig. 11, left, shows the uncertainty on $\mathcal{L}$ as a function of M. The uncertainties quoted in the previous section are observed here, with $\delta\mathcal{L}/\mathcal{L} \sim$ 5–10% up to 1 TeV. On the right, the gluon uncertainty itself is displayed at the initial scale ($Q \sim 3$ GeV), and one observes a very rapid growth for $x > 0.2$–0.3. At LHC, we have essentially no prediction for gluon initiated processes above $M \sim 3$ TeV.

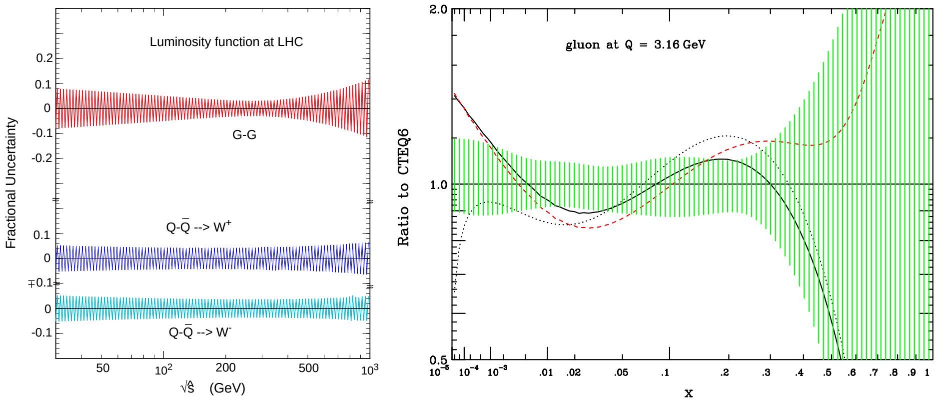

Fig. 11. Gluon–gluon luminosity and its uncertainty, as a function of $\sqrt{\hat{s}}$ [12].

The first way that comes to mind to improve the situation is the analysis of the jet cross-section itself. There are however several complications. First of all, as we said, the high mass or high $E_{\rm T}$ spectrum should, in principle, be avoided because the possible appearance of new physics effects in this region.

In addition, jet reconstruction involves many difficult experimental and theoretical issues. Jet reconstruction algorithms, and the experimental control of the jet energy scale and resolution both affect the shape of the measured M and $E_{\rm T}$ spectra. The study presented in [29] assesses the improvement on the gluon density from the analysis of dijet events. Fig. 12 displays a projected dijet mass spectrum measurement, including the jet energy scale uncertainty.

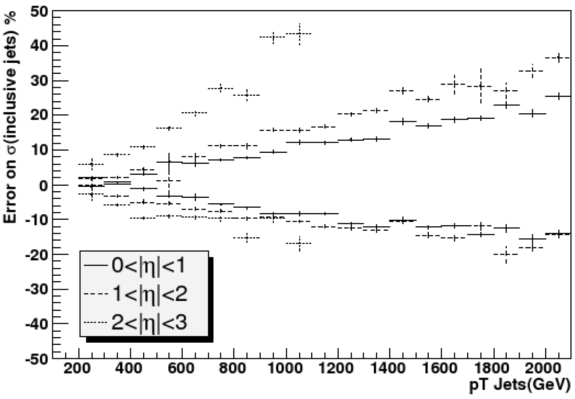

Fig. 12. Expected measurement precision of the dijet mass spectrum as a function of m_{JJ}, for three rapidity regions [29].

Although the statistical sensitivity is almost asymptotical, a jet energy scale of a few percent already limits the exploitation of the measurement result in terms of physics. Consequently, the improvement on the gluon density from this process is rather modest as shown in Fig. 13, unless the JES uncertainty can be constrained to about 1% above $E_{\rm T} \sim 1\,{\rm TeV}$ — a challenging problem.

A complementary approach is to exploit direct photon spectra. While the leading order cross-sections $q\bar{q} \rightarrow g\gamma/\gamma\gamma$ are coupled to quarks, the box processes $gg \rightarrow g\gamma/\gamma\gamma$ are not strongly suppressed, and enhanced by the very large gluon density. As a result, the gluon initiated process dominates the overall rate at the LHC. Moreover, since the quark densities are much better known than the gluon density, the box process carries essentially all the uncertainty. As a result, direct photons provide a sensitive probe to the gluon PDF.

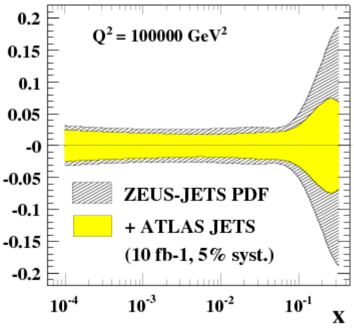

Fig. 13. Expected improvement on the gluon density from the analysis of dijet events at the LHC.

Another advantage of this process is the reduced sensitivity to the jet observables. Photon reconstruction does not involve theoretically sensitive algorithms, and the precision on the photon energy scale will reach 1% or better [30]. While completely jet-free, direct photon pairs have a low cross-section, and potentially the same physics bias as dijets, since non resonance extra-dimension effects can appear through direct photon pairs as well.

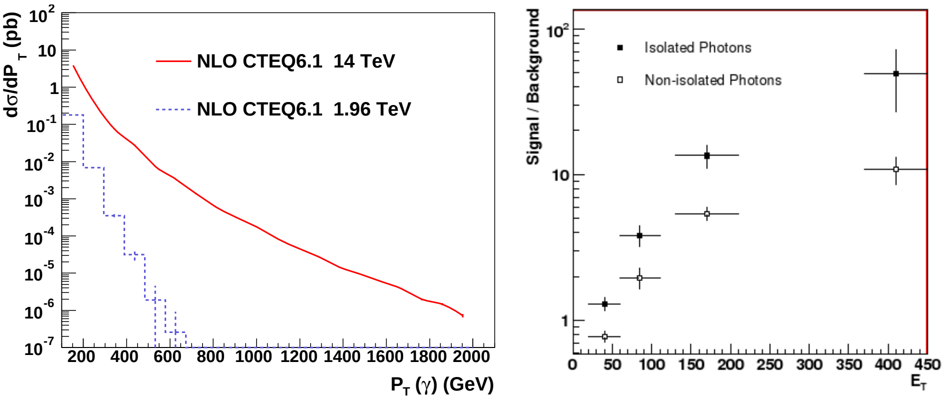

Fig. 14. Left: expected direct photon production cross-section, at Tevatron and LHC. Right: signal-to-background ratio, as a function of E_{T}.

Photon–jet processes are a convenient midway. The cross-section is sufficient and extra-dimensional new physics are unlikely to provoke an effect in this final state. Jet reconstruction difficulties can be circumvented if one restricts the analysis to the photon E_{T} spectrum. Fig. 14 illustrates the expected cross-section of the direct photon E_{T} spectrum at LHC, in comparison with Tevatron, and the experimental separation between photon and jets as a function of their transverse energy. As can be seen, the signal purity is adequate in the high-E_{T} region where this measurement is relevant.

Note that while photons of moderate transverse energy, $E_{\mathrm{T}} \sim 50\,\mathrm{GeV}$, such as those expected from Higgs boson decays, have important backgrounds from jets (the expected signal-to-background ratio is ~ 1), the background rate decreases rapidly with E_{T}. Above $E_{\mathrm{T}} > 500\,\mathrm{GeV}$, the photon sample is sufficiently pure [31], with a signal-to-background ratio in excess of 10^2, not to affect the interpretation significantly.

Finally, weak boson production provides another robust probe of the gluon density. While naïvely a quark-induced process, the process receives significant gluon-induced contributions at finite p_{T}. The hard processes $q\bar{q} \to Zg$ and $qg \to Zq$ are of similar magnitude *per se*, but the larger gluon density favours the second. Again, because of the better knowledge of the quark density, the gluon initiated process carries essentially all the uncertainty and hence the potential to constrain the gluon density. This is illustrated in Fig. 15 on the similar example of Drell–Yan production at the Tevatron, where for virtualities of $Q \sim 5$–$30\,\mathrm{GeV}$, and lepton pair p_{T} above 10 GeV the gluon initiated process dominates [32].

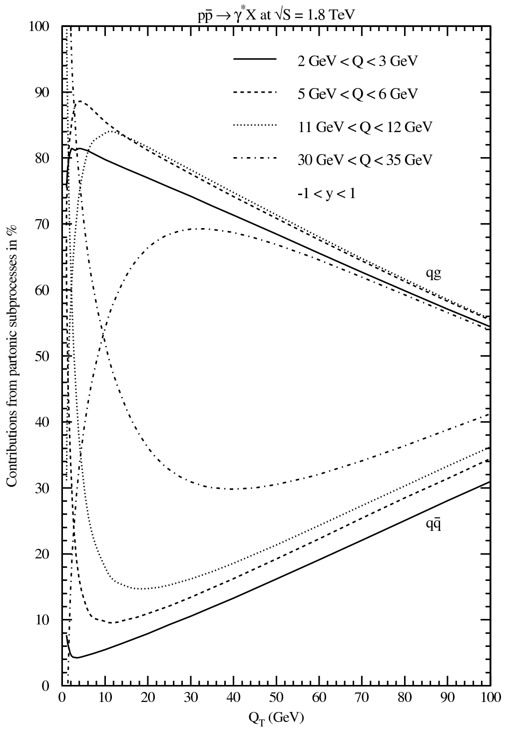

Fig. 15. $q\bar{q}$ and qg contributions to the $\gamma^* \to l^+l^-$ production cross-section at the Tevatron, as a function of p_{T} and for different Q [32].

As above, jet reconstruction issues can be avoided by measuring only the leptonic system. In Z events, the electron or muon pair momentum allows to select the high-$p_{\rm T}$ region; in W events, one has to rely on missing transverse energy as well, making this process experimentally more complicated.

As we will see in the next section, the vector boson $p_{\rm T}$ distribution is uncertain not only due to PDF uncertainties *sensu stricto*, but also due to the mechanisms of repeated soft gluon emission. However, this particular uncertainty mostly concerns the region of moderate transverse momentum, $p_{\rm T} < 50$ GeV. Above this threshold, the spectrum is not affected any more by resummation effects and can be used to constrain the gluon density.

3.3. Observables less sensitive to the uncertainties on the gluon density

Another idea complementary to the discussion we just had about further constraining the gluon density in the proton is to find other observables which are less sensitive to PDF uncertainties but still to beyond standard model effects. We will just quote one example of such observables $\chi_{\rm dijet}$, related to the jet angular distribution [33] in dijet events:

$$\chi_{\rm dijet} = \exp(|y_1 - y_2|) = \frac{1+\cos\theta^*}{1-\cos\theta^*}\,, \tag{4}$$

where y_1, y_2 are the rapidities of the two jets and θ^* is the center-of-mass scattering angle. The expected distributions are given in Fig. 16 for Rutherford scattering, QCD and new physics (compositeness, extra-dimensions ...). The distribution is flat for Rutherford scattering, slightly shaped for QCD, and strongly enhanced at low $\chi_{\rm dijet}$ in the case of quark compositeness or extra-dimensions. The idea is thus to measure normalised distributions as a function of $\chi_{\rm dijet}$ as the one shown in Fig. 16 since experimental and theoretical (mainly PDF related) uncertainties cancel. This observable is a direct

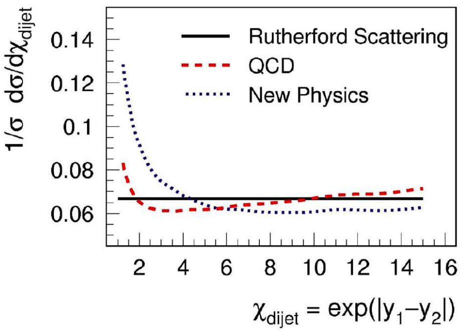

Fig. 16. $\chi_{\rm dijet}$ distribution for Rutherford scattering, QCD calculations and new physics (compositeness, extra-dimensions ...).

way to assess beyond standard model effects such as compositeness or extra-dimensions without suffering from the uncertainties of the gluon density at high x. On the contrary, the dijet mass cross-section is, of course, sensitive to such beyond standard model effects as an example, but is directly sensitive to PDF uncertainties as well.

3.4. Summary on the gluon density

The discovery potential of new particles in gluon-initiated processes is not strongly affected for moderate masses, up to $m \simeq 1\,\mathrm{TeV}$. We gave the example of the Higgs boson search, but the same conclusions hold for supersymmetric particle searches.

For higher masses, the sensitivity is strongly limited by the gluon PDF uncertainty. At, or above $m \simeq 2\,\mathrm{TeV}$, PDF uncertainties are in excess of 50% and prevent the interpretation of the observed spectra in terms of new physics. A possible way out is to use dijet angular distributions.

We have argued that jet measurements themselves are difficult to exploit in constraining the PDFs due to jet reconstruction difficulties, and the danger to absorb non-resonant new physics into the PDFs. However, events with photons are better determined experimentally (in particular the energy scale). Photon–jet events avoid large classes of non-resonant new physics, and the photon E_{T} spectrum in these events constitute a robust probe of the gluon PDFs. To avoid backgrounds, the high transverse energy range ($E_{\mathrm{T}} > 300$–$500\,\mathrm{GeV}$) should be favoured.

The range $50 < p_{\mathrm{T}} < 300$–$500\,\mathrm{GeV}$ can be covered by events with weak bosons. Avoiding the low p_{T} region affected by resummation uncertainties, these samples have low backgrounds and benefit from precise reconstruction, making them good probes of the gluon density.

4. The quark densities in the proton

In this section, we will discuss the uncertainties related to the quark densities in the proton. As in the previous section, we will follow two different approaches: how are the searches at LHC dependent on the quark density uncertainties and are there clever observables reducing their impact, as well as how can the knowledge of quark PDFs be improved at LHC?

4.1. W and Z production

The W and Z production cross-sections (and their ratios) are often regarded as precise tests of QCD. Indeed, the available NNLO calculations [34] claim residual uncertainties below 1%.

However, it is worthwhile to mention the evolution of the W and Z cross-section predictions with recently published PDF sets. The CTEQ Collaboration has produced several sets with different underlying assumptions. A summary is proposed in Fig. 17 [35, 36].

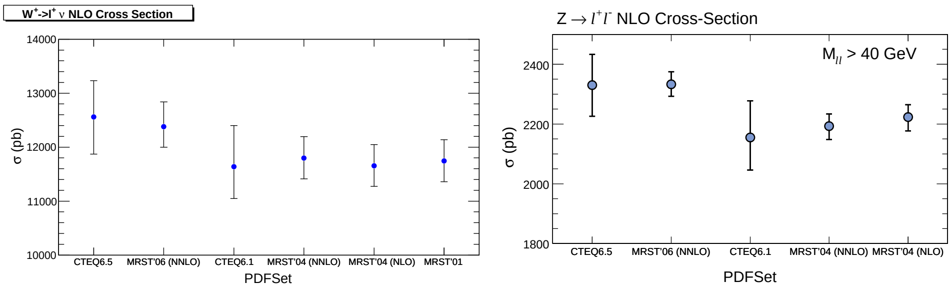

Fig. 17. W and Z total cross-sections and their uncertainties, as predicted by different PDF sets [35, 36].

Compared to CTEQ6.1, CTEQ6.5 [37] introduced a formalism accounting for the masses of heavy flavour initial quarks, resulting in an 8% increase of the W and Z cross-sections. While it is argued that this number should not be taken as an uncertainty, the theoretical framework is not unique.

In the most recent set, CTEQ6.6 [7], the assumption that the strange quark density is given by the u and d sea quark densities, $s = \bar{s} = \kappa(\bar{u} + \bar{d})$, was released. This resulted in another increase of the cross-sections by about 2–3%. Again, the net increase should not be regarded as an estimate of the uncertainty, but it is well known that the strange quark density is poorly constrained, and the question arises whether the analysis of Ref. [7], and in particular the choice of the strange quark initial parametrisation and the assumption $s = \bar{s}$ allows to fully reflect the uncertainty related to this flavour.

The release of the strange quark density plays a particular role in the W/Z cross-section ratio. Indeed, as shown in Fig. 18, this ratio was particularly stable in all previous PDF sets. As can be seen, all shown predictions of this ratio are compatible with each other (CTEQ or MRST; LO, NLO or NNLO evolution), except the prediction of CTEQ6.6. The free strange quark density decorrelates W production from Z production. Note also that the CTEQ6.6 prediction agrees better than earlier CTEQ versions with predictions by other groups. This agreement might be coincidental, since the other groups all assume fixed strangeness. This issue remains to be clarified.

From the above examples, it appears that W and Z production, and even their ratio, are very sensitive to the details of the proton PDFs. An interpretation of these measurements in terms of genuine QCD (*i.e.* α_S corrections to the hard process) is thus difficult, pending significant improvements.

As shown by the ratio example, the problems do not come from the limited perturbative expansion of the PDF evolution, but rather from the starting assumptions, in particular the strange quark density in the low-Q^2 proton.

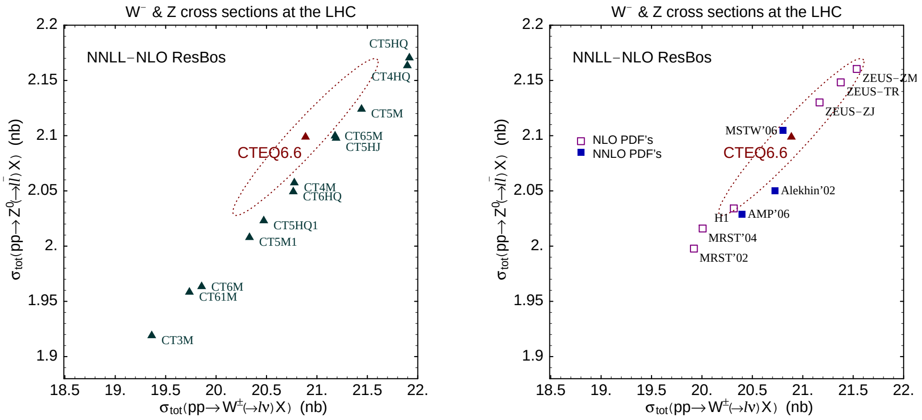

Fig. 18. Correlation between the W and Z total cross-sections, as predicted by several PDF sets [7, 12, 38, 39].

A more intricate example is given by W and Z $p_{\rm T}$ distributions. While not purely a PDF problem, the gluon emissions are determined by the Sudakov form factors, which in turn are PDF integrals. The fact that W and Z couple to different initial partons creates again subtle differences between

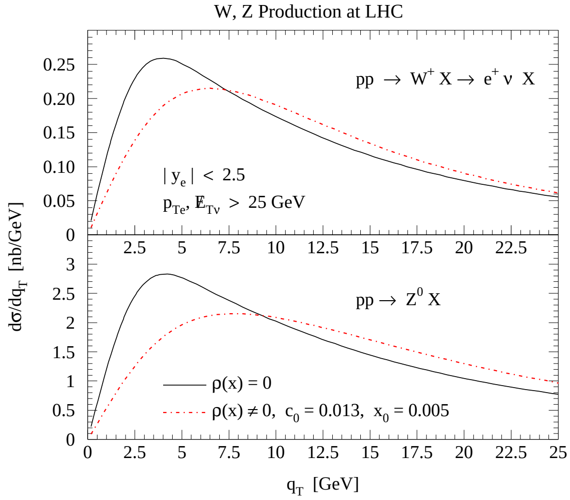

Fig. 19. W $p_{\rm T}$ distribution in the absence or presence of non-perturbative contributions to the soft gluon resummation [40].

the two processes. This distribution can also exhibit uncertainties related to the evolution itself; at low x, BFKL-like evolution can generate additional "broadening" of the p_{T} distribution, as illustrated in Fig. 19 [40].

4.2. Precision electroweak measurements

The program of testing the SM at the quantum level, through precise measurements of the electroweak parameters, will be pursued at LHC. Improvements in the measurements of notably m_W and m_{t} will result in improved predictions for the Higgs boson mass; predictions which hopefully be confronted to the observed value of m_H.

The W mass measurement is affected by PDFs through acceptance effects. Unlike the cross-section example, the PDF normalisation is irrelevant; however, their x-dependence determines the W rapidity distribution. The kinematical distributions of the W sample that passes acceptance cuts are thus affected. As a result, the distributions that enter the measurement of m_W, *i.e.* the transverse momentum of the charged decay lepton, $p_{\mathrm{T}}(l)$, and the transverse mass of the lepton–neutrino pair, can be mis-modeled, and this mis-modeling can be wrongly absorbed in the mass measurement.

The LHC prospects for the measurement of M_W have been discussed in [41, 42]. With current data, the PDF uncertainties include a systematic uncertainty on M_W of about 25 MeV, *cf.* Fig. 20.

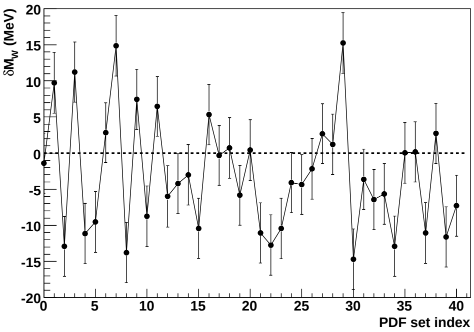

Fig. 20. Expected shift on the fitted value of m_W, for PDF sets differing from the best fit by one standard deviation in each of the free parameters. Biases are shown as predicted by CTEQ6.5. The total systematic uncertainty is essentially obtained from the quadratic sum of all biases, and amounts to 25 MeV [42].

The desired precision on m_W is much better. The statistical sensitivity is below 2 MeV, and given the current precision on the top quark mass, an uncertainty $\delta m_W \sim 10\,\mathrm{MeV}$ is desirable. Therefore, such a PDF uncertainty is prohibitive.

As shown in [42] (*cf.* also Fig. 21, left), the situation can be greatly improved by measuring the Z boson rapidity distribution at LHC, and exploiting the expected correlation of these distributions between W and Z events. In first approximation, the measurement of the Z rapidity distribution constrains the W one to the point of reducing the PDF systematic ucertainty to below 1 MeV.

However, as for the cross-sections, this picture is questioned by the CTEQ6.6 PDF sets. As shown in Fig. 21, right, the free strange quark density produces a decorrelation between W and Z distributions which partly obscures the interpretation of the Z rapidity distribution. It is remarkable that three fits with very different theoretical assumptions (CTEQ61 — NLO; CTEQ65 — with improved heavy quark treatment, and MSTW2006 — NNLO), but identical hypotheses on the initial proton parametrisation, reach the same result, whereas the CTEQ66 prediction, with its strange quark degrees of freedom, is significantly different.

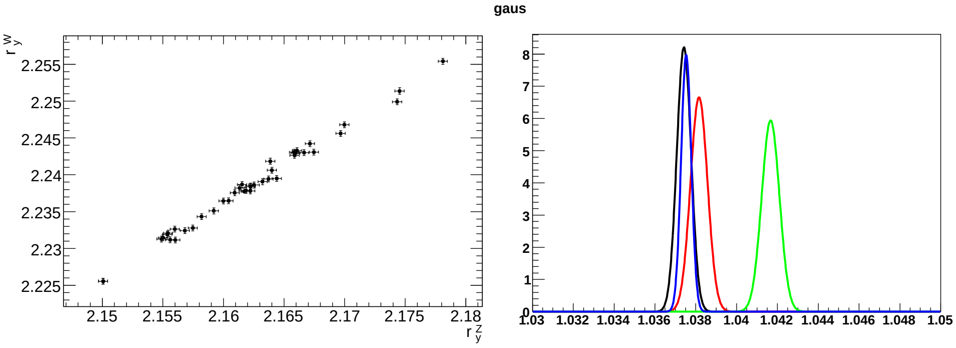

Fig. 21. Left: spread (RMS) of the rapidity distributions of W *versus* Z events, plotted for the 41 CTEQ6.1 PDF sets [42]. Right: ratio of these spreads for W and Z, as predicted by, from left to right, CTEQ61 [12], CTEQ65 [37], MSTW2006 [38], and CTEQ66 [7].

4.3. Heavy gauge bosons

If new, heavy gauge bosons exist and are related to the electroweak symmetry breaking, their mass should be in the TeV range and accessible at LHC [1,3]. In addition to the determination of their mass, which can be performed through a straightforward determination of the peak position in the invariant mass or transverse mass spectra, it is also important to determine their couplings as well as possible. This can, in principle, be done through a more difficult analysis of the lineshape, determining the interference pattern with the gauge bosons of the Standard Model. Such analyses would be reminiscent of the LEP2 $e^+e^- \to f\bar{f}$ cross-section measurements [43] which, providing data with a precision of about 1%, put stringent constraint on such new physics. For these to succeed at LHC, the standard model reference cross-section should thus be known with a precision not worse than 1%.

As can be seen in Fig. 22 [44], the PDF uncertainty in the mass range $M \sim 1\,\text{TeV}$ is about 3%. While not affecting the discovery potential, such uncertainties are too strong for the precision measurements mentioned above to be performed. It is thus desirable to reduce these uncertainties by a factor 3 or more.

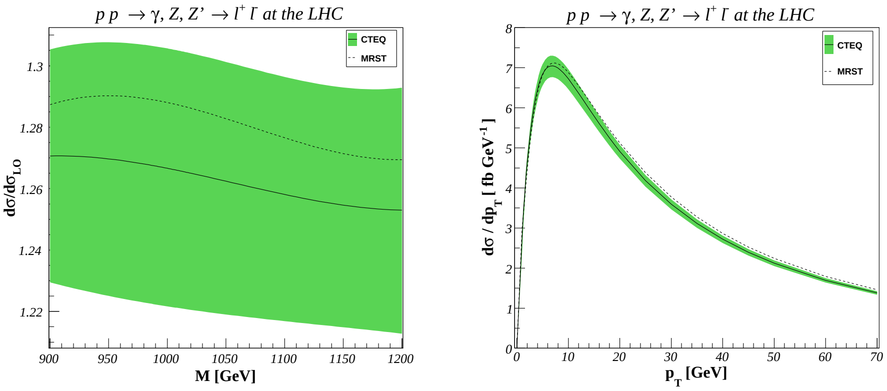

Fig. 22. Left: high-mass Drell–Yan cross-section and its uncertainty, in the region $m_{l^+l^-} \sim 1$ TeV. Right: expected $p_{\rm T}$ distribution in this region, and its uncertainty.

This can be obtained by constraining the relevant x range, through a combination of measurements of high-rapidity Z boson events, and of the low-mass Drell–Yan spectrum. It will be discussed in Section 5.5.

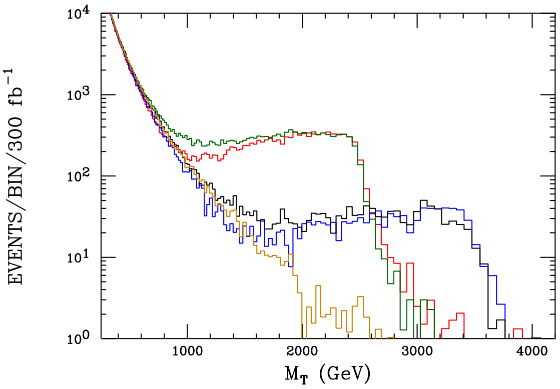

Fig. 23. Transverse mass distributions of heavy W' bosons, for different mass and helicity hypotheses. The lower curve represents the Standard Model background, and the two pairs of curves correspond to $m_{W'} = 2.5$ and 3.5 TeV, plotted for $\lambda = \pm 1$.

A similar measurement was suggested in [45], which proposes a determination of the W' helicity, via a measurement of the transverse mass distribution well below the W' peak, as illustrated in Fig. 23. While the new Jacobian peaks are clearly visible, additional model discrimination can be obtained through an analysis of the M_{T} distribution well below the peak. Here again, it is necessary to dispose of precise Standard Model benchmarks, and similar arguments as above hold.

4.4. Summary: opportunities for improvements at the LHC

In the previous section we have illustrated the impact of the PDF uncertainties on prominent example of the LHC physics programme. Many of the questions raised could hopefully be improved at LHC using dedicated analyses. The cleanest way to improve on the gluon distribution, in the high-x region, is provided by the analysis of high-E_{T} direct photon production. In the low-x region, the study of high-p_{T} vector boson production is easier and avoids the jet background when lower E_{T} photons are used. Jet production will provide useful information, but is subject to difficulties related to the jet reconstruction. The sea quark distributions will be constrained *via* measurements of W and Z boson production at low transverse momentum. The valence distributions are discussed in Section 5.

Improving the knowledge on the s, c and b quark content of the proton will need more specific measurements. While these are not new ideas, there exists almost no literature on these subjects and it is worthwhile to draw the attention to their importance.

The strange quark contents of the proton can hopefully be constrained exploiting the associated production of W boson with charm. This process is dominantly produced through $sg \rightarrow cW$, hence sensitive to the strange quark density. The process is experimentally difficult to select, and in practice the c-jet can be identified through the presence of specific D^* decays. This mode provides sufficient purity, but at the cost of a low efficiency. Further study is needed to establish whether this process can be exploited.

The cleanest way to access the c and b densities is through $cg, bg \rightarrow cZ, bZ$. The charm jet can be identified as above. B jets are selected with good efficiency and purity using b-tagging, but the measurement can be obscured by background processes like $q\bar{q} \rightarrow Zg$, with subsequent "gluon splitting" $g \rightarrow b\bar{b}$ (this background is also present in the charm final states).

Such analyses have been pursued at Tevatron [46]. The higher statistics at LHC should provide good prospects, but the experimental and theoretical difficulties remain to be quantified.

5. Another way to be less sensitive to PDFs: cross-section ratios

In this section, we will discuss another method to reduce the influence of PDF uncertainties (both quark and gluons) by considering ratio of cross-sections in a well chosen given kinematical domain. It follows somehow the idea of the $\chi_{\rm dijet}$ observable but the discussion will be more complicated since the aim will be here to define and choose ratios showing a dependence on PDFs as low as possible.

Measuring ratios of quantities are interesting from an experimental point of view because correlated systematic uncertainties may cancel. It can also provide more accurate information on PDFs since some processes use the parton densities in the same x or $(x,\, Q^2)$ region. In a ratio of quantities related to these processes, the influence of PDFs could cancel. Another motivation for using ratios is to separate the effects due to new physics from the ones due to insufficient knowledge of the PDFs. In this section, we develop some measurements based on ratios, for which the sensitivity to PDFs is reduced. Such measurements at LHC directly probes and then constrains the remaining PDF contribution: W charge asymmetry, Z forward–backward asymmetry, W over Z cross-section ratio, boson pair over single boson cross-sections ratio and Drell–Yan cross-sections ratio.

5.1. W charge asymmetry

The W charge asymmetry quantifies the imbalance between positive or negative W bosons, produced at a given rapidity y_W:

$$\mathcal{A}_W(y_W) = \frac{d\sigma(W^+)/dy_W - d\sigma(W^-)/dy_W}{d\sigma(W^+)/dy_W + d\sigma(W^-)/dy_W}\,.$$

At LHC, the W-charge asymmetry can be linked to structure functions in a simple manner. In first approximation, W bosons are mostly produced by up and down quarks and $\sigma(W^+)$ can be written as: $\sigma(W^+) = (u_{\rm val} + u_{\rm sea})\bar{d}_{\rm sea} + q_{\rm sea}\bar{q}'_{\rm sea}$. Replacing this information in the definition above, and under the approximation that the sea quark content of the proton is the same for u, d, s, c quarks, one gets the following result:

$$\mathcal{A}_W(y_W) = \frac{u_{\rm val} - d_{\rm val}}{u_{\rm val} + d_{\rm val} + 2q_{\rm sea}}\,(x)\,.$$

At leading order, the W charge asymmetry directly probes the difference between valence quarks. From the experimental side, it is preferred to measure the lepton-charge asymmetry because the W boson cannot be fully reconstructed from its decay leptons. In this experimental ratio, the relation between PDFs and W charge asymmetry is more complex but it still provides complementary measurements of valence PDFs.

The predictions of the lepton-charge asymmetry have large uncertainties due to the lack of data on valence quantities for both high- and small-x values. At high lepton rapidity, the different predictions using CTEQ6.1, MRST2001 or ZEUS-S PDFs are compatible but the uncertainty on the ratio is large ($\sim 10\%$) as shown in Fig. 24. On the contrary, for centrally produced W bosons, a 4-σ discrepancy is present between the different W charge asymmetry predictions using CTEQ6.1, MRST2001 or ZEUS-S PDFs [48]. The input parametrisation of u_v/d_v at Q_0^2 in global QCD fits could be improved with such measurement at LHC.

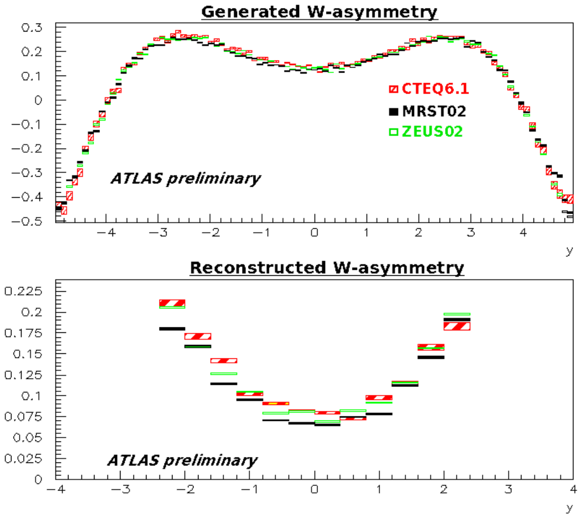

Fig. 24. Lepton charge asymmetry in W decay as a function of lepton rapidity, generated using HERWIG and CTEQ6.1 (dashed red) ZEUS-S (green) or MRST2001 (full black) PDF sets with full uncertainties, at the generator level (up) and after a fast simulation of ATLAS detector and reconstruction effects (bottom).

5.2. Z forward–backward asymmetry

The forward–backward asymmetry in Z events is an important measurement since it is sensitive to new physics effects and provides a determination of the mixing angle $\sin 2\theta_W$. The presence of both vector and axial-vector couplings of the quarks and leptons to the Z^*/γ^* boson gives rise to an asymmetry in the polar emission angle θ^* between the quark and the lepton in the Z^*/γ^* rest frame. The differential cross-section for the parton level process can be written:

$$\frac{d\sigma}{d\cos\theta^*}\left(q\bar{q} \to \frac{\gamma^*}{Z} \to l^+l^-\right) = \mathcal{A}\left(1+\cos^2\theta^*\right) + \mathcal{B}\cos\theta^* \,.$$

The weak interaction introduces the asymmetry ($\mathcal{B} \neq 0$), and $\mathcal{A}$ and B are functions of the weak isospin and charge of the incoming quarks and of the Z^*/γ^* invariant mass. The asymmetry is given by the direction of the Z with respect to the direction of the incoming quark, according to the definition below

$$\mathcal{A}_{\mathrm{FB}} = \frac{\sigma(Z)_{\cos\theta^*>0} - \sigma(Z)_{\cos\theta^*<0}}{\sigma(Z)_{\cos\theta^*>0} + \sigma(Z)_{\cos\theta^*<0}} \propto 1 - \mathcal{K}\sin^2\theta_W\left(M_Z^2\right) .$$

To measure the Z forward–backward asymmetry, it is necessary to tag the directions of the incoming quark and antiquark, which is a difficult task at LHC. Indeed, Z bosons are mostly produced by sea partons. The quark and antiquark PDFs are almost equal and the direction of the incoming quark is no longer related to the direction of the Z. This is not the case at high x, for which the incoming quark is rather a valence quark than a sea quark. This asymmetry between sea and valence quarks is useful to distinguish from which of the two protons the quark was coming. In order to produce a Z boson with a high-x quark, the antiquark must come from a low-x region. This produces a highly boosted Z boson with a high-rapidity, and the direction of the incoming quark is now correlated with the direction of the Z. These bosons can be used for forward–backward asymmetry measurements. However, since leptons from high-rapidity boosted Z bosons decay are at high pseudo-rapidity, they are likely to be reconstructed in the forward regions of the detectors. The analysis aiming at measuring this asymmetry needs to include the forward detectors, as shown in Fig. 25.

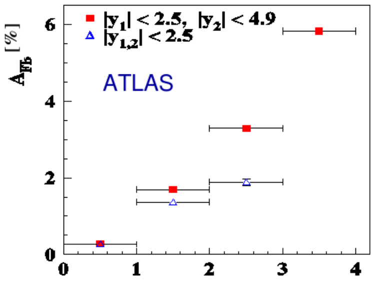

Fig. 25. Forward–backward asymmetry in $Z \to ee$ events *versus* the reconstructed Z rapidity, in the case where both electrons are reconstructed in the central region ($|\eta^e| < 2.5$), or where one electron is reconstructed in the forward calorimeter ($2.5 < |\eta^e| < 4.9$) and the other is central [2]. The analysis with two forward electrons does not lead to significant results because the rejection factor against fake electrons in the forward calorimeter may not be high enough and suffers from large systematic uncertainties.

Precise identification of forward leptons is then a difficult task, because of the high hadronic activity and because of the absence of tracking device. This requires a good understanding of forward physics, and the detector and reconstruction effects.

The main systematics come from the lepton acceptance and reconstruction efficiency and from the PDF uncertainties. Theese ones are quite large at high-x, and a measurement of $\mathcal{A}_{\mathrm{FB}}$ could directly constrain both $\sin^2\theta_W$ and the high-x valence PDFs.

5.3. W/Z production cross-sections ratio

W to Z bosons production cross-sections ratios are motivated by both experimental and theoretical aspects. At LHC, this ratio should have low statistical and systematic errors. Firstly, the selection of such events relies on isolated leptons in the same transverse momentum range, they can be selected by the same trigger condition, and the hadronic environment is expected to be similar. Many experimental uncertainties can cancel in such ratios of cross-sections. Secondly, both leading order processes are similar (quark initial state, singlet final state). Higher order corrections like initial state radiations, affect both processes in an equal way, and many theoretical uncertainties cancel in this ratio.

From the PDF side, W/Z production cross-sections ratio behave similarly under PDF variations because the $(x,\ Q^2)$ range is the same. The remaining PDF uncertainties are mostly due to the strange quark contribution. Indeed, Fig. 26 shows the correlation between $\sigma(Z)/\sigma(W^{\pm})$ and the PDF *versus* x for different partons at $Q = 85\,\mathrm{GeV}$. It indicates that a change of the gluon,

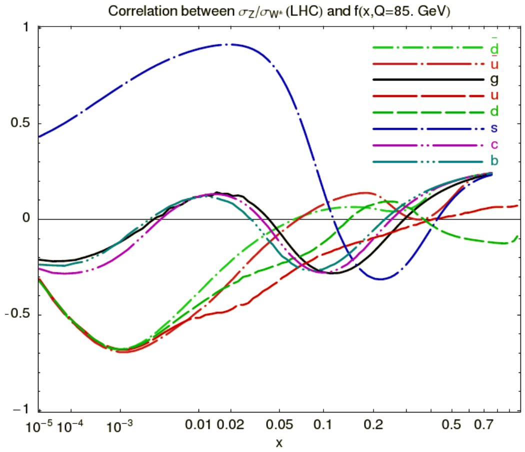

Fig. 26. Correlation between $\sigma(Z)/\sigma(W^{\pm})$ and the PDF *versus* x for different partons at $Q = 85\,\mathrm{GeV}$ (see text).

c and b quark PDF have little impact ($< 20\%$) on the ratio $\sigma(Z)/\sigma(W^{\pm})$ for the whole x range. The variations of light quark (u and d) PDFs have a higher effect on the W/Z production cross-sections ratio, especially at low x ($x < 0.1$) where they are anti-correlated. The higher correlation is obtained for the strange quark distribution in the region $x \sim 10^{-2}$, where it reaches 90%. At LHC, W and Z bosons are mainly produced with partons in this region. This means that the ratio of the total W and Z production cross-sections (integrated over x) is highly correlated with the proportion of strange quarks in the proton. In addition, since additional degrees of freedom are used to describe the strange quark PDF (in CTEQ6.6 for instance), the PDF uncertainty on the ratio is now greater than the expected experimental errors. As a consequence, a measurement of $\sigma(pp \to W^{\pm})/\sigma(pp \to Z)$ sets strong constraints of the strange quark parametrisation.

5.4. Ratio of boson pair over single boson production cross-sections

At LHC, pair production of weak bosons are one of the processes that might reveal some signs of new physics. Their production cross-section is quite low (3.5 pb for W^+W^- events in e or μ final states) compared to single W production, but this signal will be precisely studied. With a cross-section measured at the percent level, systematic uncertainties are expected to dominate the total error [2].

In order to reduce the effect of PDF uncertainties, the diboson cross-section can be normalised to the single weak boson cross-section [49]. For instance, W^+W^- cross-section is compared to the Z one. Indeed, these two processes are quite similar since W^+W^- bosons can be produced via an off-shell Z bosons: $q\bar{q} \to Z^* \to W^+W^-$. The initial state is the same as for Drell–Yan process: $q\bar{q} \to Z^*/\gamma^* \to e^+e^-$, leading to correlated higher order QCD corrections and PDF uncertainties. However, the scales, at which these processes are produced, are different and this is the reason why the cancellation of PDF uncertainty is not exact. This argument is also valid for $ZW^{\pm}$ or ZZ production, compared to $W^{\pm}$, but the statistical error will be larger.

5.5. Drell–Yan production cross-sections ratio

With millions of Z/γ^* produced with 1 fb^{-1} of LHC data, the statistical error on the Drell–Yan production cross-section is expected to be smaller than the percent. The limitation comes from systematics, among which a large error is due to PDF, around 6–8%, even at high mass $\mathrm{M} > 200\,\mathrm{GeV}/c^2$. The idea is to exploit the Z/γ^* mass and rapidity spectrum and to make ratios of cross-sections when the initial quarks have the same kinematics.

Let us consider a quark and anti-quark that produce a Z boson with a rapidity y. The momentum fractions of these partons are $x_1 = M_Z/\sqrt{s} \cdot e^{-|y|}$ and $x_2 = M_Z/\sqrt{s} \cdot e^{+|y|}$. But these momentum fractions can also be encountered in other γ^*/Z processes. Symetric $q\bar{q}$ collisions with two partons carrying the momentum fraction x_1 can produce γ^*/Z particles with the invariant mass $m = \sqrt{x_1 x_1 s} = M_Z \cdot e^{-|y|}$ and rapidity of 0. In the same way, symetric $q\bar{q}$ collisions with two partons carrying the momentum fraction x_2 can produce γ^*/Z particles with the invariant mass $M = \sqrt{x_2 x_2 s} = M_Z{\cdot}e^{+|y|}$ and rapidity of 0. In other words, the same quark momenta have been found in three cross-sections: $\sigma_{Z/\gamma^*}(M_Z, y)$, $\sigma_{Z/\gamma^*}(m, y\,{=}\,0)$ and $\sigma_{Z/\gamma^*}(M, y\,{=}\,0)$, where $y = \ln M/M_Z$ and $m = M_Z^2/M$. Uncertainties on quark kinematics could be reduced in the following ratio, involving these three cross-sections:

$$R(M) = \frac{\sigma(m, y=0)\,\sigma(M, y=0)}{\sigma^2(M_Z, y)}\,,$$

where $y = \ln M/M_Z$ and $m = M_Z^2/M$.

With only one quark flavour and with scale invariance, the PDF completely cancel and so their uncertainties. This is no longer valid in the real case but the prediction of $R(M)$ is still more precise than the high mass Drell–Yan cross-section $\sigma(M)$. Fig. 27 shows how these errors vary for different Z/γ^* invariant masses. The PDF uncertainties can be reduced by more than a factor two, leading to a higher sensitivity to non-Standard Model processes.

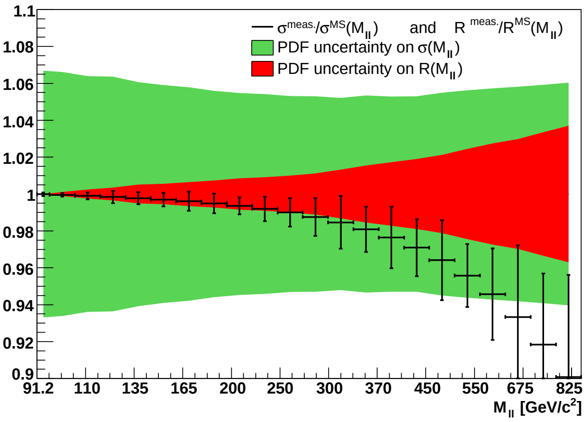

Fig. 27. Pseudo-measurement to Standard Model prediction ratios of $\sigma_{Z/\gamma^*}(M)$ or $R(M)$ with statistical error bars. The pseudo-measurements use 30 fb^{-1} of LHC data, and a 2 TeV SSM Z' have been added in the simulation. The central values of these two measurements are the same and the statistical uncertainties are very close, so only one set of error bars is shown. The uncertainty bands due to PDF on $\sigma_{Z/\gamma^*}(M)$ and $R(M)$ are also represented.

An example of new physics sensitivity is shown in Fig. 27. Pseudo-measurement of $\sigma_{Z/\gamma^*}(M)$ and $R(M)$, including a 2 TeV SSM Z' are compared to the Standard Model predictions. The statistical and PDF-induced uncertainties are also displayed. A measurement of $R(M)$ shows a sensitivity of a 2 TeV SSM Z' since $M > 200\,\mathrm{GeV}/c^2$, while in a $\sigma_{Z/\gamma^*}(M)$ cross-section analysis, no significant deviation is seen, except for $M > 600\,\mathrm{GeV}/c^2$. Thus, it seems possible to explore a larger range of Z' models, that may not be discovered by direct peak searches like non-resonant or wide Z'.

This method has other advantages. If a Z' peak is observed, this ratio of cross-sections can be used to measure the $\gamma^*/Z/Z'$ interference term at lower masses, in order to give additional constrains to the underlying Z' model. Finally, this method can be applied to any s-channel processes like $W^\pm$ production. W' searches or s-channel single-top cross-sections can be normalised to $W^\pm \to l\nu$ to obtain more precise measurements.

5.6. Summary

At LHC, most measurements will be limited by systematic uncertainties. Experimental systematics can be reduced in ratios of quantities. In this section, appropriate ratios have been presented because their sensitivity on theoretical uncertainties has been reduced compared to individual cross-sections. The total error is reduced at a few percent level, showing that precision measurements at hadron colliders are possible.

6. Beyond the DGLAP evolution equation: looking for BFKL and saturation effects

In this section, we will face another aspect: we discuss potential issues with respect to the standard DGLAP [4] QCD evolution equation which is used in standard PDF analysis, and dedicated observables which can show effects beyond the standard DGLAP equation. There will be two different parts: we will first discuss potential observables sensitive to the missing $\log 1/x$ terms in the DGLAP evolution equation and included in the BFKL equation [5], and second, the possible influence of the saturation phenomenon at the LHC.

6.1. Looking for BFKL effects at the LHC: Mueller–Navelet jets

While it is well known that the BFKL [5] low-x resummation is not required in inclusive cross-section measurements such as the proton structure functions at HERA or jet cross-sections at Tevatron and LHC (but may be needed to determine the parton distributions at the initial scale Q_0^2), the situation is quite different if one looks in a given phase space where the $\log 1/x$ terms become important. This is the case, for instance, when one considers forward jet production at HERA. The idea is quite simple: one considers jet production as far away as possible in rapidity from the scattered electron, and the transverse energy of the jet is requested to be close to the Q^2 of the virtual photon. Because of the k_{T}-ordering of the gluons along the ladder for the DGLAP evolution equation, the cross-section predicted by the DGLAP evolution is small. On the contrary, the BFKL evolution equation predicts much higher cross-sections compatible with the experimental observations since there is enough phase space to produce many gluons [50, 51]. We will just quote one of the significant forward jet measurements performed at HERA, the measurement of the triple differential cross-section in the H1 Collaboration. The triple differential cross-section $d\sigma/dx\,dk_{\mathrm{T}}^2\,dQ^2$ shown in Fig. 28 is an interesting observable as it has been measured in 9 different p_{T}^2 and Q^2 regions where p_{T} is the transverse momentum of the forward jet.

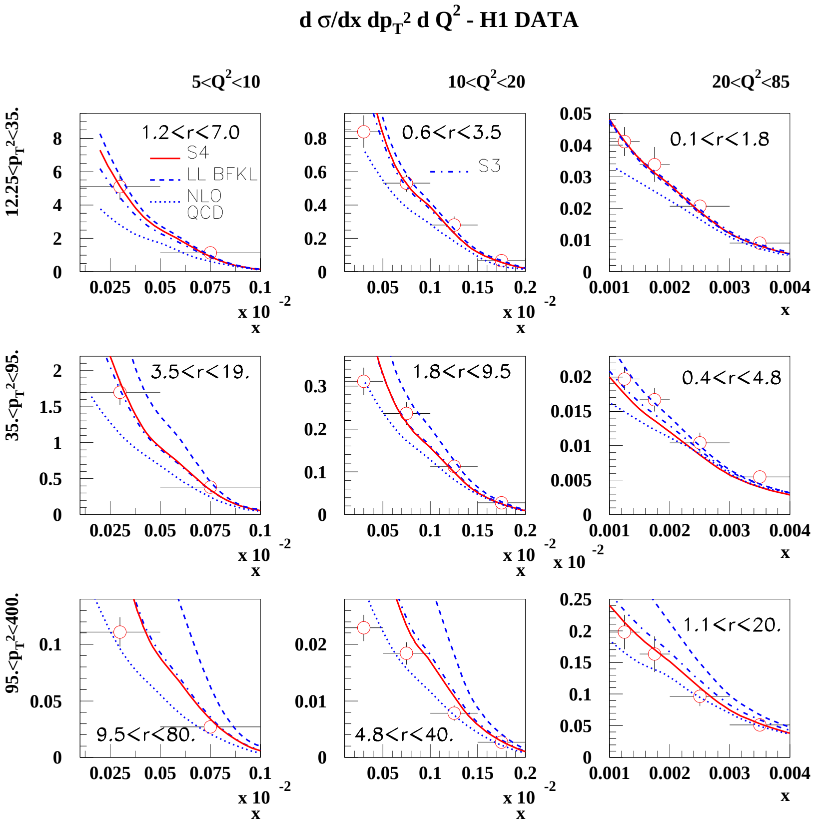

Fig. 28. Comparison between the H1 measurement of the triple differential cross-section with predictions for BFKL–LL, BFKL–NLL and DGLAP NLO calculations (see text).

The H1 data are compared to NLO DGLAP calculations which fail to describe the data in the low p_{T} region when $r = p_{\mathrm{T}}^2/Q^2$ is close to 1, precisely in the region where BFKL resummation effects are expected to be large. Fig. 28 also shows the BFKL-LL predictions which fail to describe the data when r goes away from 1. On the contrary, the BFKL NLL calculation[2] including the Q^2 evolution via the renormalisation group equation leads to a good description of the H1 data on the full range. We note that the higher order corrections are small when $r \sim 1$, when the BFKL effects are supposed to dominate. By contrast, they are significant as expected when r is different from one, *i.e.* when DGLAP evolution becomes relevant.

At hadronic colliders, similar processes can occur for the so-called Mueller–Navelet jets which are ideal processes to study BFKL resummation effects [53]. Two jets with a large interval in rapidity and with similar transverse momenta are considered. For this kind of events, the cross-section predicted by the DGLAP evolution is small because of the k_{T}-ordering of the gluons along the ladder. The BFKL cross-section can be large because there is enough phase space to emit the gluons. A typical observable to look for BFKL effects is the measurement of the azimuthal correlations between both jets. The DGLAP prediction is that this distribution should peak towards π — *i.e.* jets are back-to-back- whereas multi-gluon emission via the BFKL mechanism leads to a smoother distribution. The relevant variables to look for azimuthal correlations are the following:

$$\begin{aligned} \Delta\eta &= y_1 - y_2\,, \\ y &= (y_1 + y_2)/2\,, \\ Q &= \sqrt{k_1 k_2}\,, \\ R &= k_2/k_1\,. \end{aligned}$$

The azimuthal correlation for BFKL reads:

$$2\pi\,\frac{d\sigma}{d\Delta\eta dR d\Delta\Phi}\bigg/\frac{d\sigma}{d\Delta\eta dR} = 1 + \frac{2}{\sigma_0(\Delta\eta, R)}\sum_{p=1}^{\infty}\sigma_p(\Delta\eta, R)\cos(p\Delta\Phi)\,,$$

where in the NLL BFKL framework,

$$\begin{aligned} \sigma_p = &\int\limits_{E_{\mathrm{T}}}^{\infty}\frac{dQ}{Q^3}\alpha_{\mathrm{s}}\left(\frac{Q^2}{R}\right)\alpha_{\mathrm{s}}\left(Q^2R\right)\left(\int dy x_1 f_{\mathrm{eff}}\left(x_1, \frac{Q^2}{R}\right)x_2 f_{\mathrm{nll}}\left(x_2, Q^2R\right)\right) \\ &\times \int\limits_{1/2-\infty}^{1/2+\infty}\frac{d\gamma}{2i\pi}R^{-2\gamma}\,e^{\bar{\alpha}(Q^2)\chi_{\mathrm{nll}}(p,\gamma,\bar{\alpha})\Delta\eta}\,. \end{aligned}$$

---

[2] The BFKL NLL calculation were performed using two different schemes called S3 and S4 used to remove spurious singularities of the BFKL NLL calculation [52].

χ_{nll} is the effective resummed NLL BFKL kernel, and f_{eff} are the effective parton densities in the proton. As expected, the $\Delta\Phi$ dependence is less flat than for BFKL LL and is closer to the DGLAP behaviour [53]. In Fig. 29, we display the observable $1/\sigma d\sigma/d\Delta\Phi$ as a function of $\Delta\Phi$ for LHC kinematics. The results are displayed for different values of $\Delta\eta$ and at both LL and NLL accuracy. In general, the $\Delta\Phi$ spectra are peaked around $\Delta\Phi = 0$, which is indicative of jet emissions occuring back-to-back. In addition the $\Delta\Phi$ distribution flattens with increasing $\Delta\eta = y_1 - y_2$. Note the change of scale on the vertical axis which indicates the magnitude of the NLL corrections with respect to the LL-BFKL results.

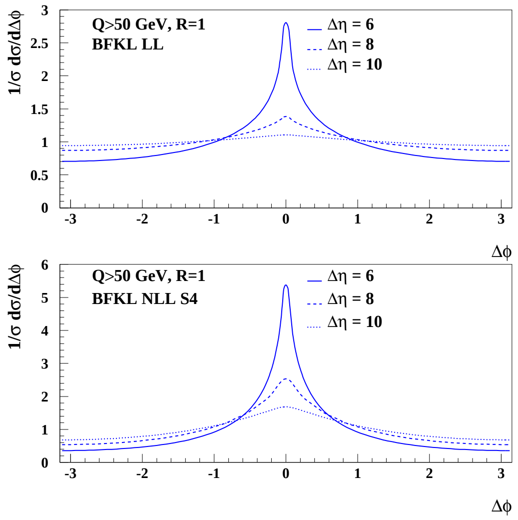

Fig. 29. The Mueller–Navelet jet $\Delta\Phi$ distribution for LHC kinematics in the BFKL framework at LL (upper plots) and NLL-S4 (lower plots) accuracy for $\Delta\eta = 6, 8, 10$.

A measurement of the cross-section $d\sigma^{hh\to JXJ}/d\Delta\eta dR d\Delta\Phi$ at the Tevatron (Run 2) or in the future at LHC will allow for a detailed study of the BFKL QCD dynamics since the DGLAP evolution leads to much less jet angular decorrelation (jets are back-to-back when R is close to 1). In particular, measurements with values of $\Delta\eta$ reaching 8 or 10 will be of great interest, as these could allow to distinguish between BFKL and DGLAP resummation effects and would provide important tests for the relevance of the BFKL formalism.

To illustrate this result, we give in Fig. 30 the azimuthal correlation in the CDF acceptance. The CDF Collaboration installed the mini-Plugs calorimeters aiming for rapidity gap selections in the very forward regions and these detectors can be used to tag very forward jets. A measurement of jet p_{T} with these detectors would not be possible but their azimuthal segmentation

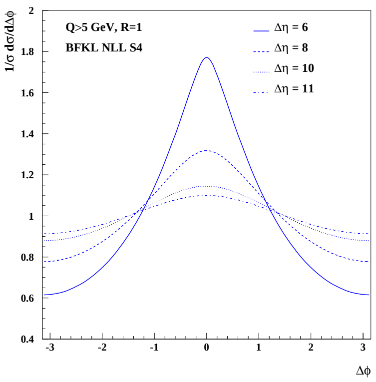

Fig. 30. Azimuthal correlations between jets with $\Delta\eta = 6$, 8, 10 and 11 and $p_{\rm T} > 5$ GeV in the CDF acceptance. This measurement will represent a clear test of the BFKL regime.

allows a ϕ measurement. In Fig. 30, we display the jet azimuthal correlations for jets with a $p_{\rm T} > 5$ GeV and $\Delta\eta = 6$, 8, 10 and 11. For $\Delta\eta = 11$, we notice that the distribution is quite flat, which would be a clear test of the BFKL prediction. Mueller–Navelet jets might also be a possible way to look for saturation effects [50] when jets are widely separated in rapidity.

Another measurement sensitive to BFKL resummation effects is the cross-section of dijet events where there is a gap devoid of any energy between the two jets. The production cross-section was measured by the DØ Collaboration and was found in good agreement with BFKL LL calculations [54]. BFKL NLL calculations at Tevatron and LHC are in progress [54].

6.2. Saturation physics at HERA and LHC

In this section, we will discuss some preliminary approaches related to saturation physics at HERA and briefly the implications at LHC. A sketch of the proton structure in (x, Q^2) is given in Fig. 31. The LHC will allow to probe scales in the proton which were never reached at present, by accessing values of x down to 5.10^{-7} and Q^2 up to 10^8 GeV^2. For a comparison, the Tevatron only reaches $Q^2 \sim 2.10^5$ GeV^2. When x decreases, the number of gluons increases. At some point, the number is so large that they start overlapping each other, and one cannot longer neglect the interactions between the different gluons. This is the domain of saturation. The domain of full saturation where the standard equations will not hold is yet to be discovered experimentally and this is one of the challenges for LHC. One of the already significant implications of the saturation models is that the proton structure function does not depend independently on x and Q^2 but on scaling variables which are combinations of x and Q^2 [55, 56]. The type of the predicted scaling depends on the considered equations: fixed coupling constant,

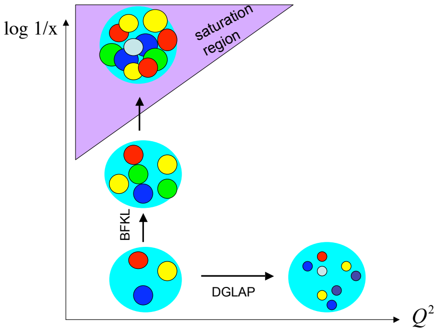

Fig. 31. QCD at hadronic colliders.

running coupling constant, Pomeron loops… It is also worth noticing that saturation models such as the one described in Ref. [57] lead to a common description of diffractive and non-diffractive data and we will come back on these models when we discuss the diffractive results.

Geometric scaling [58] is a remarkable property verified by data on high energy deep inelastic scattering (DIS). One can represent with reasonable accuracy the cross-section $\sigma^{\gamma^* p}$ by the formula $\sigma^{\gamma^* p}(Y,Q) = \sigma^{\gamma^*}(\tau)$, where Y the total rapidity in the γ^*-proton system and $\tau = \log Q^2 - \log Q_s(Y) = \log Q^2 - \lambda Y$ is the scaling variable.

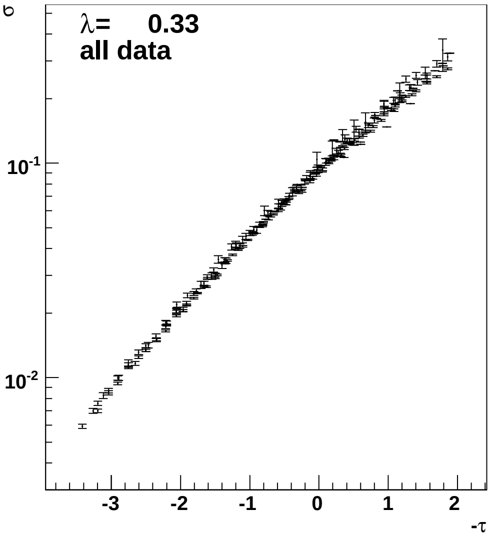

Fig. 32. Scaling curve for “Fixed Coupling” for the proton structure function F_2 measured in fixed target experiments and at HERA. A $Q^2 > 3$ and $x < 10^{-2}$ cut was applied to the data.

A way to introduce theoretically saturation in the BFKL equation was developed originally in the Balitsky–Kovchegov equation [59] (BK). When α_S is constant, it is possible to show that the solution of the BK equation at high energies does not depend independently on rapidity $Y = \log 1/x$ and $L = \log Q^2$ but on a combination of both, $\tau = L - \lambda Y$. This is called "fixed coupling" (FC). When α_S is running ($\alpha_S \sim 1/\log Q^2$), an approximate solution of the BK equation is found with a scaling in $(L - \lambda\sqrt{Y})$ called running coupling. Other forms of scalings are also possible. The experimental aspects of scaling were studied in Ref. [55], and scaling was found for proton structure function F_2, the diffractive structure function $F_2^{\rm D}$, the vector meson and DVCS production cross-sections. The results were studied quantitatively using the "quality factor" approach [56].

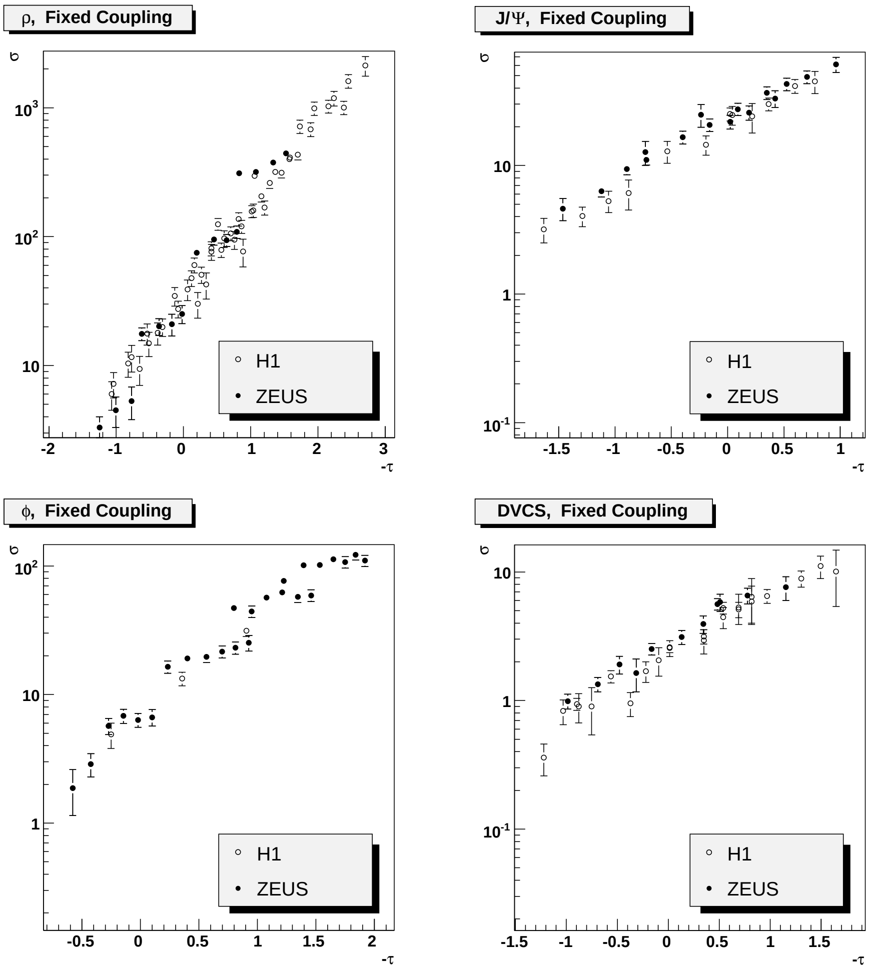

Fig. 33. Scaling curves obtained for "Fixed Coupling", for vector meson data.

As an example, we give the results of the fixed coupling scaling for the proton structure function data in Fig. 32 and for vector mesons and DVCS in Fig. 33. We will also discuss the description of diffractive inclusive data using the saturation formalism in a next section.

It is worth studying the impact of saturation effects at LHC. While most of the measurements will be done at higher Q^2 (Higgs boson, searches for new phenomena) and will not be influenced by saturation effects, dedicated measurements such as Mueller–Navelet jets might be a way to assess saturation effects [50]. On the other hand, it is worth noticing that the saturation scale at HERA or at the LHC is quite low. It was estimated for instance using inclusive F_2 measurements that the saturation scale is close to 1 GeV^2 at HERA, and is expected to be around 1–2 GeV^2 at the LHC. The fact that this scale is close to the non-perturbative region makes it difficult to observe direct consequences of saturation at LHC, and only indirect measurements such as scaling properties can be an indication of the presence of saturation at a lower scale. On the contrary, the proton-lead interactions at LHC might be a better way of observing saturation effects. The saturation scale is expected to be higher for such events (about 4–5 GeV^2) and thus entering the perturbative region. This domain is certainly worth of further studies at the LHC.

7. Conclusion on the proton structure

We have reviewed some important measurements at LHC, which are motivated to improve the knowledge of quark and gluon distributions in the proton. They have a reduced sensitivity to new physics effects, because the impact of the PDF uncertainties is that a small deviation from the Standard Model predictions could be absorbed into the PDFs. Improvements of parton distributions are expected at three different levels: reduction of the uncertainties on the parameters used in global QCD fits, reduction of the dependence on input functional form at $Q_0^2 \sim m_p^2$, and reduction of the theoretical uncertainties on evolution equations.

In order to reduce the PDF uncertainties, global QCD fits could benefit from additional measurement sensitive to parton distribution at unexplored (x, Q^2) values. Differential cross-sections using jets, photons or heavy gauge bosons *versus* the system invariant mass, transverse momentum or rapidity have a strong potential to constrain PDFs. Statistics is expected to be large at LHC so these measurements will be limited by experimental systematics that must be reduced. Some subjects are still not covered at LHC. Heavy flavour quark distributions still suffer from large statistical and systematic uncertainties, but they could be constrained by $W/Z + c$ or $W/Z + b$ cross-section measurements. These processes will be one of the main backgrounds to Higgs boson or new physics searches, their understanding is thus crucial for discoveries. Other measurements are aimed to constrain the high-x region while being safe of new physics. Low mass dijet or Drell–Yan cross-sections at high rapidity can constrain the high-x gluon or sea quark distributions, *i.e.* where the uncertainties are large.

Finally, when quoting a PDF-induced uncertainty, one needs to ascertain whether these underlying hypotheses affect the result or can be ignored. We have shown that the input functional form at $Q_0^2 \sim m_p^2$ or the choices of evolution equations can lead to large differences between predictions on observables, and thus must be more constrained. These assumptions can be tested with asymmetry measurements or ratios of cross-sections, especially built to cancel most of PDF uncertainties and thus to probe a reduced set of parton distributions. As a consequence, these observables have a better sensitivity to beyond Standard Model phenomena.

The discovery of the electroweak symmetry breaking mechanism and the observation of new particles are the main goal of the LHC. Direct searches and precision measurement both require a good control of the background and the signal itself because PDF-induced uncertainties can be larger than the size of new physics effects. Two methods have been discussed in this chapter: the reduction of the uncertainties on gluon and quark distributions via interesting measurements, or the measurement of observables less sensitive to PDF uncertainties. Both solutions improve the discovery potential of LHC.

We will now move to another important component of the proton structure which we did not mention until now and which is related to diffractive events.

8. What is diffraction: the example of HERA

In the following sections, we first describe diffraction at HERA before showing the results from Tevatron and discussing the possible measurements at LHC. As detailed in the previous sections, the advanced metrology of PDFs at LHC is a very important topic, not only in order to understand better the structure of the proton, but also to determine more precisely the background to searches for the Higgs boson or supersymmetric particles. However, as mentioned above in the context of saturation, diffraction is also an important class of processes to scrutenize and understand the structure of the proton. In fact, an important fraction of the total cross-section at HERA or LHC energies is driven by diffractive reactions, which then deserve specific studies. Let us start by giving a basic description of a diffractive event in HERA experiments. A typical standard DIS event is shown in the upper plot of Fig. 34 is $ep \to eX$ where electron and jets are produced in the final state. We notice that the electron is scattered in the H1 backward

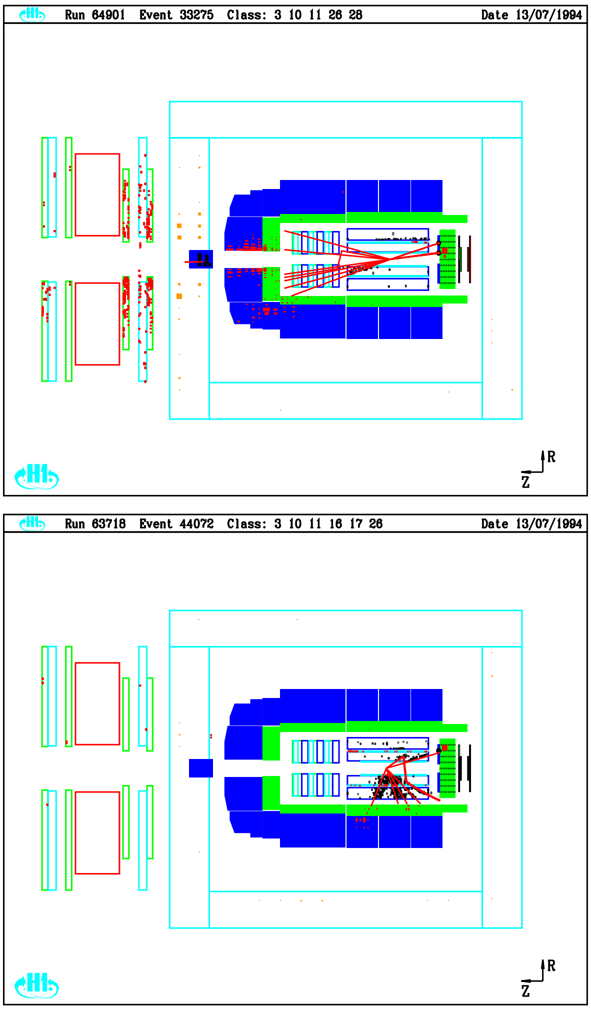

Fig. 34. Standard and diffractive events in the H1 experiment. For the diffractive event, the electron is visible in the backward detector, there is still some hadronic activity (jets) in the LAr calorimeter, but no energy above noise level is deposited in the forward part of the LAr calorimeter or in the forward muon detectors. In other words, there is no colour exchange between the proton and the produced jets.

detector[3] whereas some hadronic activity is present in the forward region of the detector (in the LAr calorimeter and in the forward muon detectors). The proton is thus completely destroyed and the interaction leads to jets and proton remnants directly observable in the detector. The fact that

---

[3] At HERA, the backward (resp. forward) directions are defined as the direction of the outgoing electron (resp. proton).

much energy is observed in the forward region is due to colour exchanges between the scattered jet and the proton remnants. In contrast, for about 10% of the events, the situation is completely different. Such events appear like the one shown in the bottom plot of Fig. 34. The electron is still present in the backward detector, there is still some hadronic activity (jets) in the LAr calorimeter, but no energy above noise level is deposited in the forward part of the LAr calorimeter or in the forward muon detectors. In other words, there is no colour exchange between the proton and the produced jets. As an example, this can be explained if the proton stays intact after the interaction. These events amount to about 10% of the total deep inelastic event production at HERA in the acceptance of the measurement — they are called diffractive — and about 30 % of the total cross-section at LHC. Thus, they cannot be ignored with the assumption that the dynamics of those reactions follow exactly the standard QCD equations that govern the PDF behaviour. The possible explanations of the underlying dynamics of such processes is described in the following. We also show why their specific analysis is an essential aspect of understanding the proton structure at high gluon densities.

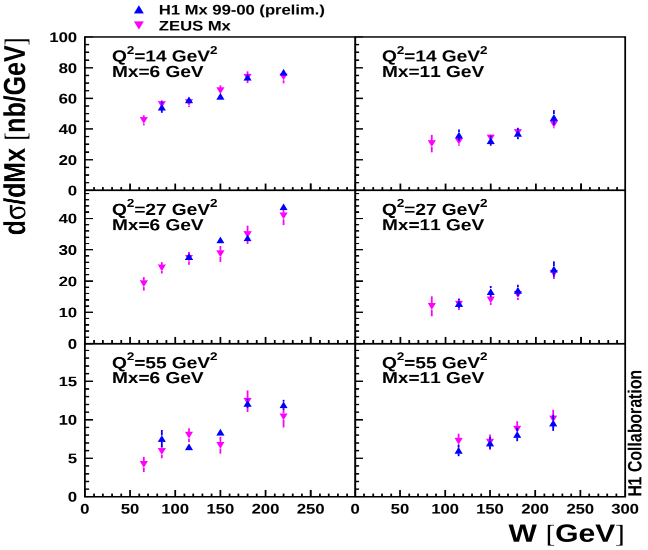

Fig. 35. The cross-section of the diffractive process $\gamma^* p \to p' X$ measured by the H1 and ZEUS collaborations, differential in the mass of the diffractively produced hadronic system X (M_X), is presented as a function of the centre-of-mass energy of the $\gamma^* p$ system W. Measurements at different values of the virtuality Q^2 of the exchanged photon are displayed.

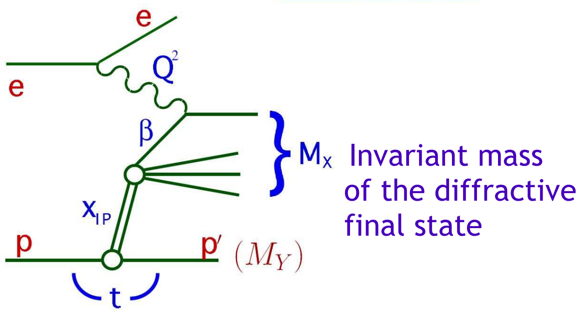

Fig. 36. Scheme of a diffractive event at HERA.

One of the first experimental results to be considered is the diffractive cross-section as a function of the energy dependence of the $\gamma^* p$ system, which has been measured at HERA by H1 [60–62] and ZEUS [63–65] experiments over a wide kinematic range (see Fig. 35). In order to describe the diffractive processes described in Fig. 36 where there is no colour exchange between the proton in the final state and the scattered jet, we have to introduce new variables in addition to the ones used to describe the inclusive DIS such as Q^2, W, x and y. Namely, we define $x_{I\!P}$, which is the momentum fraction of the proton carried by the colourless object (called the Pomeron), and β, the momentum fraction of the Pomeron carried by the interacting parton inside the Pomeron, if we assume the Pomeron to be made of quarks and gluons:

$$x_{I\!P} = \xi = \frac{Q^2 + M_X^2}{Q^2 + W^2} \,, \tag{5}$$

$$\beta = \frac{Q^2}{Q^2 + M_X^2} = \frac{x}{x_{I\!P}} \,. \tag{6}$$

In order to make quantitative predictions, we need to distinguish two kinds of factorisation at HERA. The first factorisation is the QCD hard scattering collinear factorisation at fixed $x_{I\!P}$ and t (see left plot of Fig. 37) [66], namely

$$d\sigma(ep \to eXY) = f_{\mathrm{D}}\left(x, Q^2, x_{I\!P}, t\right) \times d\hat{\sigma}\left(x, Q^2\right) \,, \tag{7}$$

where we can factorise the flux f_{D} from the cross-section $\hat{\sigma}$. This factorisation was proven recently, and separates the γq coupling to the interaction with the colourless object. The Regge factorisation at the proton vertex allows to factorise the $(x_{I\!P}, t)$ and (β, Q^2) dependence, or in other words the hard interaction from the Pomeron coupling to the proton (see right plot of Fig. 37).

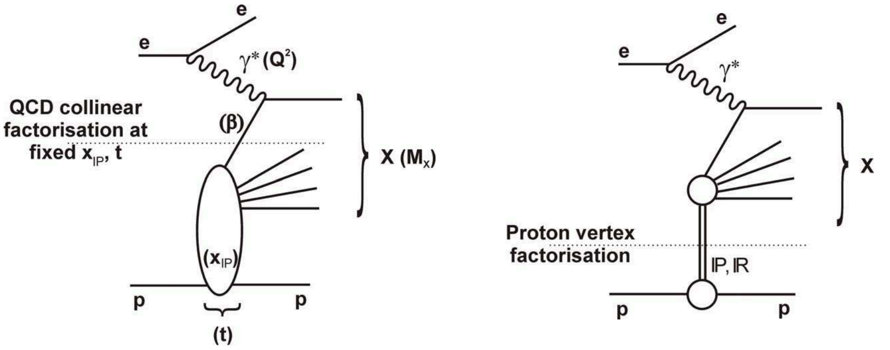

Fig. 37. Diffractive factorisation.

The measurement of the diffractive structure function is shown in Figs 35 and 39 (next section):

$$\frac{d^3\sigma^{\mathrm{D}}}{dx_{I\!P}dQ^2d\beta} = \frac{2\pi\alpha_{\mathrm{em}}^2}{\beta Q^4}\left(1-y+\frac{y^2}{2}\right)\sigma_r^{\mathrm{D}}(x_{I\!P},Q^2,\beta)\,. \tag{8}$$

We notice that the measurement has been performed with high precision over a wide kinematical domain: $0.01 < \beta < 0.9$, $3.5 < Q^2 < 1600\,\mathrm{GeV}^2$, $10^{-4} < x_{I\!P} < 5.10^{-2}$ for H1 as an example. We also observe that the diffractive cross-section shows a hard dependence in the centre-of-mass energy of the γ^*p system W. Namely, we get a behaviour of the form $\sim W^{0.6}$ for the diffractive cross-section, compatible with the dependence expected for a hard process. This first observation allows further studies of the diffractive process in the context of perturbative QCD, as diffractive PDFs or dipole models, which are described in the following.

9. Different models of diffraction

In this section, we describe the diffractive interactions and their link with the proton structure. We should not forget that diffractive processes represent a sizable fraction of the total cross-section at HERA, Tevatron and LHC energies. Diffraction is also a natural process to obtain a better understanding of the fundamental issues of saturation. We present below four different interpretations of diffractive events. The challenge for all models is not only to describe diffractive data from HERA but also diffraction at Tevatron and then LHC. In this review, we introduce the different models in the context of HERA and later on, at hadronic colliders. A detailed quantitative comparison of the different models can be found in Ref. [67].

9.1. Diffraction via a Pomeron made of quarks and gluons

The requirement of a separation of the diffracted final state from the target leads, at high energy, to the presence of a large rapidity gap between the two systems. In the parton model, there is no mechanism for producing large rapidity gaps other than by fluctuations in the hadronisation process which are short range in rapidity. Therefore, diffractive dissociation as such has to be introduced by hand. The idea of Ingelman and Schlein was to postulate that the Pomeron has a partonic structure which may be probed in hard interactions in much the same way as the partonic structure of hadrons [67–69]. They suggested that the partonic structure of the Pomeron would manifest itself in the production of high transverse momentum jets associated with single diffractive dissociation, for example in *pp* scattering. The trigger for such a reaction would consist of a quasi elastically scattered proton and the presence of high $p_{\rm T}$ jets in final state of the dissociated hadron. The jets would be accompanied by remnants of the Pomeron and of the diffracted hadron.

As we mentioned already, according to Regge theory, we can factorise the $(x_{I\!P}, t)$ dependence from the (β, Q^2) one for each trajectory (Pomeron and Reggeon). The first diffractive structure function measurement from the H1 Collaboration [70] showed that the assumption of plain factorisation between the $x_{I\!P}$ and $(\beta,\ Q^2)$ dependences was not true. The natural solution as observed in soft physics was that two different trajectories, namely Pomeron and secondary Reggeon, were needed to describe the measurement, which lead to a good description of the data. The diffractive structure function then reads:

$$F_2^{\rm D} \sim f_p(x_{I\!P})\left(F_2^{\rm D}\right)_{\rm Pom}\left(\beta, Q^2\right) + f_r(x_{I\!P})\left(F_2^{\rm D}\right)_{\rm Reg}\left(\beta, Q^2\right)\,, \tag{9}$$

where f_p and f_r are the Pomeron and Reggeon fluxes, and $(F_2^{\rm D})_{\rm Pom}$ and $(F_2^{\rm D})_{\rm Reg}$ the Pomeron and Reggeon structure functions. The flux parametrisation is predicted by Regge theory:

$$f(x_{I\!P}, t) = \frac{e^{B_P t}}{x_{I\!P}^{2\alpha_P(t)-1}}\,, \tag{10}$$

with the following Pomeron trajectory

$$\alpha_P(t) = \alpha_P(0) + \alpha'_P t\,. \tag{11}$$

The next step is to perform Dokshitzer–Gribov–Lipatov–Altarelli–Parisi (DGLAP) [4] fits to the Pomeron structure function based on the Ingelman and Schlein model of the Pomeron. If we assume that the Pomeron is made of quarks and gluons, it is natural to check whether the DGLAP evolution equations are able to describe the Q^2 evolution of these parton densities. As necessary for DGLAP fits, a form for the input distributions is assumed at a given Q_0^2 and is evolved using the DGLAP evolution equations to a different Q^2, and fitted to the diffractive structure function data at this Q^2 value.

The DGLAP QCD fit allows to get the parton distributions in the Pomeron as a direct output of the fit, and is displayed in Fig. 38 as a shaded (blue) area as a function of β. We first note that the gluon density is much higher than the quark one, showing that the Pomeron is gluon dominated. We also note that the gluon density at high β is poorly constrained which is shown by the larger shaded area. Another fit was also performed by the H1 Collaboration and is displayed as a black line in Fig. 38. This shows further that the gluon is very poorly constrained at high β and some other data sets such as jet cross-section measurements are needed to constrain it further. The H1 Collaboration showed that the jet data have the tendency to favour the lowest values of the gluon density (black line in Fig. 38).

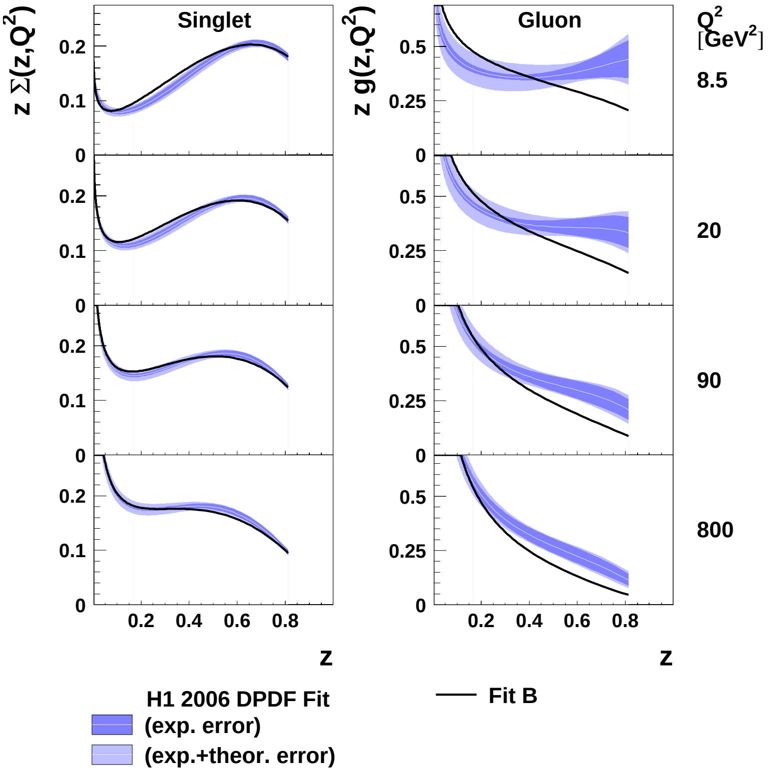

Fig. 38. Extraction of the parton densities in the Pomeron using a DGLAP NLO fit (H1 Collaboration).

As we show in the following, these quark and gluon densities in the Pomeron are essential ingredients to predict diffractive cross-sections at Tevatron and LHC that we describe in the next subsections.

9.2. Dipole models

Another model to describe inclusive diffraction at HERA is based on dipole models. It is useful to look at *ep* scattering in a frame where the virtual photon moves very fast (for instance in the proton rest frame, where the γ^* has a momentum of up to about 50 TeV at HERA). The virtual photon can fluctuate into a quark–antiquark pair, forming a small colour dipole. Because of its large Lorentz boost, this virtual pair has a lifetime much longer than a typical strong interaction time. Since the interaction between the pair and the proton is mediated by the strong interaction, diffractive events are possible. An advantage of studying diffraction in *ep* collisions is that, for sufficiently large photon virtuality Q^2, the typical transverse dimensions of the dipole are small compared to the size of a hadron. The interaction between the quark and the antiquark, as well as the interaction of the pair with the proton, can be treated perturbatively. With decreasing Q^2 the colour dipole becomes larger, and at very low Q^2 these interactions become so strong that a description in terms of quarks and gluons is no longer justified, and the diffractive reactions become very similar to those in hadron–hadron scattering.

The original dipole model assumes the simplest perturbative description of the Pomeron by a two-gluon ladder [71, 72]. A parametrisation of the diffractive structure function in terms of three main contributions is proposed. The first term describes the diffractive production of a $q\bar{q}$ pair from a transversely polarised photon, the second one the production of a diffractive $q\bar{q}g$ system, and the third one the production of a $q\bar{q}$ component from a longitudinally polarised photon. The dipole model leads to a good description of data. In Fig. 39, we give the comparison between the H1 and ZEUS data and the dipole model which leads to a good description of the F_2^{D} measurement on the full range. Other extensions of the dipole model containing for instance higher order contributions such as $q\bar{q}gg$, $q\bar{q}ggg$, *etc.*, exist and lead also to a good description of data [71]. Unfortunately, by definition, it is difficult to transpose the dipole model to hadronic colliders.

9.3. Description of F_2^{D} using saturation models

We have already introduced in a previous section the concept of saturation. Below, we discuss the practical implementation of this concept by Golec-Biernat and Wüsthoff [57], which has been formulated in the colour dipole picture. In this formalism, both the inclusive and diffractive cross-sections may be calculated. The diffractive structure function $F_2^{\mathrm{D}(3)}$ is the sum of three contributions [57]:

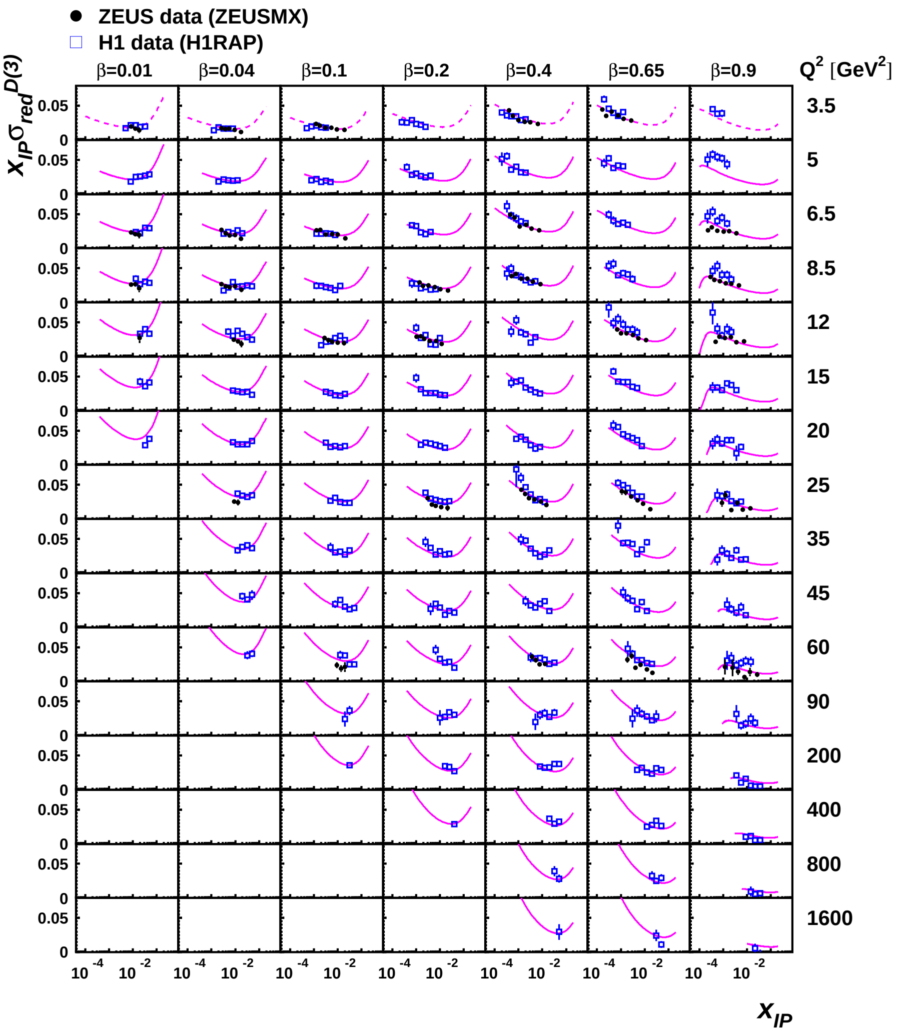

Fig. 39. Comparison of H1 and ZEUS data sets with the prediction of the dipole model. Only the statistical part of the uncertainty is shown for the data points on this plot. A dashed line is drawn for the prediction of the fit on points not included in the analysis.

$$F_2^{\mathrm{D}(3)}(Q^2, x_{I\!P}, \beta) = F_{\mathrm{T}}^{q\bar{q}} + F_{\mathrm{L}}^{q\bar{q}} + F_{\mathrm{T}}^{q\bar{q}g} \,. \tag{12}$$

The dipole cross-section has the following form:

$$\hat{\sigma}(x,r) = \sigma_0 \left\{1 - \exp\left(-r^2 \frac{Q^2_{\mathrm{sat}}(x)}{4}\right)\right\} , \qquad Q^2_{\mathrm{sat}}(x) = \left(\frac{x_0}{x}\right)^{\lambda} , \tag{13}$$

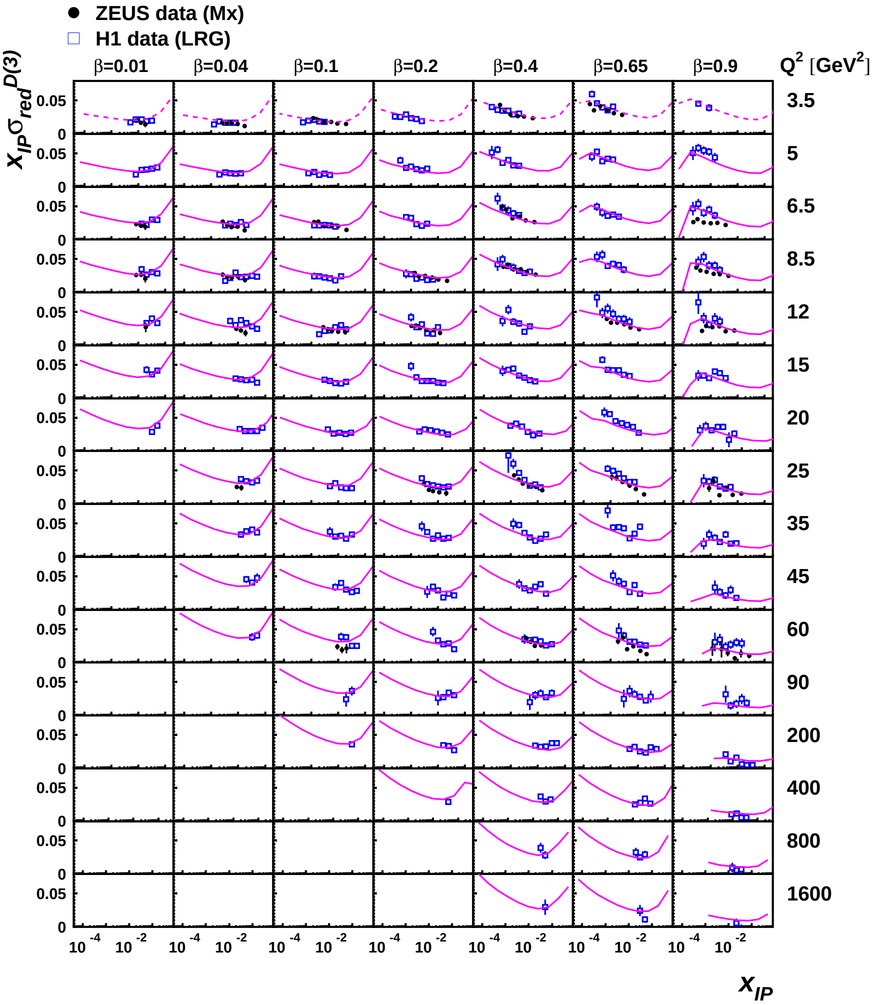

Fig. 40. Comparison of H1 and ZEUS data sets with the prediction of the saturation model. Only the statistical part of the uncertainty is shown for the data points on this plot. A dashed line is drawn for the prediction of the fit on points not included in the analysis.

which introduces three parameters: the maximal possible value of the dipole cross-section σ_0 and two parameters characterizing the saturation scale $Q^2_{\text{sat}}(x)$ that is λ and x_0. In Fig. 40, we give the comparison between the H1 and ZEUS F_2^{D} data and the saturation model which leads to a good description of data. It is worth noticing that both the inclusive F_2 and the diffractive F_2^{D} measurements can be described within the same framework of saturation models. Since these original ideas, many theoretical and pheneomenological developments occured which lead to a good description of data at HERA [57]. It is worth noticing that this is one of the only models which aim at a global description of HERA, RHIC and also Tevatron and LHC in a given phase space where the gluons dominate. This model provides an essential tool to examine the prior effects of saturation that takes place at the microscopic level of the dipole amplitude. For this sake, diffractive processes show the best sensitivity and this is why they are so precious in analyzing the structure of the proton.

9.4. Soft colour interaction

This alternative model assumes that diffraction is not due to a colourless exchange at the hard vertex (called Pomeron) but rather to string rearrangement in the final state during hadronisation [73]. In this kind of model, there is a probability (to be determined by the experiment) that there is no string connection, and so no colour exchange, between the partons in the proton and the scattered quark produced during the hard interaction. We discuss further this model when we discuss the measurements at the Tevatron.

10. Limits of diffractive hard-scattering factorisation: hadron–hadron collisions

A natural question to ask is whether one can use the diffractive PDFs extracted at HERA to describe hard diffractive processes in hadron–hadron collisions, and especially to predict the production of jets, heavy quarks or weak gauge bosons at the Tevatron.

From a theoretical point of view, diffractive hard-scattering factorisation does not apply to hadron–hadron collisions because of additional interactions between the particles in initial and final states, but it will be interesting to study experimentally how factorization is broken. The breakdown of factorisation occurs because of interactions between spectator partons of the colliding hadrons. The contribution of these interactions to the cross-section does not decrease with the hard scale. Since they are not associated with the hard scattering subprocess, factorisation between the parton-level cross-section and the parton densities of one of the colliding hadrons is no longer true. These additional interactions are generally soft, and we have at present to rely on phenomenological models to quantify their effects [74]. The yield of diffractive events in hadron–hadron collisions is expected to be lower because of these soft interactions between spectator partons (often referred to as reinteractions or multiple scatterings). They can produce additional final state particles which fill the would-be rapidity gap (hence the notion of gap survival probability). When such additional particles are produced, a very fast proton can no longer appear in the final state because of energy conservation. Diffractive factorisation breaking is thus intimately related to multiple scattering in hadron–hadron collisions. Understanding and describing this phenomenon is a challenge in the high-energy regime that will be reached at the LHC [74]. It is also worth noticing that the time scale when factorisation breaking occurs is completely different from the hard interaction one. Factorisation breaking is due to soft exchanges occuring in the initial and final states which appear at a much longer time scale than the hard interaction. In that sense, it is expected that the survival probability will not depend strongly on the type of hard interaction and its kinematics. In other words, the survival probability should be similar if one produces jets of different energies, vector mesons, photons, *etc.*, which can be cross-checked experimentally at Tevatron and LHC.

We can also notice that the collision partners, in pp or $p\bar{p}$ reactions, are both composite systems of large transverse size, and it is not too surprising that multiple interactions between their constituents can be substantial. In contrast, the virtual photon in γ^*p collisions shows a small transverse size, which disfavours multiple interactions and enables diffractive factorisation to hold. According to our discussion, we may expect that for decreasing virtuality Q^2 the photon behaves more and more like a hadron, and diffractive factorisation may again be broken.

We now study how factorisation is broken experimentally in two steps: is factorisation observed within Tevatron data alone (or in other words, does the survival probability or the soft interactions depend on the occuring hard interaction) and is factorisation broken as expected between Tevatron and HERA?

The CDF Collaboration measured diffractive events at the Tevatron and their characteristics. Diffractive events show, as expected, less QCD radiation: as an example, dijet events are more back-to-back or the difference in azimuthal angles between both jets is more peaked towards π. We first check whether factorisation holds within CDF data alone or in other words, if the β and Q^2 dependence can be factorised out from the ξ one. In Fig. 41, we notice that the percentage of diffractive events shows the same x-dependence for different ξ bins within systematic and statistical uncertainties, which supports the fact that CDF data are consistent with factorisation [75]. The x dependence for different Q^2 bins also leads to the same conclusion. These results show that the additional soft interactions or the multiple interactions are compatible with a weak dependence on the hard scattering which is somewhat natural since they occur at a much longer time scale.

The first step of the study of factorisation breaking between Tevatron and HERA is just confirmed by counting the percentage of diffractive events observed at both accelerators: 10% at HERA and about 1% of single diffractive events at the Tevatron. The second step is to determine how factorisa-

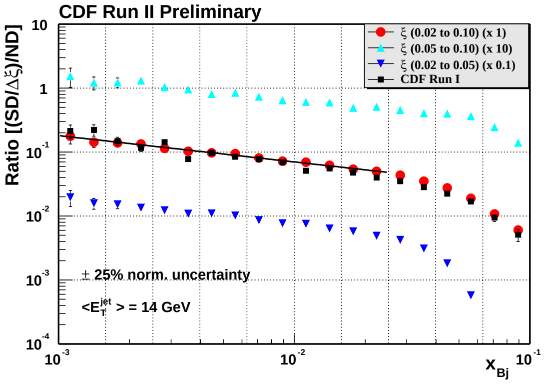

Fig. 41. Test of factorisation within CDF data alone.

tion is broken between Tevatron and HERA data. It is possible to measure indirectly the diffractive structure function at the Tevatron. The CDF Collaboration measured the ratio of dijet events in single diffractive and non-diffractive events directly proportional to the ratio of the diffractive to the "standard" proton structure functions F_2:

$$R(x) = \frac{\mathrm{Rate}_{jj}^{\mathrm{SD}}(x)}{\mathrm{Rate}_{jj}^{\mathrm{ND}}(x)} \sim \frac{F_{jj}^{\mathrm{SD}}(x)}{F_{jj}^{\mathrm{ND}}(x)} \,. \tag{14}$$

The "standard" proton structure function in this kinematic region is known from the usual PDFs using for instance the CTEQ or MRST parametrisations. The comparison between the CDF measurement (black points, with systematics errors as shaded area) and the expectation from the H1 QCD fits in full line is shown in Fig. 42 [76]. We notice a difference by a factor 8 to 10 between the data and the predictions from the QCD fit assuming factorisation or a survival probability equal to 1. The breaking of factorisation is thus confirmed and the value of the survival probability is of the order of 0.1. Fig. 42 also shows that the difference is compatible with a constant within systematic and statistical uncertainties on a large part of the kinematical plane in β, which means that the survival probability is compatible with a constant independent of β. It will be interesting to make these studies again in a wider kinematical domain both at the Tevatron and at the LHC. The understanding of the survival probability and its dependence on the kinematic variables is important to make precise predictions on inclusive diffraction at the LHC.

The other interesting test of factorisation which can be also performed at the Tevatron is to check if factorisation holds between single diffraction and double Pomeron exchange. The results from the CDF Collaboration are

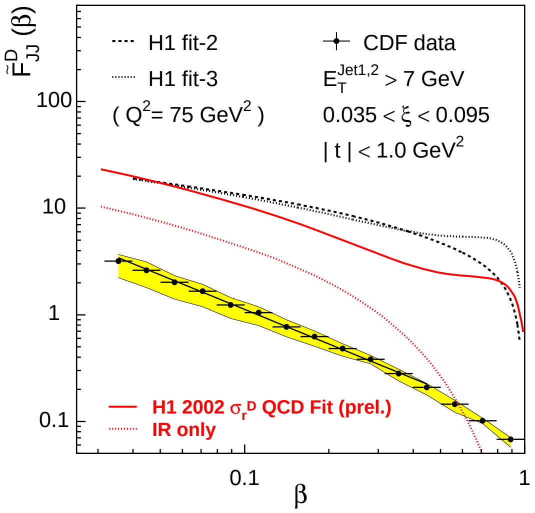

Fig. 42. Comparison between the CDF measurement of diffractive structure function (black points) with the expectation of the H1 QCD fits (red full line).

shown in Fig. 43 [76]. The left plot shows the definition of both ratios while the right figure shows the comparison between the ratio of double Pomeron exchange to single diffraction and the QCD predictions using HERA data in full line. Factorisation holds for the ratio of double Pomeron exchange to single diffraction. In other words, the price to pay for one gap is the same as the price to pay for two gaps. The survival probability needs to be applied only once to require the existence of a diffractive event, but should not be applied again for double Pomeron exchange.

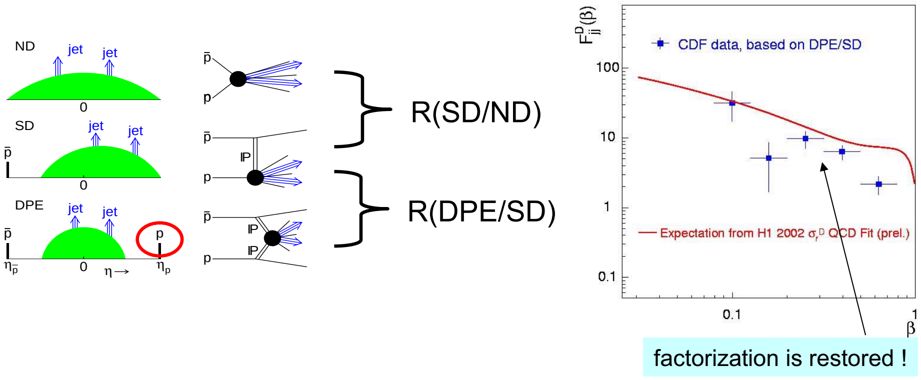

Fig. 43. Restoration of factorisation for the ratio of double Pomeron exchange to single diffractive events (CDF Collaboration).

11. From soft to hard physics: vector meson production at HERA

11.1. Exclusive vector mesons at HERA

For all processes we have discussed till now, using the point of view of PDFs, at HERA, Tevatron or LHC, the very basic assumption is, of course, that it makes sense to use PDFs to describe those reactions. In other words, we have always assumed that those processes are driven by partons, which is what we call a hard process. Most of the time, the assumption is implicit when there is a hard scale in the problem: for example, the W or Z mass in the case of events at the LHC. However, in general, we do not know the frontier between a hard process (parton driven) and a soft reaction, where the description in terms of partons is yet unknown. In fact, together with the high parton density physics of the small-x regime of ep scattering at HERA came the realisation that the hard physics studied till now is the result of an interplay of hard and soft phenomena. In the case of deep inelastic scattering the unknown soft physics is hidden in the initial parton distributions which are parameterised at a relatively small scale $Q_0^2 \sim 1\,\mathrm{GeV}^2$. The lack of a dynamical picture of the proton structure leads to a large uncertainty about the region of phase space which has not been probed as yet. This uncertainty propagates itself in QCD predictions for high energy hard scattering at future colliders. The ability to separate clearly the regimes dominated by soft or by hard processes is essential for exploring QCD both at a quantitative and qualitative level. A typical example of a process dominated by soft phenomena is the interaction of two large size partonic configurations such as two hadrons. A process which would lend itself to a fully perturbative calculation, and therefore hard, is the scattering of two small size heavy onium-states each consisting of a pair of heavy $q\bar{q}$ pair. In deep inelastic scattering the partonic fluctuations of the virtual photon can lead to configurations of different sizes. The size of the configuration will depend on the relative transverse momentum k_{T} of the $q\bar{q}$ pair. Small size configurations (large $k_{\mathrm{T}} \sim Q/2$) are favoured by phase space considerations (the phase space volume available is proportional to k_{T}^2/Q^2). In the quark parton model (QPM), in order to preserve scaling, it was necessary to suppress their presence by making them sterile. In QCD there is a simple explanation for this suppression — the effective colour charge of a small size $q\bar{q}$ pair is small due to the screening of one parton by the other and therefore the interaction cross-section will be small. This phenomenon is known under the name of colour transparency.

At this point comes exclusive vector meson production, for which we can differentiate soft and hard components of the interaction processes. In the following, we show that these reactions allows to study the transition between hard and soft physics. At HERA, it was found that the cross-sections for exclusive vector meson production rise strongly with energy when compared to fixed target experiments, if a hard scale is present in the process. In the case of J/ψ production, the strong rise of the cross-section is indeed measured directly. The theoretical calculations indicate that the cross-sections depend on the square of the gluon density in the proton. If higher order calculations become available, the measurement of the energy dependence of the vector meson cross-section may be one of the ideal methods to measure the gluon density in the proton. In pQCD models, the scattering ($\gamma p \to Vp$) is viewed in the proton rest frame as a sequence of events very well separated in time. The process is depicted in Fig. 44. A first approximation of the cross-section can be written as

$$\left.\frac{d\sigma}{dt}\right|_{t=0} (\gamma^* N \to VN) = \frac{4\pi^3 \Gamma_V m_V \alpha_{\mathrm{s}}^2(Q) \eta_V^2 \left(xg(x,Q^2)\right)^2}{3\alpha_{\mathrm{em}} Q^6} , \tag{15}$$

where the dependence on the meson structure is in the parameter

$$\eta_V = \frac{1}{2} \int \frac{dz}{z(1-z)} \phi^V(z) \Big/ \int dz \phi^V(z) \tag{16}$$

and $\phi^V(z)$ is the light-cone wave function. Exclusive electroproduction of light vector mesons is a particularly good process to study the transition from the soft to the hard regime of strong interactions, the former being well described within the Regge phenomenology while the latter by perturbative QCD (pQCD). Among the most striking expectations in this transition is the change of the logarithmic derivative δ of the cross-section σ with respect to the $\gamma^* p$ center-of-mass energy W, from a value of about 0.2 in the soft regime to 0.8 in the hard one (represented by a two-gluon exchange diagram

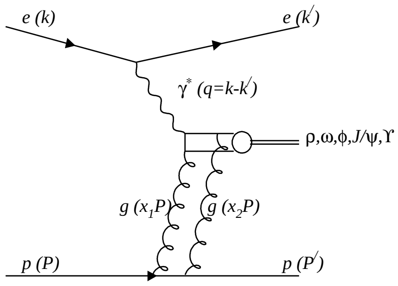

Fig. 44. Exclusive vector meson production in QCD based models. The photon is viewed as fluctuating into a quark–antiquark pair, which couples to the proton via the exchange of two gluons (with momentum fractions x_1, x_2). The vector meson is formed after the scattering has occurred.

in Fig. 44), and the decrease of the exponential slope b of the differential cross-section with respect to the squared four momentum transfer t, from a value of about $10\,\mathrm{GeV}^{-2}$ to an asymptotic value of about 5 GeV^{-2} when the virtuality Q^2 of the photon increases [77–79].

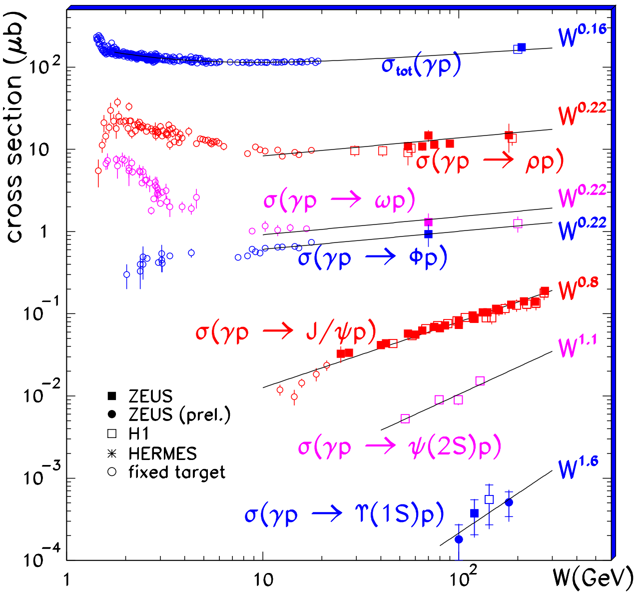

Fig. 45. W dependence of the exclusive vector meson cross-section in photoproduction, $\sigma(\gamma p \rightarrow Vp)$. The total photoproduction cross-section is also shown. The lines are the fit result of the form W^δ to the high energy part of the data.

The soft to hard transition can be seen by studying the W dependence of the cross-section for exclusive vector meson photoproduction, from the lightest one, ρ^0, to the heavier ones, up to the Υ. The scale in this case is the mass of the vector meson, as in photoproduction $Q^2 = 0$. Fig. 45 shows $\sigma(\gamma p \rightarrow Vp)$ as a function of W for light and heavy vector mesons. For comparison, the total photoproduction cross-section, $\sigma_{\mathrm{tot}}(\gamma p)$, is also shown. The data at high W can be parameterised as W^δ, and the value of δ is displayed in the figure for each reaction. One sees clearly the transition from a shallow W dependence for low scales (soft) to a steeper one as the scale increases (hard).

One can also check this transition by varying Q^2 for a given vector meson. The cross-section $\sigma(\gamma^* p \rightarrow \rho^0 p)$ is presented in Fig. 46 as a function of W, for different values of Q^2. The cross-section rises with W in all Q^2 bins.

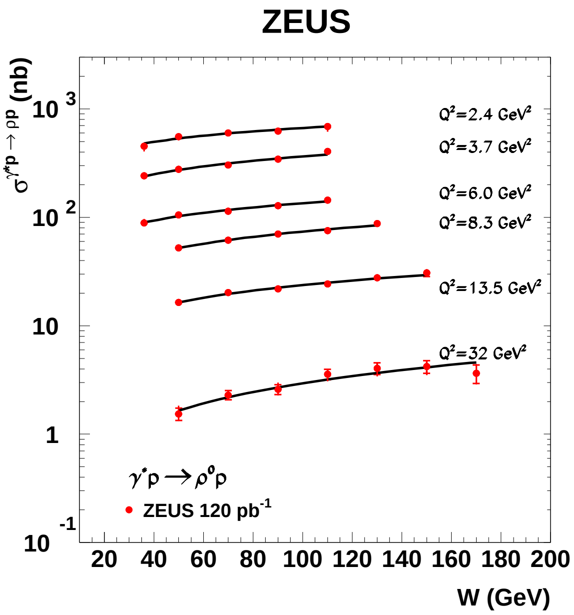

Fig. 46. W dependence of the cross-section for exclusive ρ^0 electroproduction, for different Q^2 values, as indicated in the figure. The lines are the fit results of the form W^δ to data.

The same conclusion holds for the deeply virtual Compton scattering (DVCS) (Fig. 47), in which a real photon is produced instead of a VM $ep \rightarrow ep\gamma$. In order to quantify this rise, the logarithmic derivative δ of cross-section with respect to W is obtained by fitting the data to the expression $\sigma \sim W^\delta$ in Q^2 intervals. The resulting values of δ from recent measurements

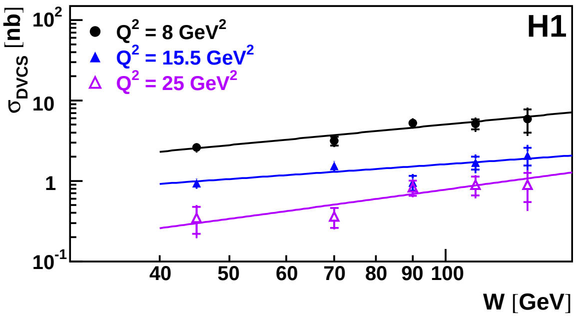

Fig. 47. The DVCS cross-section as a function of W at three values of Q^2. The solid lines represent the fit results of the form W^δ.

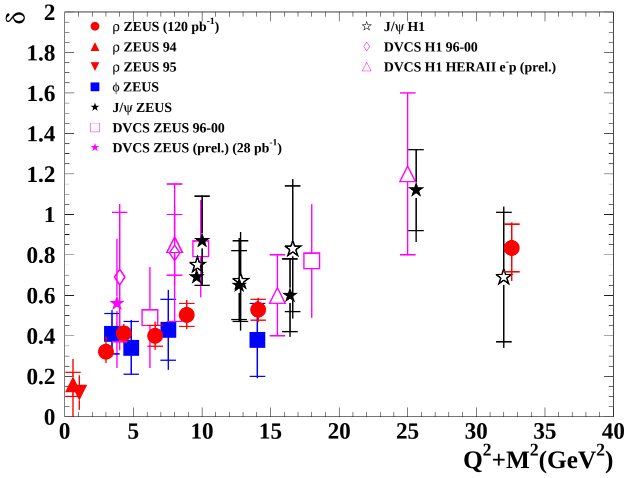

Fig. 48. A compilation of values of δ from fits of the form W^{δ} for exclusive VM electroproduction, as a function of $Q^2 + M^2$. It includes also the DVCS results.

are compiled in Fig 48. Also included in this figure are values of δ from other measurements [77] for the ρ^0 as well as those for ϕ [78], J/ψ [79] and γ [80–83]. Results are plotted as a function of $Q^2 + M^2$, where M is the mass of the vector meson. One sees a universal behaviour, showing an increase of δ as the scale becomes larger. The value of δ at low scale is the

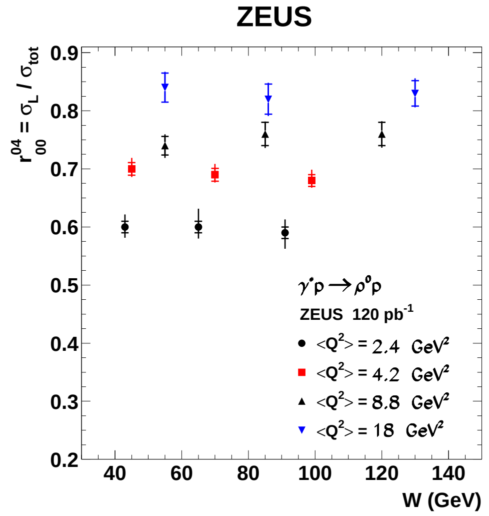

Fig. 49. The ratio $r_{00}^{04} = \sigma_{\rm L}/\sigma_{\rm tot}$ as a function of W for different values of Q^2.

one expected from the soft Pomeron intercept, while the one at large scale is in accordance with twice the logarithmic derivative of the gluon density with respect to W. A comment is in order concerning the W dependence of DVCS. It reaches the same value of δ as in the hard process of J/ψ electroproduction. Given the fact that the final state photon is real, and thus transversely polarised, the DVCS process is produced by transversely polarised virtual photons, assuming s-channel helicity conservation. The steep energy dependence thus indicates that the large configurations of the virtual transverse photon are suppressed and the reaction is dominated by small $q\bar{q}$ configurations, leading to the observed perturbative hard behavior. A similar effect is observed for ρ^0 production, as displayed in Fig. 49. The ratio $\sigma_L/\sigma_{\rm tot}$ is shown to be constant with W, which means that the W dependence for σ_L and σ_T are about the same [55].

11.2. t-dependence of the vector meson production cross-section

One of the key measurement in exclusive processes is the dependence of the cross-section in t, where $t = (p - p')^2$ is the square of the momentum transfer at the proton vertex. The differential cross-section, $d\sigma/dt$, is parameterised by an exponential function $e^{-b|t|}$ (at small t) and fitted to the data of exclusive vector meson electroproduction and also to DVCS. The resulting values of b as a function of the scale $Q^2 + M^2$ are plotted in Fig. 50. As expected, b decreases to a universal value of about 5 GeV^{-2} as the scale increases.

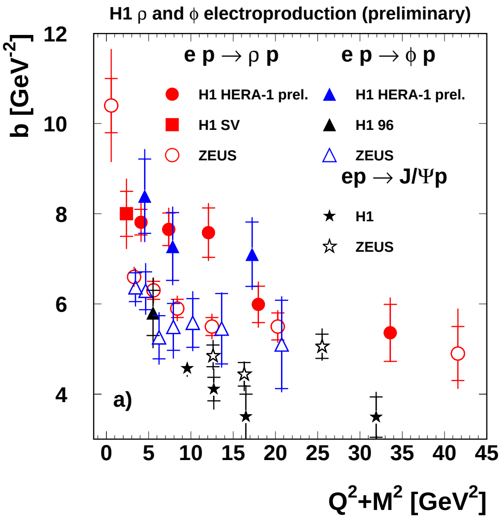

Fig. 50. A compilation of the b slope values from fits of the form $d\sigma/d|t| \propto e^{-b|t|}$ for exclusive vector–meson electroproduction, as a function of $Q^2 + M^2$.

A Fourier transform from momentum to impact parameter space shows that the t-slope b is related to the typical transverse distance between the colliding objects which data allow us to measure experimentally. At high scale, the $q\bar{q}$ dipole is almost point-like, and the t dependence of the cross-section is given by the transverse extension of the gluons (or sea quarks) in the proton for a given x range [84–87, 89, 90]. This is an important issue in modern lepton nucleon scattering that we can call proton tomography. Detailed reviews can be found in [84–88]. Applications at LHC energies of the parton transverse profiles, derived from impact parameter analysis, are of fundamental interests, but not yet at a practical level.

More generally, one can study the W dependence of $d\sigma/dt$ for fixed t values and extract the effective Pomeron trajectory $\alpha_{IP}(t)$ for all VMs. This was done in the case of ρ^0 production for two Q^2 values and the trajectory was fitted to a linear form to obtain the intercept $\alpha_{IP}(0)$ and the slope α'_{IP}. These values are presented in a compilation of the effective Pomeron intercept and slope in Fig. 51. Values are plotted as a function of $Q^2 + M^2$. We observe that the value of $\alpha_P(0)$ increases with Q^2 while the value of α'_P tends to decrease with Q^2. Results found for DVCS are consistent with with $\alpha'_P = 0$, as for the J/Ψ [80] (see Fig. 52). The resulting value of $\alpha' \approx 0$ is an evidence of no shrinkage of $d\sigma/dt$ in the process $\gamma^* p \to J/\Psi p$ or $\gamma^* p \to \gamma p$. This gives an important input for the parametrisations of Pomeron flux at the LHC, when producing J/Ψ diffractively.

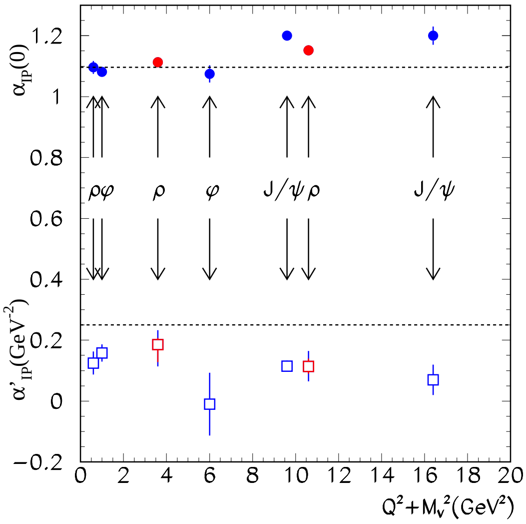

Fig. 51. Values of the intercept and slope of the effective Pomeron trajectory as a function of $Q^2 + M^2$, as obtained from measurements of exclusive VM electroproduction. The dashed lines show the results from soft elastic scattering.

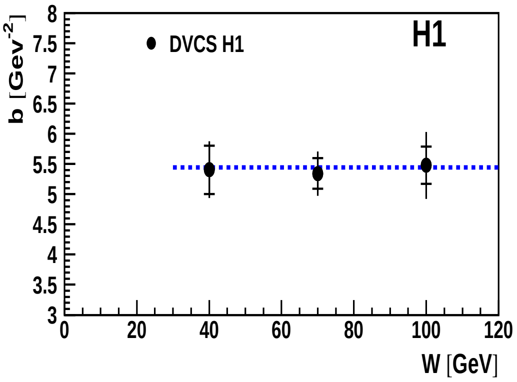

Fig. 52. The logarithmic slope of the t dependence for DVCS as a function of W.

11.3. Generalised parton distributions

Let us mention briefly at this level one of the newest possibilities of lepton–nucleon scattering experiments. For a few years, they can give access to the spatial distribution of quarks and gluons in the proton at femtometer scale. The general framework which describes these measurements is encoded in the generalised parton distributions (GPDs) [91]. In fact, the reconstruction of spatial images from scattering experiments by way of Fourier transforms of the observed scattering pattern is a technique widely used in physics, for example in X-rays scattering from crystals. Recently, it has been discovered how to extend this technique to the spatial distribution of quarks and gluons within the proton, using processes that probe the proton at a tiny resolution scale. Mapping out the GPDs is an ambitious program that requires a large amount of experimental information and future programs at JLab and CERN (COMPASS, LHC), in the continuation of HERA measurements (see [80–83, 92–95] and [96]). This domain of research follows a great expansion, both on the experimental or theoretical sides. First, as mentioned above, via spatial imaging of the nucleon. Second, GPDs will allow us to quantify how the orbital motion of quarks in the nucleon contributes to the nucleon spin, a question of crucial importance for our understanding of the mechanics underlying nucleon structure. Third, the spatial view of the nucleon enabled by the GPDs provides us with new ways to test dynamical models of the nucleon structure. This will be relevant to understand the proton structure in detail such as the spatial and energy partonic structure. However, in this review, we focus on results (mainly based on standard PDFs) that impact directly LHC measurements and searches and the impact of this new knowledge is rather weak and we do not enter into details of this huge physics topic which deserves a dedicated review.

12. Soft and hard diffraction at the LHC

The LHC with a center-of-mass energy of 14 TeV will allow us to access a completely new kinematical domain in diffraction. So far, three experiments, namely ATLAS and CMS-TOTEM have shown interest in diffractive measurements. The diffractive event selection at the LHC will be the same as at the Tevatron. However, the rapidity gap selection will no longer be possible at high luminosity since up to 35 interactions per bunch crossing are expected to occur and soft pile-up events will kill the gaps produced by the hard interaction. Proton tagging will thus be the only possibility to detect diffractive events at high luminosity. Let us note that this is not straightforward: we need to make sure that the diffracted protons come from the hard interaction and not from the soft pile up events. The idea we develop in the following is to measure precisely the time of arrival of the diffracted protons in the forward detectors, and thus know if the protons come from the vertex of the hard interaction.

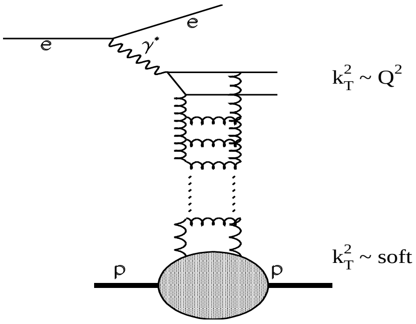

Fig. 53. A diagram describing a gluon ladder in a diffractive process.

Measurements of total cross-section and luminosity are foreseen in the ATLAS-ALFA [97] and TOTEM [98] experiments, and Roman pots are installed at 147 and 220 m in TOTEM and 240 m in ATLAS. These measurements will require a special injection lattice of the LHC at low luminosity since they require the roman pot detectors to be moved very close to the beam.

The measurement of the total cross-section to be performed by the TOTEM Collaboration [98] is shown in Fig. 54. We notice that there is a large uncertainty on predictions of the total cross-section at the LHC energy in particular due to the discrepancy between the two Tevatron measurements. The inelastic $p\bar{p}$ cross-section was measured at a center-of-mass energy of 1.8 TeV at the Tevatron by the E710, E811 and CDF collaborations which lead to the following respective results: 56.6 ± 2.2 mb, 56.5 ± 1.2 mb

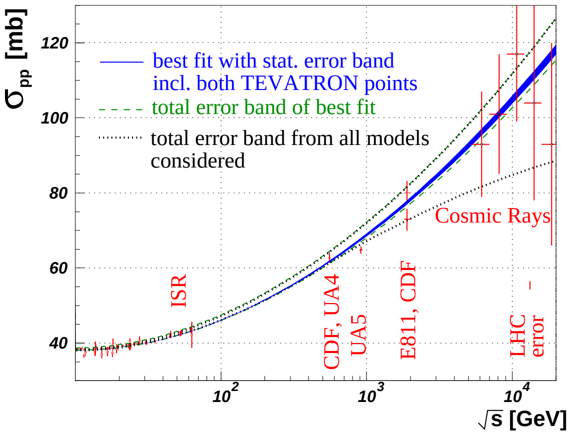

Fig. 54. Measurement of the total cross-section.

and 61.7 ± 1.4 mb [99]. While the E710 and E811 experiments agree (E811 is basically the follow up of E710), the E811 and CDF measurements disagree by 9.2%, and the reason is unclear [99]. The measurement of TOTEM will be of special interest to solve that ambiguity as well.

The ATLAS Collaboration prefers to measure the elastic scattering in the Coulomb region [97], typically at very low t ($|t| \sim 6.5\ 10^{-4}$ GeV^2). When t is close to 0, the t dependence of the elastic cross-section reads:

$$\frac{dN}{dt}(t \to 0) = L\pi \left(\frac{-2\alpha}{|t|} + \frac{\sigma_{\mathrm{tot}}}{4\pi}(i+\rho)e^{-b|t|/2} \right)^2 . \tag{17}$$

From a fit to the data in the Coulomb region, it is possible to determine directly the total cross-section σ_{tot}, the ρ and b parameters as well as the absolute luminosity L. This measurement requires to go down to $t \sim 6.5\ 10^{-4}\,\mathrm{GeV}^2$, or $\theta \sim 3.5\,\mu$rad (to reach the kinematical domain where the strong amplitude equals the electromagnetic one). This measurement requires a special high β^* lattice, the detectors to be installed 1.5 mm from the LHC beam, a spatial resolution of these detectors well below 100 μm and no significant dead edge on the detector (less than 100 μm). The solution to perform this measurement is to install two sets of Roman pot detectors on each side of ATLAS located at about 240 m from the interaction point, which can go close to the beam when the beam is stable.

The second measurement to be performed at the LHC relies on the diffractive dijet cross-section. The dijet mass fraction as a function of different jet p_{T} is visible in Fig. 55 after a simulation of the ATLAS/CMS detectors including inclusive diffraction and the exclusive one which we discuss in the next section. The exclusive contribution manifests itself as an

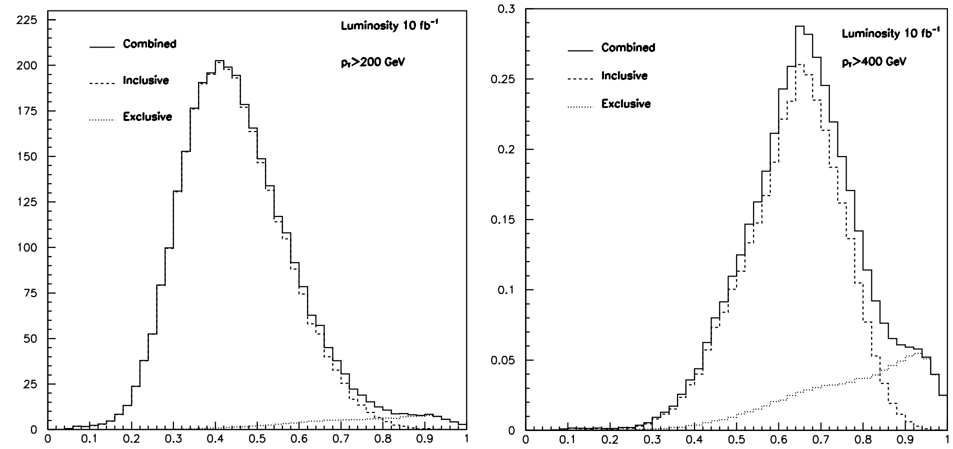

Fig. 55. Dijet mass fraction at the LHC for jets $p_{\mathrm{T}} > 200\,\mathrm{GeV}$ and $p_{\mathrm{T}} > 400\,\mathrm{GeV}$ showing the contribution of both inclusive and exclusive diffraction.

increase in the tail of the distribution which can be seen for 200 GeV jets (left) and 400 GeV jets (right), respectively [103], as we will discuss in the following.

13. Exclusive diffractive events at the Tevatron and the LHC

13.1. Interest of exclusive events

A schematic view of non-diffractive, inclusive double Pomeron exchange, exclusive diffractive events at the Tevatron or the LHC is displayed in Fig. 56. The upper left plot (1) shows the "standard" non-diffractive events where the Higgs boson, the dijet or diphotons are produced directly by a coupling to the proton and shows proton remnants. The right plot (2) displays the standard diffractive double Pomeron exchange where the protons remain intact after interaction and the total available energy is used to produce the heavy object (Higgs boson, dijets, diphotons ...) and the Pomeron remnants. We have so far only discussed this kind of events and their diffractive production using the parton densities measured at HERA. There may be a third class of processes displayed in the lower left figure (3), namely the exclusive diffractive production. In this kind of events, the full energy is used to produce the heavy object (Higgs boson, dijets, diphotons ...) and no energy is lost in Pomeron remnants.

There is an important consequence for the diffractive exclusive events: the mass of the produced object can be computed using Roman pot detectors and tagged protons[4]

---

[4] The formula is more complicated for low mass objects when the proton mass cannot be neglected [100].

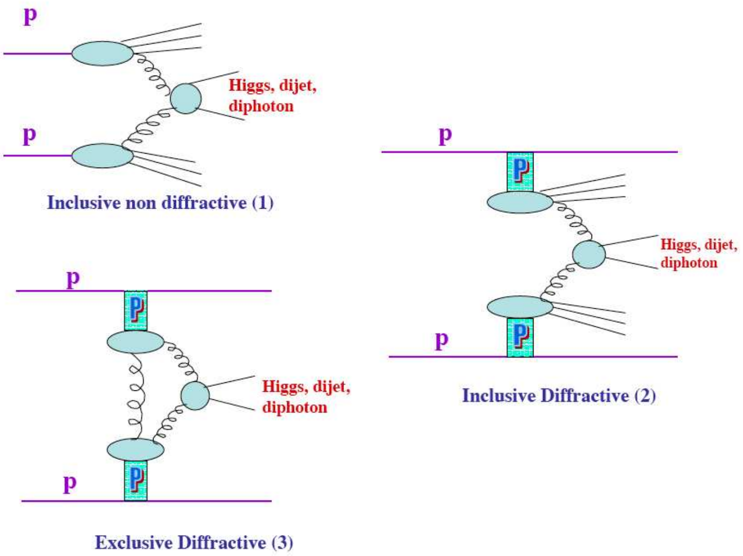

Fig. 56. Scheme of non-diffractive, inclusive double Pomeron exchange, exclusive diffractive events at the Tevatron or the LHC.

$$M = \sqrt{\xi_1 \xi_2 S}\,, \tag{18}$$

where $\sqrt{S}$ is the center-of-mass energy and ξ is the fraction of the proton momentum carried away by the Pomeron (called $x_{I\!P}$ at HERA). The advantage of those processes is obvious: we can benefit from the good forward detector resolution on ξ to get a good mass resolution, and to measure precisely the kinematical properties of the produced object. It is thus important to know if this kind of events exists or not. We now describe in detail the search for exclusive events in the different channels which is performed by the CDF and DØ collaborations at the Tevatron. In the next section, we also discuss the impact of the exclusive events on the LHC physics potential.

13.2. Search for exclusive events in $\chi_{\rm c}$ production

One way to look for exclusive events at the Tevatron is to search for the diffractive exclusive production of light particles like the χ mesons. This leads to high enough cross-sections — contrary to the diffractive exclusive production of heavy mass objects such as Higgs bosons — to check the dynamical mechanisms and the existence of exclusive events. The CDF Collaboration [100] put an upper limit for the χ production cross-section of $\sigma_{\rm exc}(p\bar{p} \to p{+}J/\psi{+}\gamma{+}\bar{p}) \sim 49{\pm}18\,({\rm stat.}){\pm}39\,({\rm syst.})$ pb where the $\chi_{\rm c}$ decays into J/Ψ and γ, the J/Ψ decaying itself into two muons. The experimental signature is very clean, two muons and an isolated photon. The cosmics contamination is difficult to compute and this is why the CDF Collaboration only quotes an upper limit. To know if the production is expected to be a hint of exclusive events, it is important to study the tail of inclusive diffraction which is a direct contamination of the exclusive signal. The tail of inclusive diffraction corresponds to events which show very little energy in the forward direction, or in other words where the Pomeron remnants carry very little energy. In Ref. [100], we found that the contamination of inclusive events into the signal region depends strongly on the assumptions on the gluon distribution in the Pomeron at high β, which is very badly known. Therefore, this channel is unfortunately not conclusive concerning the existence of exclusive events.

13.3. Search for exclusive events in the diphoton channel

The CDF Collaboration also looked for the exclusive production of dilepton and diphoton [101]. Contrary to diphotons, dileptons cannot be produced exclusively via Pomeron exchanges since $gg \to \gamma\gamma$ is possible, but $gg \to l^+l^-$ directly is impossible. Dileptons are produced via QED processes, and the CDF dilepton measurement is $\sigma = 1.6^{+0.5}_{-0.3}\,(\text{stat.})\ \pm 0.3\,(\text{syst.})$ pb which is found to be in good agreement with QED predictions. 3 exclusive diphoton events have been observed by the CDF Collaboration leading to a cross-section of $\sigma = 0.14^{+0.14}_{-0.04}\,(\text{stat.})\ \pm 0.03\,(\text{syst.})$ pb compatible with the expectations for exclusive diphoton production at the Tevatron. Unfortunately, the number of events is very small and the conclusion concerning the existence of exclusive events is uncertain. An update by the CDF Collaboration with higher luminosity is, however, expected very soon. This channel will be, however, very important at the LHC where the expected exclusive cross-section is much higher.

13.4. Search for exclusive events using the dijet mass fraction at the Tevatron

The CDF Collaboration measured the so-called dijet mass fraction in dijet events — the ratio of the mass carried by the two jets produced in the event divided by the total diffractive mass — when the antiproton is tagged in the Roman pot detectors and when there is a rapidity gap on the proton side to ensure that the event corresponds to a double Pomeron exchange [102]. We compare this measurement to the expectation obtained from the Pomeron structure in quarks and gluons as measured at HERA [67, 69]. The factorisation breaking between HERA and the Tevatron is assumed to be constant and to come only through the gap survival probability (0.1 at the Tevatron).

The comparison between the CDF data for a jet p_{T} cut of 10 GeV as an example and the predictions from inclusive diffraction is given in Fig. 57, left, together with the effects of changing the gluon density at high β by changing the value of the ν parameter introduced to vary the gluon density in the Pomeron at high β. Namely, to study the uncertainty on the gluon density at high β, we multiply the gluon distribution by the factor $(1-\beta)^{\nu}$. The ν parameter varies between -1 and 1 (for $\nu=-1$ (resp. $+1$), the gluon density in the Pomeron is enhanced (resp. damped) at high β). QCD fits to the H1 data lead to an uncertainty on the ν parameter of 0.5 [67]. Inclusive diffraction alone is not able to describe the CDF data at high dijet mass fraction, where exclusive events are expected to appear [103]. The conclusion remains unchanged when jets with $p_{\mathrm{T}} > 25$ GeV are considered [103].

Adding exclusive events to the distribution of the dijet mass fraction leads to a good description of data [103] as shown in Fig. 57, right. This does not prove that exclusive events exist but shows that some additional component with respect to inclusive diffraction compatible with exclusive events is needed to explain CDF data. To be sure of the existence of exclusive events, the observation will have to be done in different channels and the different cross-sections to be compared with theoretical expectations.

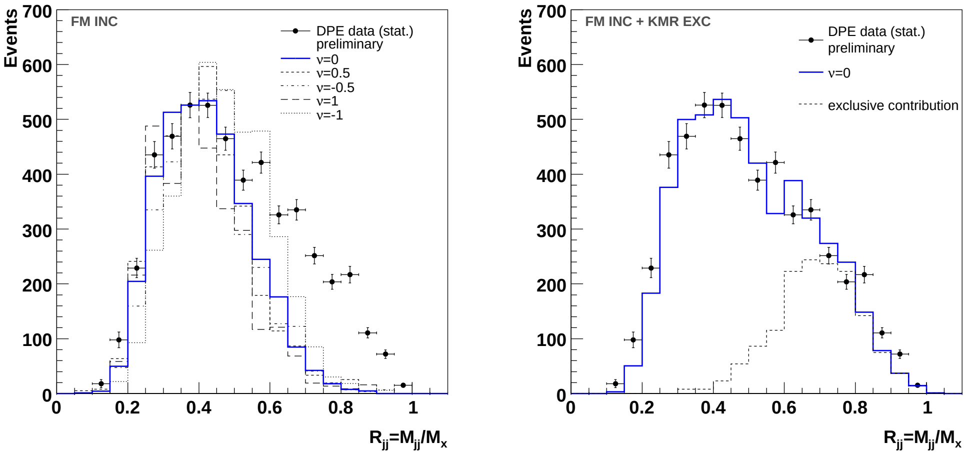

Fig. 57. Left: dijet mass fraction measured by the CDF Collaboration compared to the prediction from inclusive diffraction based on the parton densities in the Pomeron measured at HERA. The gluon density in the Pomeron at high β was modified by varying the parameter ν. Right: dijet mass fraction measured by the CDF Collaboration compared to the prediction adding the contributions from inclusive and exclusive diffraction.

Another interesting observable in the dijet channel is to look at the rate of b jets as a function of the dijet mass fraction. In exclusive events, the b jets are suppressed because of the $J_Z = 0$ selection rule [104], and as expected, the fraction of b jets in the diffractive dijet sample diminishes as a function of the dijet mass fraction (see Fig. 58 from Ref. [102]).

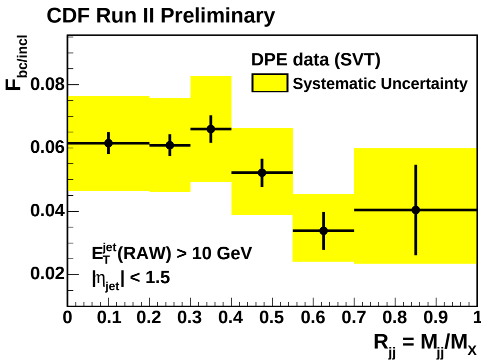

Fig. 58. Ratio of b/c jets to inclusive jets in double Pomeron exchange events as a function of the dijet mass fraction.

Another method to search for exclusive events is to study the correlation between the gap size measured in both p and $\bar{p}$ directions and the value of $\log 1/\xi$ measured using Roman pot detectors [105]. The gap size between the Pomeron remnant and the protons detected in Roman pot detector is of the order of $\log 1/\xi$ for usual diffractive events while exclusive events show a larger rapidity gap since the gap occurs between the jets and the proton detected in Roman pot detectors (in other words, there is no Pomeron remnant).

As we mentioned in a previous section, we also compared the CDF measurements with the expectations from the soft colour interaction (SCI) model. The SCI model is the only model which explains the different normalisation between HERA and Tevatron diffractive data without the need of the survival probability (since it assumes that diffraction is purely due to a soft colour rearrangement in the final state). The CDF dijet data were compared with the predictions from the SCI models [103], and the proportion of needed exclusive events to describe the dijet mass fraction is found to be smaller. However, the SCI model cannot describe properly the jet rapidity distributions which are predicted to be asymmetric around 0 by the SCI model (the CDF requires one tagged proton on one side and a rapidity gap on the other side, and within the SCI model, it is difficult to obtain an intact proton in the final state). For these reasons, the SCI model is disfavoured but it would be probably useful to revisit the ideas and the implementation of such a model in Pythia.

13.5. Search for exclusive events at the LHC

The search for exclusive events at the LHC can be performed in the same channels as the ones used at the Tevatron. Additional possibilities benefiting from the higher luminosity and cross-sections at the LHC appear. One of the cleanest ways to show the existence of exclusive events would be to measure the dilepton and diphoton cross-section ratios as a function of the dilepton/diphoton mass [104,105]. If exclusive events exist, this distribution should show a bump towards high values of the dilepton/diphoton mass since it is possible to produce exclusively diphotons but not dileptons at leading order.

The search for exclusive events at the LHC will also require a precise analysis and measurement of inclusive diffractive cross-sections and in particular the tails at high β since it is a direct background to exclusive event production. It will be also useful to measure directly, as an example, the exclusive jet production cross-section as a function of jet p_{T} and compare the evolution to the models. This will allow to know precisely the background especially to Higgs searches which we discuss in the following.

13.6. Exclusive Higgs production at the LHC

One special interest of diffractive events at the LHC is related to the existence of exclusive events and the search for Higgs bosons at low mass in the diffractive mode. So far, two projects are being discussed at the LHC: the installation of forward detectors at 220 and 420 m in ATLAS and CMS [108] which we describe briefly at the end of this review.

Many studies (including pile up effects and all background sources for the most recent ones) were performed recently [104, 106, 107] to study in detail the signal over background for MSSM Higgs production in particular. The ratio R of the number of diffractive Higgs bosons in MSSM to SM is given in Fig. 59. Typically if R >10, the number of events is high enough to allow a discovery with 30 fb^{-1} per experiment using the diffractive mode. We notice that almost the full plane in ($\tan\beta$, M_A) can be covered even at low luminosity. In Fig. 60, we give the number of background and MSSM Higgs signal events for a Higgs mass of 120 GeV for $\tan\beta \sim$40. The signal significance is larger than 3.5 σ for 60 fb^{-1} (see Fig. 60, left) and larger than 5 σ after three years of data taking at high luminosity at the LHC and using timing detectors with a good timing resolution (see Fig. 60, right).

In some scenario such as NMSSM where the Higgs boson decays in $h \rightarrow aa \rightarrow \tau\tau\tau\tau$ where a is the lighter of the two pseudo-scalar Higgs bosons, the discovery might come only from exclusive diffractive Higgs production [107] ($m_a < 2m_b$ is natural in NMSSM with $m_a > 2m_\tau$ somewhat preferred).

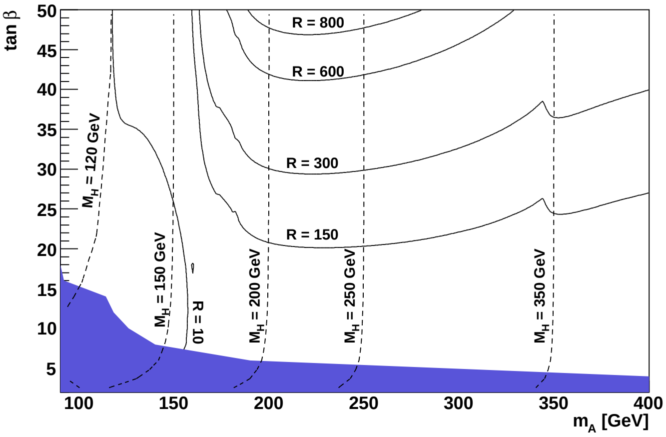

Fig. 59. Ratio R at generator level between the number of diffractive Higgs events in MSSM to SM in the $(\tan\beta,\, M_A)$ plane for heavy CP-even Higgs bosons. The lines of constant Higgs boson mass are also indicated in dashed line.

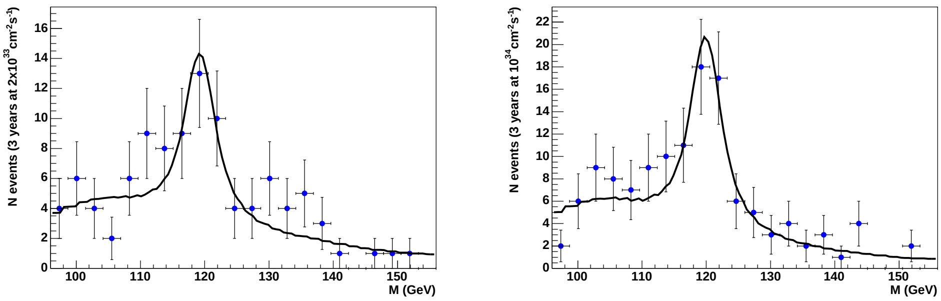

Fig. 60. Higgs signal and background obtained for MSSM Higgs production for neutral light CP-even Higgs bosons. The signal significance is larger than 3.5 σ for 60 fb^{-1} (left plot) and larger than 5 σ after three years of data taking at high luminosity at the LHC and using timing detectors with a resolution of 2 ps (right plot).

13.7. Photon induced processes at the LHC

In this section, we discuss particularly a new possible test of the Standard Model (SM) predictions using photon induced processes at the LHC, and especially WW production [109, 110]. The cross-sections of these processes are computed with high precision using Quantum Electrodynamics (QED) calculations, and an experimental observation leading to differences with expectations would be a signal due to beyond standard model effects. The experimental signature of such processes is the decay products of the W in the main central detectors from the ATLAS and CMS experiments and the presence of two intact scattered protons in the final state.

The experimental signature of diboson events is very clear. Depending on the decay of the W there is zero, one, or two leptons in the final state. When both Ws decay purely hadronically four jets are produced in the final state. This topology can be easily mimicked in the high luminosity environment with pile-up interactions and also suffer from a high QCD background. Therefore, we always require that at least one of the W decays leptonically. In addition, the interpretation of the signal is simple contrary to *e.g.* $e^+e^- \rightarrow WW$ production at LEP where such production could be due to γ or Z exchange and one could not clearly separate the $WW\gamma$ and WWZ couplings. In our case, only the γ exchange is possible since there is no $Z\gamma\gamma$ vertex in the SM.

In summary, we require the following constraints at particle level to select WW events:

- both protons are tagged in the forward detectors in the acceptance $0.0015 < \xi < 0.15$,
- at least one electron or muon is detected with $p_{\mathrm{T}} > 30\,\mathrm{GeV}/c$ and $|\eta| < 2.5$ in the main detector.

The main source of background is the W pair production in Double Pomeron Exchange (DPE), *i.e.* $pp \rightarrow p + WW + Y + p$ through $\mathbb{PP} \rightarrow WW + Y$ where Y denotes the Pomeron remnant system. To remove most of the DPE background, it is possible to cut on the ξ of the protons measured in the proton taggers. Indeed, two-photon events populate the low ξ phase space whereas DPE events show a flat ξ distribution. The $pp \rightarrow pWWp$ cross-section can be measured precisely with a $\mathcal{L}$= 1 fb^{-1} with a statistical significance higher than 20 σ depending on the active ξ range. Using the full ξ acceptance $0.0015 < \xi < 0.15$, one expects about 30 tagged WW events. As ξ_{max}, the upper cut on ξ, decreases, one obtains a cleaner signal, but the number of observed events drops. Already with a low integrated luminosity of $\mathcal{L}$= 200 pb^{-1} it is possible to observe 5.6 W pair two-photon events for a background of DPE lower than 0.4, leading to a signal above 8 σ for WW production via photon induced processes.

New physics with a characteristic scale (*i.e.* the typical mass of new particles) well above what can be probed experimentally at the LHC can manifest itself as a modification of gauge boson couplings due to the exchange of new heavy particles. The conventional way to investigate the sensitivity to the potential new physics is to introduce an effective Lagrangian with additional higher dimensional terms parametrised with anomalous parameters. We consider the modification of the $WW\gamma$ triple gauge boson vertex with additional terms conserving C- and P-parity separately, that are parametrised with two anomalous parameters $\Delta\kappa^\gamma$, λ^γ. The effective Lagrangian reads

$$\begin{aligned}\mathcal{L}/ig_{WW\gamma} &= (W^\dagger_{\mu\nu}W^\mu A^\nu - W_{\mu\nu}W^{\dagger\mu}A^\nu) + (1+\Delta\kappa^\gamma)W^\dagger_\mu W_\nu A^{\mu\nu} \\ &\quad + \frac{\lambda^\gamma}{M_W^2}W^\dagger_{\rho\mu}W^\mu{}_\nu A^{\nu\rho}\,, \end{aligned} \tag{19}$$

where $g_{WW\gamma} = -e$ is the $WW\gamma$ coupling in the SM and the double-indexed terms are $V_{\mu\nu} \equiv \partial_\mu V_\nu - \partial_\nu V_\mu$, for $V^\mu = W^\mu, A^\mu$. In the SM, the anomalous parameters are $\Delta\kappa^\gamma = \lambda^\gamma = 0$. The sensitivity to anomalous coupling can be derived by counting the number of observed events and comparing it with the SM expectation. In order to obtain the best $S/\sqrt{B}$ ratio, the ξ acceptance was further optimised for the λ^γ parameter. The event is accepted if $\xi_i > 0.05$. In the case of $\Delta\kappa^\gamma$, the full acceptance of the forward detectors is used since the difference between the enhanced and SM cross-section is almost flat around relevant values of the coupling $|\Delta\kappa^\gamma|$. For $30\,\mathrm{fb}^{-1}$, the reach on $\Delta\kappa^\gamma$ and λ^γ is respectively 0.043 and 0.034, improving the direct limits from hadronic colliders by factors of 12 and 4, respectively (with respect to the LEP indirect limits, the improvement is only about a factor 2). Using a luminosity of 200 fb^{-1}, present sensitivities coming from the hadronic colliders can be improved by about a factor 30, while the LEP sensitivity can be improved by a factor 5.

It is worth noticing that many observed events are expected in the region $W_{\gamma\gamma} > 1$ TeV where beyond standard model effects, such as SUSY, new strong dynamics at the TeV scale, anomalous coupling, *etc.*, are expected (see Fig. 61). It is expected that the LHC experiments will collect 400 such events predicted by QED with $W >$1 TeV for a luminosity of $200\,\mathrm{fb}^{-1}$ which will allow to probe further the SM expectations. In the same way that we studied the $WW\gamma$ coupling, it is also possible to study the $ZZ\gamma$ one. The SM prediction for the $ZZ\gamma$ coupling is 0, and any observation of this process is directly sensitive to anomalous coupling (the main SM production of exclusive ZZ event will be due to exclusive Higgs boson production decaying into two Z bosons).

Many other studies can be performed using γ induced processes. The WW cross-section measurements are also sensitive to anomalous quartic couplings [111], and recent studies showed that the sensitivity on quartic coupling is 10 000 times better than at LEP with only a luminosity of $10\,\mathrm{fb}^{-1}$. In addition, it is possible to produce new physics beyond the Standard Model. Two photon production of SUSY leptons as an example has been investigated and the cross-section for $\gamma\gamma \to \tilde{l}^+\tilde{l}^-$ can be larger than 1 fb.

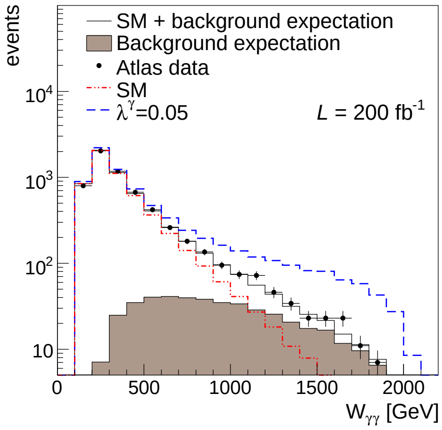

Fig. 61. Distributions of the $\gamma\gamma$ photon invariant mass $W_{\gamma\gamma}$ measured with the forward detectors using $W_{\gamma\gamma} = \sqrt{s\xi_1\xi_2}$. The effect of the λ^{γ} anomalous parameter appears at high $\gamma\gamma$ invariant mass (dashed line). The SM background is indicated in dot-dashed line, the DPE background as a shaded area and their combination in full line. The black points show the ATLAS data smeared according to a Poisson distribution.

13.8. Projects to install forward detectors at the LHC

In this section, we describe briefly the project to install forward detectors at 220 and 420 m in the ATLAS and CMS collaborations [108] allowing to accomplish the physics program we just described, namely a better understanding of diffractive events, the search for exclusive events and the Higgs boson in this mode, and the search for photon anomalous coupling. To obtain a good acceptance in mass (above 50% for masses between 115 and 650 GeV), both detectors at 220 and 420 m are needed, since many events even at low masses show an intact proton in the 220 m detector on one side and in the 420 m one on the other side. Two kinds of detectors namely the 3D Si and the timing detectors, will be hosted in movable beam pipes located at 220 and 420 m.

The idea of movable beam pipes is quite simple and was used already in the ZEUS Collaboration at HERA: when the beam is injected, the movable beam pipe is in its “home” position so that the detectors can be far away from the beam and its halo, and when the beam is stable, the movable beam pipe moves so that the detectors go closer to the beam. A typical movement is of the order of 2 cm. Beam Pipe Monitors will be located in the fixed and movable beam pipe areas to measure how close the detectors are located with respect to the beam. The needed precision is of the order of 10–15 μm. 4 horizontal pockets containing the 3D Silicon and timing detectors will be located within the movable beam pipe structure. The protons are emitted diffractively in the horizontal plane and this is why only horizontal detectors and pockets are needed.

It is assumed that it will be possible to go as close to the beam as 15 σ at 220 and 420 m. To get a full coverage for the diffracted protons, detectors of 2 cm $\times$ 2 cm and of 0.6 cm $\times$ 2 cm are needed at 220 and 420 m respectively. The position of the protons have to be measured with a precision of 10–15 μm in x-direction in a radiation environment and this is why the solution of 3D Silicon pixels has been chosen. The size of the pixels is of 50 μm $\times$ 400 μm and a supermodule shows an active area of 7.2 mm $\times$ 8 mm. There will be 10 layers of such supermodules staggered in x and y directions perpendicular to the beam. This will allow to obtain the needed resolution. To achieve the full coverage, 3 and 6 supermodules per layer are needed at 420 and 220 m respectively. The alignment of these detectors will be achieved using exclusive dimuon events — this can be performed at a store-by-store basis at 420 m and only on a week basis at 220 m since the 220 m detectors are sensitive to higher dimuon mass events — and also possibly using elastics events which would imply the installation of vertical detectors as well.

The 3D Si detector at 220 m can also provide a L1 trigger allowing to cut on the proton momentum loss (the 420 m detector is too far away to make it to the L1 trigger). Two kinds of trigger are considered. The first one triggers on events when both protons are detected at 220 m. The second (more difficult) triggers on events when only one proton is present at 220 m. In that case, the idea is to cut on the acceptance at 220 m corresponding to the possibility of a tag at 420 m. A typical jet trigger will be: two jets with a transverse momentum above 40 GeV, one proton at 220 m with a momentum loss smaller than 0.05 compatible with the presence of a proton at 420 m on the other side, and the exclusiveness of the process (most of the energy is carried by the two hard jets). With these cuts, the L1 rate is expected to be smaller than 1 kHz for a luminosity smaller than 2×10^{33} cm^{-2}s^{-1}. The expected output at L2 is assumed to be only a few Hz only since the timing and the 420 m detector informations will be available at this stage.

The other kind of detector which is crucial for this project is the timing detectors. At the LHC, up to 35 interactions occur at the same bunch crossing and we need to know if the observed protons in the final state originate from the main interaction producing for instance the Higgs boson or the WW event, or from a secondary one which is not related to the hard interaction. To achieve this goal, it is needed to know if the protons are coming from the main vertex of the event, and for this sake, to measure precisely the time of flight of the protons with a precision of the order of 10–15 ps or better. Two kinds of detectors have been proposed. The GASTOF measures the Cerenkov light emitted by the protons and collected in a multichannel photomultiplier. This detector has a very good intrinsic resolution measured in beam tests of about 10–15 ps, but presents the inconvenience of showing no lateral space resolution which is needed in the case of multiple protons are produced in one bunch crossing. The other device, QUARTIC, uses quartz radiator bars to emit the photons and leads to a resolution per detector of 30–40 ps. Several detectors are thus needed to achieve the wanted resolution. The advantage of such detectors is that it can have a couple of mm space resolution and the inconvenient is the smaller number of photoelectrons produced. The idea would be thus to combine the advantages of the GASTOF and QUARTIC detectors which is under study now in a world-wide collaboration regrouping the institutes of Louvain, Chicago, Fermilab, Argonne National Lab, Brookhaven National Lab, Stony Brook, Alberta, Texas Arlington, Saclay and Orsay. This kind of detectors is also specially interesting for medical applications since it would allow to improve the present resolution of the PET imaging detectors by one order of magnitude.

14. Conclusion

The aim of this review is to describe the present vision we have of the proton structure at high energy from the HERA and Tevatron data and to discuss the potential improvements brought by the LHC.

Parton momentum density distributions are important ingredients in the calculation of high energy hadron–hadron and lepton–hadron scattering cross-sections. In these calculations the cross-sections are written as a convolution of the parton densities and the elementary cross-sections for parton–parton or lepton–parton scattering. Whereas the latter can be perturbatively calculated in the framework of the Standard Model, the parton densities are non-perturbative quantities and are obtained from DGLAP based fits to measured cross-sections at various experiments.

After showing the present status of PDF determination at the Tevatron and HERA, we discussed the possible LHC measurements at LHC that will increase our knowledge of the PDFs, as well as the dependence of the LHC measurements and discovery potential on the present PDF uncertainties. We stressed that the current PDF uncertainty on some LHC observables is underestimated as a consequence of hidden assumptions in current PDF sets. The usual sea quark symmetry assumptions, relating the $\bar{u}$, $\bar{d}$ and $\bar{s}$ densities, are prominent examples that affect the study of electroweak boson production. We review a number of processes that can be measured at the LHC and allow to test the validity of these assumptions. In some cases, cross-section ratios can be defined that are less sensitive to PDF uncertainties while preserving the sensitivity to new physics effects.

In a second part of the paper, we study another striking kind of events as they appear at HERA or Tevatron, namely diffractive events, where in most cases, the proton is found intact after the interaction. Diffractive events provide another way to examine the structure of matter under specific conditions, at large gluon densities at HERA for example. We first describe the ongoing measurements of inclusive and exclusive diffraction at HERA, which is the starting point to study diffraction at Tevatron and then LHC. Some evidence of a new kind of diffractive events, namely exclusive events, where all available energy is used to diffractively produce high mass objects, was shown at Tevatron. These events are particularly interesting at LHC where diffractive Higgs events might occur through this mechanism. Tagging the intact final state protons will also allow to measure photon induced processes, and to study the γW coupling in W pair production. The link of the diffractive data with saturation effects which we also discussed is an interesting and promising issue for the future and could lead to a global unified view of the proton.

To summarize, the vision of the proton we have at present was definitely improved with the recent data from HERA and Tevatron but still suffers from large uncertainties at low or high x, with significant impact on LHC physics. No doubt that the understanding of the proton structure will be further improved at LHC, and new observables less sensitive to PDF uncertainties can be used to disentangle in a better way the PDF effects from the ones due to new physics. Diffractive events still deserve to be explained via a unified understanding of the proton structure and it might be that saturation physics will help us achieving this goal. Finally, the rich PDF and diffractive program at LHC will definitely lead to new unforeseen insights of the proton.

We thank R. Peschanski for a careful reading of the manuscript.

REFERENCES

[1] [ATLAS Collaboration], CERN/LHCC 99-14, CERN/LHCC 99-15.

[2] [ATLAS Collaboration], `arXiv:0901.0512`.

[3] [CMS Collaboration], CERN/LHCC 2006-001, CERN/LHCC 2006-002.

[4] G. Altarelli, G. Parisi, *Nucl. Phys.* **B126**, 298 (1977); V.N. Gribov, L.N. Lipatov, *Sov. J. Nucl. Phys.* **15**, 438 (1972); 675 (1972). Yu.L. Dokshitzer, *Sov. Phys. JETP* **46**, 641 (1977).

[5] V.S. Fadin, L.N. Lipatov, *Phys. Lett.* **B429**, 127 (1998); M. Ciafaloni, *Phys. Lett.* **B429**, 363 (1998); M. Ciafaloni, G. Camici, *Phys. Lett.* **B430**, 349 (1998); L.N. Lipatov, *Sov. J. Nucl. Phys.* **23**, 338 (1976); E.A. Kuraev, L.N. Lipatov, V.S. Fadin, *Sov. Phys. JETP* **45**, 199 (1977); I.I. Balitsky, L.N. Lipatov, *Sov. J. Nucl. Phys.* **28**, 822 (1978).

[6] A.M. Cooper-Sarkar, R.C.E. Devenish, A. De Roeck, *Int. J. Mod. Phys.* **A13**, 3385 (1998); M. Klein, R. Yoshida, *Prog. Part. Nucl. Phys.* **61**, 343 (2008).

[7] P. Nadolsky *et al., Phys. Rev.* **D78**, 013004 (2008).

[8] A. Martin *et al.*, `arXiv:0901.0002`.

[9] R.D. Ball *et al., Nucl. Phys.* **B809**, 1 (2009); L. Del Debbio *et al. J. High Energy Phys.* **0703**, 039 (2007).

[10] [H1 and ZEUS Collaborations], H1prelim-08-045, ZEUS-prel-08-003 (2008); P. Nadolsky *et al., Phys. Rev.* **D78**, 013004 (2008).

[11] V.M. Abazov *et al., Phys. Rev. Lett.* **101**, 062001 (2008); A. Abulencia *et al., Phys. Rev.* **D75**, 092006 (2007); *Phys. Rev.* **D74**, 071103 (2006).

[12] W.K. Tung *et al., J. High Energy Phys.* **0702**, 053 (2007); J. Pumplin *et al., J. High Energy Phys.* **0207**, 12 (2002); D. Stump *et al., J. High Energy Phys.* **0310**, 046 (2003); A.D. Martin *et al., Phys. Lett.* **B604**, 61 (2004).

[13] See `http://www-cdf.fnal.gov/physics/new/qcd/QCD.html`

[14] V.M. Abazov *et al., Phys. Rev. Lett.* **94**, 221801 (2005).

[15] T. Sjöstrand *et al., Comput. Phys. Commun.* **135**, 238 (2001).

[16] G. Marchesini *et al., Comput. Phys. Commun.* **67**, 465 (1992).

[17] V.M. Abazov *et al., Phys. Lett.* **B666**, 435 (2008).

[18] D. Acosta *et al., Phys. Rev.* **D71**, 112002 (2005).

[19] A. Abulencia *et al.*, preprint `arXiv:0806.1699 [hep-ex]`.

[20] V.M. Abazov *et al., Phys. Lett.* **B666**, 23 (2008); T. Aaltonen *et al., Phys. Rev. Lett.* **100**, 091803 (2008).

[21] A. Abulencia *et al., Phys. Rev.* **D74**, 032008 (2008);
see `http://www-cdf.fnal.gov/physics/new/qcd/QCD.html`

[22] C. Anastasiou *et al., Nucl. Phys.* **B724**, 197 (2005).

[23] A. Djouadi *et al., Comput. Phys. Commun.* **108**, 56 (1998).

[24] A. Djouadi, S. Ferrag, *Phys. Lett.* **B586**, 345 (2004).

[25] See for example E. Fahri, L. Susskind, *Phys. Rep.* **74**, 277 (1981).

[26] See for example L. Randall, R. Sundrum, *Phys. Rev. Lett.* **83**, 3370 (1999).

[27] S. Ferrag, `hep-ph/0407303`.

[28] [ATLAS Collaboration] H. Stenzel, ATL-PHYS-2001-003.

[29] [ATLAS Collaboration] D. Clements, *Deep-Inelastic Scattering*, vol. 2* 1015–1018 (DIS2007).

[30] [ATLAS Collaboration], *JINST* **3**, S08003 (2008).

[31] I. Hollins, PhD dissertation, University of Birmingham, 2006.

[32] E. Berger, L. Gordon, M. Klasen, *Phys. Rev.* **D58**, 074012 (1998).

[33] See `http://www-d0.fnal.gov/Run2Physics/ICHEP08/S08DØResults.html`

[34] K. Melnikov, F. Petriello, *Phys. Rev.* **D74**, 114017 (2006).

[35] N. Adam, V. Halyo, S. Yost, W. Zhu, *J. High Energy Phys.* **0809**, 133 (2008).

[36] N. Adam, V. Halyo, S. Yost, W. Zhu, *J. High Energy Phys.* **0805,** 062 (2008).

[37] W.K. Tung *et al., J. High Energy Phys.* **0702**, 053 (2007).

[38] A.D. Martin *et al., Eur. Phys. J.* **C28**, 455 (2003); *Eur. Phys. J.* **C35**, 325 (2004).

[39] S. Alekhin, *Phys. Rev.* **D68**, 014002 (2003).

[40] S. Berge *et al., Phys. Rev.* **D72**, 033015 (2005).

[41] M.W. Krasny, F. Fayette, W. Placzek, A. Siodmok, *Eur. Phys. J.* **C51**, 607 (2007).

[42] [ATLAS Collaboration] N. Besson *et al., Eur. Phys. J.* **C57**, 627 (2008) `[arXiv:0805.2093[hep-ex]]`.

[43] [LEP Collaborations: ALEPH, DELPHI, L3, OPAL], `hep-ph/0612034`.

[44] B. Fuks *et al., Nucl. Phys.* **B797**, 322 (2008).

[45] T.G. Rizzo, *J. High Energy Phys.* **0705**, 037 (2007).

[46] [CDF Collaboration] T. Aaltonen, *et al.*, `arXiv:0812.4458 [hep-ex]`; *Phys. Rev. Lett.* **100**, 102001 (2008); *Phys. Rev.* **D77**, 011108 (2008); [DØ Collaboration] V.M. Abazov *et al.*, *Phys. Rev. Lett.* **94**, 161801 (2005); *Phys. Lett.* **B666**, 23 (2008).

[47] S.J. Brodsky, P. Hoyer, C. Peterson, N. Sakai, *Phys. Lett.* **B93**, 451 (1980).

[48] A. Tricoli, A. Cooper-Sarkar, C. Gwenlan, `arXiv:hep-ex/0509002v1`.

[49] M. Dittmar, F. Pauss, D. Zuercher, `arXiv:hep-ex/9901004`.

[50] J.G. Contreras, R. Peschanski, C. Royon, *Phys. Rev.* **D62**, 034006 (2000); C. Marquet, R. Peschanski, C. Royon, *Phys. Lett.* **B599**, 236 (2004); C. Marquet, C. Royon, *Nucl. Phys.* **B739**, 131 (2006).

[51] O. Kepka, C. Marquet, R. Peschanski, C. Royon, *Phys. Lett.* **B655**, 236 (2007); *Eur. Phys. J.* **C55**, 259 (2008).

[52] G.P. Salam, *J. High Energy Phys.* **9807**, 019 (1998); M. Ciafaloni, D. Colferai, G.P. Salam, *Phys. Rev.* **D60**, 114036 (1999); *J. High Energy Phys.* **9910**, 017 (1999).

[53] A.H. Mueller, H. Navelet, *Nucl. Phys.* **B282**, 727 (1987); C. Marquet, C. Royon, preprint `arXiv:0704.3409` and references therein; A. Sabio Vera, F. Schwennsen, *Nucl. Phys.* **B776**, 170 (2007); *Phys. Rev.* **D77**, 014001 (2008).

[54] [DØ Collaboration] S. Abachi *et al., Phys. Rev. Lett.* **72**, 2332 (1994); *Phys. Rev. Lett.* **76**, 734 (1996); [CDF Collaboration] F. Abe *at al., Phys. Rev. Lett.* **74**, 855 (1995); *Phys. Rev. Lett.* **80**, 1156 (1998); *Phys. Rev. Lett.* **81**, 5278 (1998); J.D. Bjorken, *Phys. Rev.* **D47**, 101 (1992); A.H. Mueller, W.-K. Tang, *Phys. Lett.* **B284**, 123 (1992); B. Cox, J. Forshaw, L. Lonnblad, *J. High Energy Phys.* **9910**, 23 (1999); F. Chevallier, O. Kepka, C. Marquet, C. Royon, *Phys. Rev.* **D79**, 094019 (2009).

[55] C. Marquet, L. Schoeffel, *Phys. Lett.* **B639**, 471 (2006); G. Beuf, R. Peschanski, C. Royon, D. Salek, *Phys. Rev.* **D78**, 074004 (2008); G. Beuf, `arXiv:0803.2167`; G. Beuf, C. Royon, D. Salek, `arXiv:0810.5082`.

[56] F. Gelis, R. Peschanski, G. Soyez, L. Schoeffel, *Phys. Lett.* **B647**, 376 (2007).

[57] K.J. Golec-Biernat, M. Wusthoff, *Phys. Rev.* **D59**, 014017 (1999); K.J. Golec-Biernat, M. Wusthoff, *Phys. Rev.* **D60**, 114023 (1999); K.J. Golec-Biernat, S. Sapeta, *Phys. Rev.* **D74**, 054032 (2006).

[58] A.M. Staśto, K. Golec-Biernat, J. Kwiecinski, *Phys. Rev. Lett.* **86**, 596 (2001); K. Golec-Biernat, M. Wusthoff, *Phys. Rev.* **D59**, 014017 (1999).

[59] I. Balitsky, *Nucl. Phys.* **B463**, 99 (1996); Y.V. Kovchegov, *Phys. Rev.* **D61**, 074018 (2000).

[60] [H1 Collaboration] A. Aktas *et al., Eur. Phys. J.* **C48**, 715 (2006).

[61] [H1 Collaboration] A. Aktas *et al., Eur. Phys. J.* **C48**, 749 (2006).

[62] E. Sauvan, published in *Tsukuba 2006, Deep Inelastic Scattering* p. 211–214, `arXiv:hep-ex/0607038`.

[63] [ZEUS Collaboration] S. Chekanov, *Nucl. Phys.* **B800**, 1 (2008).

[64] [ZEUS Collaboration] S. Chekanov *et al., Nucl. Phys.* **B713**, 3 (2005).

[65] [ZEUS Collaboration] S. Chekanov *et al., Eur. Phys. J.* **C38**, 43 (2004).

[66] J. Collins, *Phys. Rev.* **D57**, 3051 (1998).

[67] C. Royon, L. Schoeffel, J. Bartels, H. Jung, R. Peschanski, *Phys. Rev.* **D63**, 074004 (2001); C. Royon, L. Schoeffel, S. Sapeta, R.B. Peschanski, E. Sauvan, *Nucl. Phys.* **B781**, 1 (2007); C. Royon, L. Schoeffel, R.B. Peschanski, E. Sauvan, *Nucl. Phys.* **B746**, 15 (2006).

[68] G. Ingelman, P.E. Schlein, *Phys. Lett.* **B152**, 256 (1985).

[69] L. Schoeffel, `arXiv:0707.3706[hep-ph]`.

[70] [H1 Collaboration], *Z. Phys.* **C76**, 613 (1997).

[71] A.H. Mueller, *Nucl. Phys.* **B335**, 115 (1990); N.N. Nikolaev, B.G. Zakharov, *Zeit. Phys.* **C49**, 607 (1991); A.H. Mueller, B.Patel, *Nucl. Phys.* **B425**, 471 (1994); A.H. Mueller, *Nucl. Phys.* **B437**, 107 (1995); A.H. Mueller, *Nucl. Phys.* **B415**, 373 (1994); A. Bialas, R. Peschanski, *Phys. Lett.* **B378**, 302 (1996); *Phys. Lett.* **B387**, 405 (1996); H. Navelet, R. Peschanski, Ch. Royon, S. Wallon, *Phys. Lett.* **B385**, 357 (1996); H. Navelet, R. Peschanski, C. Royon, *Phys. Lett.* **B366**, 329 (1996); A. Bialas, R. Peschanski, C. Royon, *Phys. Rev.* **D57**, 6899 (1998); S. Munier, R. Peschanski, C. Royon, *Nucl. Phys.* **B534**, 297 (1998);

[72] J. Bartels, J. Ellis, H. Kowalski, M. Wuesthoff, *Eur. Phys. J.* **C7**, 443 (1999); J. Bartels, C. Royon, *Mod. Phys. Lett.* **A14**, 1583 (1999).

[73] A. Edin, G. Ingelman, J. Rathsman, *Phys. Lett.* **B366**, 371 (1996).

[74] C. Royon, *Acta Phys. Pol. B* **37**, 3571 (2006); *Acta Phys. Pol. B* **39**, 2339 (2008).

[75] M. Gallinaro, talk given at the DIS 2006 workshop, 20–24 April 2006, Tsukuba, Japan, see `http://www-conf.kek.jp/dis06/`; Dino Goulianos, talk given at the "Low x" 2006 workshop, June 28–July 1, 2006, Lisbon, Portugal, see `http://www-d0.fnal.gov/ royon/lowx_lisbon`; CDF Collaboration, *Phys. Rev. Lett.* **88**, 151802 (2002).

[76] CDF Collaboration, *Phys. Rev. Lett.* **84**, 5043 (2000); *Phys. Rev. Lett.* **87**, 141802 (2001).

[77] [ZEUS Collaboration] J. Breitweg *et al., Eur. Phys. J.* **C2**, 2 (1998); [ZEUS Collaboration] M. Derrick *et al., Eur. Phys. J.* **C6**, 603 (1999); [H1 Collaboration] C. Adloff *et al., Eur. Phys. J.* **C13**, 371 (2000); [H1 Collaboration] C. Adloff *et al., Phys. Lett.* **B539**, 25 (2002) [`arXiv:hep-ex/0203022`].

[78] [H1 Collaboration] C. Adloff *et al., Phys. Lett.* **B483**, 360 (2000); [ZEUS Collaboration] S. Chekanov *et al., Nucl. Phys.* **B718**, 3 (2005).

[79] [ZEUS Collaboration] S. Chekanov *et al., Nucl. Phys.* **B695**, 3 (2004); [H1 Collaboration] A. Aktas *et al., Eur. Phys. J.* **C46**, 585 (2006).

[80] [H1 Collaboration] F.D. Aaron *et al., Phys. Lett.* **B659**, 796 (2008).

[81] [H1 Collaboration] A. Aktas *et al., Eur. Phys. J.* **C44**, 1 (2005) [`arXiv:hep-ex/0505061`].

[82] [H1 Collaboration] C. Adloff *et al., Phys. Lett.* **B517**, 47 (2001) [`arXiv:hep-ex/0107005`].

[83] [ZEUS Collaboration] S. Chekanov *et al., Phys. Lett.* **B573**, 46 (2003) [`arXiv:hep-ex/0305028`].

[84] M. Diehl, T. Gousset, B. Pire, J. P. Ralston, *Phys. Lett.* **B411**, 193 (1997) [`hep-ph/9706344`].

[85] M. Burkardt, *Int. J. Mod. Phys.* **A18**, 173 (2003) [`hep-ph/0207047`].

[86] M. Diehl, *Eur. Phys. J.* **C25**, 223 (2002); Erratum **C31**, 277 (2003) [`hep-ph/0205208`].

[87] L. Frankfurt, M. Strikman, C. Weiss, *Annu. Rev. Nucl. Part. Sci.* **55**, 403 (2005) [`hep-ph/0507286`].

[88] H. Kowalski, L. Motyka, G. Watt, *Phys. Rev.* **D74**, 074016 (2006).

[89] K. Kumericki, D. Mueller, K. Passek-Kumericki, *Eur. Phys. J.* **C58**, 193 (2008) [`arXiv:0805.0152[hep-ph]`]; `arXiv:0807.0159 [hep-ph]`.

[90] L. Schoeffel, *Phys. Lett.* **B658**, 33 (2007) [`arXiv:0706.3488 [hep-ph]`].

[91] K. Goeke *et al., Prog. Part. Nucl. Phys.* **47**, 401 (2001); M. Diehl, *Phys. Rep.* **388**, 41 (2003); A.V. Belitsky, A.V. Radyushkin, *Phys. Rep.* **418**, 1 (2005).

[92] [CLAS Collaboration] F.X. Girod *et al., Phys. Rev. Lett.* **100**, 162002 (2008); [Jefferson Lab Hall A Collaboration and Hall A DVCS Collaboration] C. Munoz Camacho *et al., Phys. Rev. Lett.* **97**, 262002 (2006); [CLAS Collaboration] S. Chen *et al., Phys. Rev. Lett.* **97**, 072002 (2006); [CLAS Collaboration] S. Stepanyan *et al., Phys. Rev. Lett.* **87**, 182002 (2001).

[93] [HERMES Collaboration] A. Airapetian *et al., J. High Energy Phys.* **0806**, 066 (2008); [HERMES Collaboration] A. Airapetian *et al., Phys. Rev.* **D75**, 011103 (2007); [HERMES Collaboration] A. Airapetian *et al., Phys. Rev. Lett.* **87**, 182001 (2001).

[94] L. Schoeffel, `arXiv:0705.2925 [hep-ph]`.

[95] N. d'Hose, E. Burtin, P.A.M. Guichon, J. Marroncle, M. Moinester, J. Pochodzalla, A. Sandacz, `arXiv:hep-ex/0212047`.

[96] B. Pire, L. Szymanowski, J. Wagner, *Phys. Rev.* **D79**, 014010 (2009); `arXiv:0811.0321`.

[97] [ATLAS Collaboration], see `http://atlas-project-lumi-fphys.web.cern.ch/atlas-project-lumi-fphys/`; C. Royon, Proccedings of Science DIFF2006 (2006) 021.

[98] [TOTEM Collaboration], see `http://totem.web.cern.ch/Totem/`, TOTEM Technical Design Report.

[99] [E710 Collaboration], *Phys. Rev. Lett.* **63**, 2784 (1989); [E811 Collaboration], *Phys. Lett.* **B445**, 419 (1999); [CDF Collaboration], *Phys. Rev.* **D50**, 5550 (1994).

[100] M. Rangel, C. Royon, G. Alves, J. Barreto, R. Peschanski, *Nucl. Phys.* **B774**, 53 (2007); [CDF Collaboration], analysis and results described in: `http://www-cdf.fnal.gov/physics/new/qcd/abstracts/dpe_ex_07.html`

[101] [CDF Collaboration], *Phys. Rev. Lett.* **99**, 242002 (2007).

[102] [CDF Collaboration], `hep-ex/0712.0604`.

[103] O. Kepka, C. Royon, *Phys. Rev.* **D76**, 034012 (2007).

[104] C. Royon, *Mod. Phys. Lett.* **A18**, 2169 (2003) and references therein; M. Boonekamp, R. Peschanski, C. Royon, *Phys. Rev. Lett.* **87**, 251806 (2001); *Nucl. Phys.* **B669**, 277 (2003); M. Boonekamp, A. De Roeck, R. Peschanski, C. Royon, *Phys. Lett.* **B550**, 93 (2002); V.A. Khoze, A.D. Martin, M.G. Ryskin, *Eur. Phys. J.* **C19**, 477 (2001); *Eur. Phys. J.* **C23**, 311 (2002); *Eur. Phys. J.* **C24**, 581 (2002); `arXiv:0802.0177`; *Phys. Lett.* **B650**, 41 (2007); A.B. Kaidalov, V.A. Khoze, A.D. Martin, M.G. Ryskin, *Eur. Phys. J.* **C33**, 261 (2004); *Eur. Phys. J.* **C31**, 387 (2003); R. Peschanski, M. Rangel, C. Royon, `arXiv:0808.1691`.

[105] C. Royon, Fermilab-CONF-06-018E, `hep-ph/0601226`; TeV4LHC QCD Working Group, FERMILAB-CONF-06-359, `hep-ph/0610012`.

[106] M. Boonekamp, J. Cammin, S. Lavignac, R. Peschanski, C. Royon, *Phys. Rev.* **D73**, 115011 (2006) and references therein.

[107] B. Cox, F. Loebinger, A. Pilkington, *J. High Energy Phys.* **0710**, 090 (2007); S. Heinemeyer *et al., Eur. Phys. J.* **C53**, 231 (2008); J.R. Forshaw, J.F. Gunion, L. Hodgkinson, A. Papaefstathiou, A.D. Pilkington, *J. High Energy Phys.* **0804**, 090 (2008).

[108] [FP420 Collaboration], see `http://www.fp420.com`; `arXiv:0806.0302`; M. Albrow *et al.*, CERN-LHCC-2006-039; ATLAS and CMS TDR to be submitted; see: `http://project-rp220. web.cern.ch/project-rp220`; C. Royon, `arXiv:0706.1796`, proceedings of 15th International Workshop on Deep-Inelastic Scattering and Related Subjects (DIS2007), Munich, Germany, 16–20 April, 2007.

[109] M. Boonekamp, J. Cammin, R. Peschanski, C. Royon, *Phys. Lett.* **B654**, 104 (2007).

[110] O. Kepka, C. Royon, *Phys. Rev.* **D78**, 073005 (2008).

[111] T. Pierzchala, K. Piotrzkowski, `arXiv:0807.1121 [hep-ph]`; N. Schul, K. Piotrzkowski, `arXiv:0806.1097 [hep-ph]`.

[112] H. Weigert, *Prog. Part. Nucl. Phys.* **55**, 461 (2005).

[113] I. Balitsky, *Nucl. Phys.* **B463**, 99 (1996).

[114] D. Kharzeev, E. Levin, *Phys. Lett.* **B523**, 79 (2001).